FACULTY OF ENGINEERING AND ARCHITECTURE

Impact of Onyx Injection Velocity in Endovascular Embolization: a Computational Multi-Phase Flow Study of a Patient-Specific Arteriovenous Malformation

Kaat Wille
Student number: 02010479

Supervisors: Prof. dr. ir. Charlotte Debbaut, Prof. dr. Peter Vanlangenhove
Counsellors: Jessie Duquesne, Dr. ir. Danilo Babin, Mohammadjavad Sedghizadeh, Prof. ir. Vincent Keereman

Master's dissertation submitted in order to obtain the academic degree of
Master of Science in Biomedical Engineering

Academic year 2024-2025

GHENT UNIVERSITY

VUB VRIJE UNIVERSITEIT BRUSSEL

FACULTY OF ENGINEERING AND ARCHITECTURE

Impact of Onyx Injection Velocity in Endovascular Embolization: a Computational Multi-Phase Flow Study of a Patient-Specific Arteriovenous Malformation

Kaat Wille
Student number: 02010479

Supervisors: Prof. dr. ir. Charlotte Debbaut, Prof. dr. Peter Vanlangenhove
Counsellors: Jessie Duquesne, Dr. ir. Danilo Babin, Mohammadjavad Sedghizadeh, Prof. ir. Vincent Keereman

Master's dissertation submitted in order to obtain the academic degree of
Master of Science in Biomedical Engineering

Academic year 2024-2025

GHENT UNIVERSITY

VUB VRIJE UNIVERSITEIT BRUSSEL

Preface

I am grateful to have had the opportunity to conduct my thesis on computational fluid dynamics modeling in arteriovenous malformations, a topic that aligns with my profound interest in research on the integration of computational simulations to advance personalized medicine. I would like to express my gratitude to my promotors, prof. dr. ir. Charlotte Debbaut and prof. dr. Peter Vanlangenhove, and my supervisors, ir. Jessie Duquesne, dr. ir. Danilo Babin, ir. Mohammadjavad Sedghizadeh and prof. ir. Vincent Keereman, for making this thesis possible.

In particular, I would like to thank prof. dr. ir. Charlotte Debbaut for her support through regular meetings and insightful feedback throughout the year. Her guidance and input, shaped by her expertise in the field, were greatly appreciated.

Moreover, I am especially grateful to ir. Jessie Duquesne for her exceptional guidance throughout this year. Her readiness to assist, whether through swift email replies, frequent update meetings, or insightful feedback, was invaluable. I am thankful for the time and effort she dedicated to carefully reviewing my work, offering constructive suggestions, and providing detailed proofreading. I greatly appreciated her guidance, which was instrumental in shaping this thesis.

Kaat Wille
June 2025

Permission of Use on Loan

"The author gives permission to make this master dissertation available for consultation and to copy parts of this master dissertation for personal use. In all cases of other use, the copyright terms have to be respected, in particular with regard to the obligation to state explicitly the source when quoting results from this master dissertation."

Kaat Wille
June 2025

Remark on the master's dissertation and presentation

"This master's dissertation is part of an exam. Any comments formulated by the assessment committee during the oral presentation of the master's dissertation are not included in this text."

Kaat Wille
June 2025

Acknowledgement of Generative AI Use

Generative AI tools (such as ChatGPT) were used to assist in rephrasing certain sections of text for improved clarity and conciseness, and to help debug minor technical issues in Python code. All scientific ideas, interpretations, and methods were created or implemented independently without the use of such generative AI programs.

Kaat Wille
June 2025

Abstract

Cerebral arteriovenous malformations (AVMs) are a type of vascular malformation in the brain vasculature, characterized by an abnormal direct connection between the arteries and veins. These malformations commonly form a tangled network of blood vessels that bypass the capillary beds. This creates a high-flow, low-resistance shunt that alters normal cerebral hemodynamics and increases the risk of hemorrhage, seizures, and other neurological deficits. A commonly used treatment strategy is endovascular embolization, a minimally invasive procedure in which a liquid embolic agent is injected through a microcatheter to occlude the AVM and establish a safer hemodynamic state. A widely used embolic agent is Onyx, a suspension of ethylene-vinyl alcohol copolymer dissolved in dimethyl sulfoxide. The procedural outcomes are operator-dependent and might be influenced by the clinician's experience in controlling factors such as catheter placement and injection velocity. Therefore, quantitative tools like computational fluid dynamics (CFD) are valuable for simulating embolic agent behavior and evaluating the impact of different parameters. One key parameter expected to influence outcomes is the Onyx injection rate, which is currently not routinely monitored during procedures, despite Food and Drug Administration (FDA) guidelines recommending a rate of 0.16 ml/min and setting a strict upper limit of 0.30 ml/min (due to angionecrosis and vasospasm observed in animal studies). This thesis examines the influence of the injection rate through CFD modeling, using a multi-phase Volume-of-Fluid approach to simulate both blood and Onyx. Simulations were performed on a patient-specific AVM geometry segmented based on 3D rotational angiography images, with boundary conditions derived from literature and patient-specific digital subtraction angiography data. Preliminary results indicate that injection rate significantly affects Onyx distribution and local hemodynamics. Higher injection rates appear to accelerate Onyx progression, modify its distribution within the AVM, and lead to slightly increased local pressure differences, with maximal values of 0.44 Pa in the absence of Onyx injection and 4.47 Pa, 5.95 Pa, and 8.85 Pa for injection rates of 0.08, 0.16, and 0.32 ml/min, respectively. This study highlights the potential of patient-specific CFD modeling to quantify embolization behavior and suggests that the injection rate of Onyx is a critical parameter warranting closer clinical attention. However, further research with improved boundary conditions, expanded patient cohorts, and experimental validation is required to confirm and generalize these findings.

Key words: Arteriovenous malformations – Endovascular embolization – Onyx injection velocity – Computational Fluid Dynamics – Multi-phase flow

Impact of Onyx Injection Velocity in Endovascular Embolization: a Computational Multi-Phase Flow Study of a Patient-Specific Arteriovenous Malformation

Kaat Wille

Promotors: prof. dr. ir. Charlotte Debbaut, prof. dr. Peter Vanlangenhove
Supervisors: ir. Jessie Duquesne, dr. ir. Danilo Babin, ir. Mohammadjavad Sedghizadeh, prof. ir. Vincent Keereman

Abstract – **Cerebral arteriovenous malformations are complex vascular abnormalities characterized by abnormal, direct connections between arteries and veins, disrupting normal blood flow and posing risks such as hemorrhage [1]. Endovascular embolization with Onyx, a liquid embolic agent, offers a minimally invasive method to occlude these malformations. Its success, however, depends on operator-controlled parameters [1]. Onyx injection velocity is hypothesized to be such an important parameter, but is currently not routinely monitored during procedures. This thesis examines how various Onyx injection velocities affect hemodynamics in a patient-specific case via computational fluid dynamics simulations with a Volume-of-Fluid approach for multi-phase modeling. Results indicate that the Onyx injection rate affects Onyx progression, distribution within the vasculature, and local pressure differences, highlighting it as a key parameter for further investigation. Additional research with expanded patient cohorts and experimental validation is required to generalize these findings.**

Key words – Arteriovenous malformations, Endovascular embolization, Onyx injection velocity, Computational Fluid Dynamics, Multi-phase flow

I. ENDOVASCULAR EMBOLIZATION TREATMENT FOR ARTERIOVENOUS MALFORMATIONS

Cerebral arteriovenous malformations (AVMs) are abnormal tangles of cerebral vessels, creating a direct artery-to-vein connection, bypassing the capillaries (Figure 1). They result in a high-flow, low-resistance shunt that disrupts normal hemodynamics and increases the risk of hemorrhage, seizures, headaches, and other neurological deficits [1].

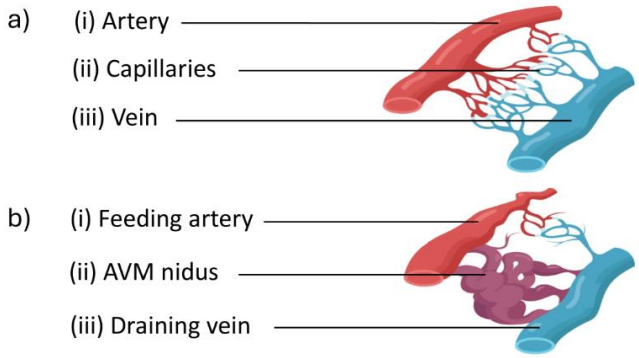

Figure 1. a) Normal situation: (i) arteries, (ii) capillaries, and (iii) veins. b) AVM: (i) feeding artery, (ii) nidus (core vessels), and (iii) draining vein. (Adapted from [2])

Endovascular embolization is a treatment method in which a liquid embolic agent, typically Onyx (an ethylene-vinyl alcohol copolymer (EVOH) dissolved in dimethyl sulfoxide (DMSO)), is injected into the AVM to solidify there, and consequently occlude blood flow to the AVM to create a safer hemodynamic situation [1].

II. COMPUTATIONAL MODELING FOR ENDOVASCULAR EMBOLIZATION

Clinical outcomes of embolization are dependent on the operator's experience in controlling parameters, such as the catheter placement and injection velocity [3]. This drives interest in quantification of certain procedural parameters, for which computational fluid dynamics (CFD) modeling is promising. Although the Food and Drug Administration (FDA) recommends an Onyx injection rate of 0.16 ml/min and states an upper limit of 0.30 ml/min (due to risks for angionecrosis and vasospasm observed in animal studies), injection velocity is not routinely monitored [4]. This thesis investigates the influence of the Onyx injection rate on embolic agent distribution and local hemodynamics in a patient-specific AVM through multi-phase flow CFD modeling.

III. GEOMETRY SEGMENTATION AND MESH GENERATION

The patient-specific AVM geometry was segmented based on 3D rotational angiography images using Mimics (Materialise NV, Leuven, Belgium). The feeding arteries and draining veins were determined from the patient's treatment reports and digital subtraction angiography images. There were two feeding arteries: one branch from the anterior cerebral artery (pericallosal artery, inlet1), and one branch from the middle cerebral artery (inlet 2); and two draining veins: one for deep venous drainage towards the great cerebral vein (outlet 1), and one for superficial venous drainage via a cortical vein towards the superior sagittal sinus (outlet 2). Two catheters were implemented using ANSYS Discovery (ANSYS Inc., Canonsburg, PA, USA) replicating their actual position during embolization. An optimal mesh was created using 3-Matic (Materialise NV, Leuven, Belgium) and Fluent Meshing (ANSYS Inc., Canonsburg, PA, USA), applying boundary layers (for fine sampling near the walls) and refinement around catheters. The final model is depicted in Figure 2.

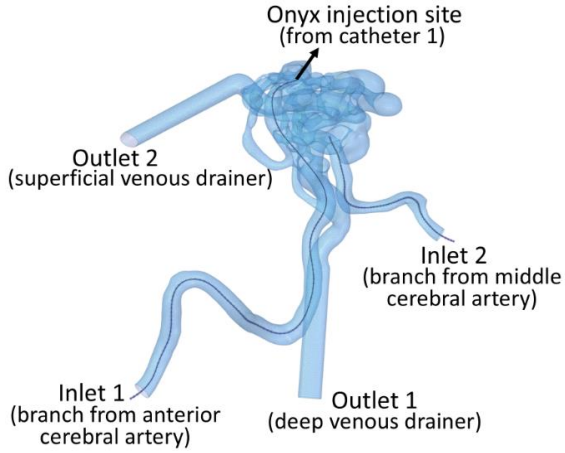

Figure 2. Final model for the patient-specific AVM with catheters.

IV. SIMULATION SETUP

Simulations for various Onyx injection rates were conducted: 0.08, 0.16 (FDA-recommended), and 0.32 ml/min. Table 1 outlines the key simulation settings. Multi-phase flow was modeled using ANSYS Fluent's Volume-of-Fluid method to represent blood and Onyx as immiscible phases. Onyx was assigned properties of Onyx-18 (6m% EVOH and 94 m% DMSO; with material properties defined as the mass-weighted averages of EVOH and DMSO properties).

Table 1. Settings for simulations

Material parameters	
Onyx	Density: 1103.9 kg/m^3, viscosity: 0.018 kg/(m·s)
Blood	Density: 1063.0 kg/m^3, viscosity: 0.004 kg/(m·s)
Boundary conditions	
Blood inlet	Velocity profiles from literature 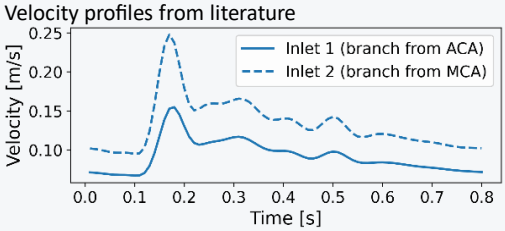
Onyx inlet	Constant injection rate: 0.08, 0.16, or 0.32 ml/min (0.16 ml/min is FDA-recommended [4])
Outlet	Outlet 1: -16.30 Pa, Outlet 2: -70.91 Pa Patient-specific pressures from a single-phase simulation using outflow fractions derived from digital subtraction angiography (as outflow fractions as boundary condition are not compatible with the Volume-of-Fluid method [5])
Walls	No-slip, rigid walls
Assumptions	
Fluid	Incompressible and Newtonian fluid
Flow	Laminar
Multi-phase flow: Onyx-blood interactions	
Model	Volume-of-Fluid model

V. RESULTS & DISCUSSION

A. Onyx Progression over Time for Various Injection Rates

To evaluate how the Onyx injection rate affects its progression and distribution within the AVM, Figure 3 visualizes the Onyx progression over time for three injection rates (0.08, 0.16, and 0.32 ml/min). Additionally, Table 2 quantifies the cumulative percentage of Onyx mass flowing through two downstream branches (branch 1 and 2 defined as indicated in Figure 3) over the period of one, two and three blood flow cycles.

Figure 3 illustrates that higher injection rates result in further Onyx progression over a certain time period. Qualitatively from Figure 3 and quantitatively from Table 2, it is also evident that for all injection rates, Onyx initially flows predominantly into branch 1, while over time a growing fraction is redirected toward branch 2. The initial favoring of branch 1 is likely due to the catheter position within the geometry, which is more oriented towards branch 1. The shift towards more flow going to branch 2 is likely due to an accumulation of Onyx in branch 1, leading to an increased flow resistance because of the higher viscosity of Onyx compared to blood, causing more flow towards branch 2, as flow follows the path of least resistance. This can be intuitively understood via Hagen-Poiseuille's law, which indicates that increased viscosity corresponds to increased vascular resistance (Equation 1 [6]).

Hagen-Poiseuille's law for resistance:

This law assumes steady, laminar flow of incompressible, Newtonian fluid through a cylindrical tube. However, the described relationships between these variables still provide valuable insights into the real blood flow dynamics in vessels, despite the strict assumptions not being satisfied.

$$R = \frac{8 \cdot \eta \cdot L}{\pi \cdot r^4} \qquad (1)$$

With R vascular resistance [Pa · s/m^3], r vessel radius [m], η dynamic viscosity [Pa · s], and L vessel length [m].

The Onyx injection rate influences the timing and extend of this redistribution: higher rates lead to faster Onyx accumulation in branch 1, and thus, a more rapid and pronounced redistribution to branch 2. Table 2 quantifies this trend: for example, after two cycles for a higher injection rate of 0.32 ml/min, the majority (57.93 %) of injected Onyx went to branch 2. In contrast, at the lower rate of 0.08 ml/min, branch 1 still received the majority (82.43 %) of injected Onyx over two blood flow cycles. These findings suggest important clinical implications. They highlight the Onyx injection rate as an important parameter that influences the Onyx progression and distribution over downstream branches. This suggests that uncontrolled or excessively high injection rates could potentially increase the risk of non-target embolization. So, both the catheter location and Onyx injection velocity are important parameters that need to be well-controlled for optimal embolization outcomes.

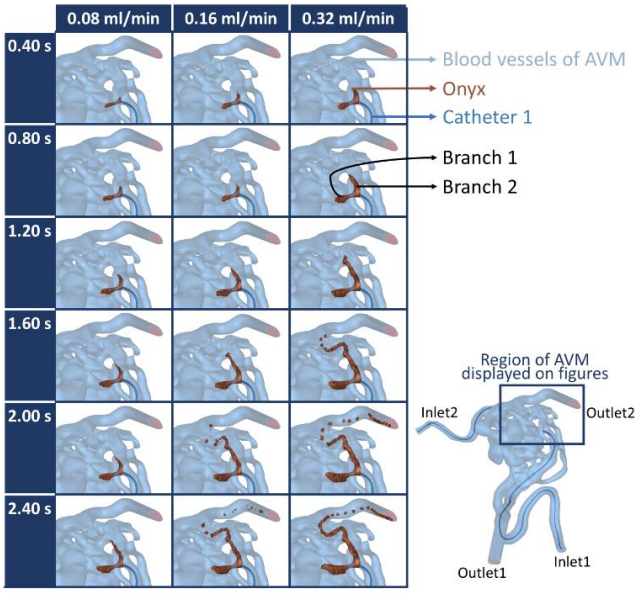

Figure 3. Progression of Onyx over time for various injection rates (0.08, 0.16, and 0.32 ml/min). The vessels of the AVM are seen in light blue and are made transparent to visualize Onyx in dark red and catheter 1 (from where Onyx is injected) in dark blue. The red color indicates cells that contain Onyx, but are not necessarily fully filled with Onyx: the criterion to indicate the cells red was a volume fraction for the Onyx phase greater than 10^{-6}. Branch 1 and 2 are indicated in black. On the bottom right, the zone of the AVM depicted in the pictures in the table is indicated.

Table 2. Mass distribution through branches after one, two and three blood flow cycles for different Onyx injection rates.

	0.08 ml/min		0.16 ml/min		0.32 ml/min	
	Branch 1	Branch 2	Branch 1	Branch 2	Branch 1	Branch 2
After 1 cycle (0.80 s)	93.66 %	6.34 %	76.60 %	23.40 %	51.86 %	48.14 %
After 2 cycles (1.60 s)	82.43 %	17.57 %	57.78 %	40.22 %	42.07 %	57.93 %
After 3 cycles (2.40 s)	74.35 %	25.65 %	51.02 %	48.98 %	39.06 %	60.94 %

B. Local Pressure Differences for Various Injection Rates

Figure 5.a indicates a small zone downstream of the injection site over which the pressure difference is determined (as the facet-averaged static pressure in plane 1A minus that in plane 1B), while Figure 5.b shows the pressure differences over this region over time for various injection rates.

Across all injection rates, pressure differences were consistently higher than in the baseline case before Onyx injection. This increase is likely attributed to the viscous Onyx occupying space within the vessel, raising local flow resistance, and consequently increasing pressure differences over the region. The increased vascular resistance because of increased viscosity can again be intuitively understood via Hagen-Poiseuille's law (Equation 1), while the increased pressure difference as a consequence of increased vascular resistance is supported by Ohm's law (Equation 2 [7]).

The fluid mechanical equivalent of Ohm's law:

$$R = \frac{\Delta P}{Q} \qquad (2)$$

With R flow resistance [Pa · s/m^3], ΔP pressure difference [Pa], and Q volumetric flow rate [m^3/s].

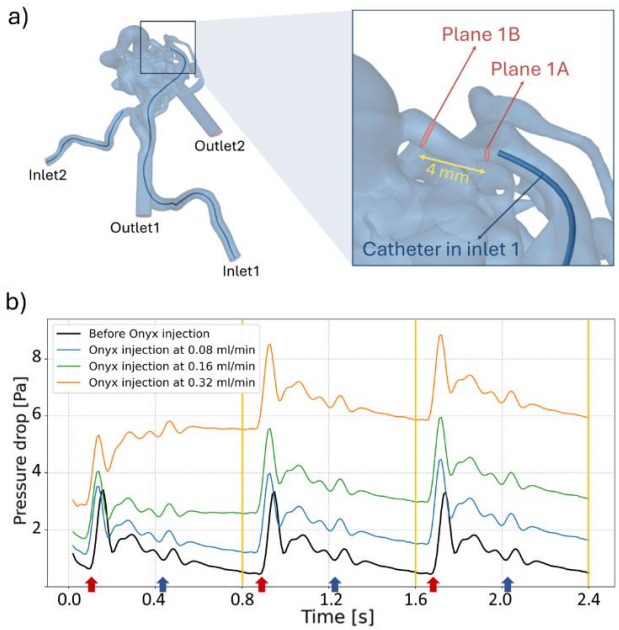

Figure 5. a) Two planes closely downstream of the injection site delimiting the zone over which the pressure difference is calculated. The yellow arrow indicates a distance of 4 mm. b) The pressure difference over zone in panel a) over time for the case before Onyx injection (black) and for various Onyx injection rates: 0.08, 0.16, and 0.32 ml/min (blue, green, and orange, respectively). The results are shown for three blood flow cycles (0.8 s each), with yellow vertical lines marking the end of each cycle, and the red and blue arrows on the time-axis marking the start of systole and diastole, respectively.

From Figure 5.b, it is evident that higher rates produce higher pressure differences, likely because more Onyx is introduced in a shorter time, increasing local resistance more rapidly. So, higher injection rates might challenge procedural safety, as elevated pressures are associated with hemorrhagic risks in this clinical context [4]. However, the absolute pressure differences remain small (maximum of 8.85 Pa for the highest injection rate), well below the accuracy limits of typical intracranial pressure transducers in the order of 100 Pa [8]. Perhaps this is partially due to the short simulation time (2.40 s) and limited length of the zone (4 mm). Future simulations over longer durations, considering larger zones, and including Onyx solidification might capture more pronounced and clinically relevant effects.

VI. LIMITATIONS & FUTURE WORK

This study presents valuable insights into the impact of Onyx injection rate on hemodynamics during AVM embolization; however, several limitations must be acknowledged. Model reconstruction was limited by the imaging resolution and inevitable geometric alterations introduced during segmentation and meshing. Moreover, boundary conditions should be further optimized in future work. Blood inlet velocity profiles were based on literature due to the lack of patient-specific dynamic imaging (e.g. 4D flow MRI [9]) or imaging frame rate data for the digital subtraction angiography, which could otherwise enable intensity-based mean velocity estimation in the feeding arteries [10]. Vessel walls were assumed rigid, although Fluid-Structure-Interaction would provide a more realistic representation [11]. Fixed outlet pressures were applied, but ideally time-varying pressures or flow-distribution-based outlet profiles would be used for greater physiological accuracy. Next, Onyx was simplified as a single-phase fluid without solidification. Future models should simulate its two-phase behavior (EVOH and DMSO) and viscosity increase as DMSO diffuses to improve realism. Moreover, several setup simplifications (e.g. Newtonian blood flow, laminar flow, and incompressibility) were deemed reasonable but inevitably limit realism. Future work should explore alternative workflows and validate them through in-vitro experiments with patient-specific 3D phantoms. Finally, validation across a larger number of patient-specific AVM cases is essential to ensure generalizability of the findings and clinical applicability.

VII. CONCLUSION

The findings confirm that Onyx injection rate is a critical parameter influencing embolic spread and local hemodynamics during AVM embolization. This suggests that Onyx injection rate is a clinically relevant factor to further examine and perhaps also monitor in the clinic. Overall, the results suggest that CFD modeling is a valuable tool for quantification in this clinical context, and in the long term has potential for patient-specific pretreatment planning, to optimize treatment efficacy and safety, by minimizing potential complications such as non-target embolization, suboptimal Onyx distribution, or vessel rupture. However, additional research with larger patient cohorts, optimized simulation protocols, and experimental validation are needed to generalize these findings and translate them into clinical practice.

REFERENCES

[1] Pinkiewicz, M., Walecki, J., & Zawadzki, M. (2022). State of the Art in the Role of Endovascular Embolization in the Management of Brain Arteriovenous Malformations—A Systematic Review. In Journal of Clinical Medicine (Vol. 11). MDPI. https://doi.org/10.3390/jcm11237208

[2] A. H. Care, "Arteriovenous malformation (avm)," n.d. [Online]. Available: https://www.aurorahealthcare.org/services/neuroscience/brain-skull-base-care/ cerebrovascular-malformations/arteriovenous-malformation

[3] L. Pierot, C. Cognard, D. Herbreteau, H. Fransen, W. J. V. Rooij, E. Boccardi, A. Beltramello, N. Sourour, K. Kupcs, A. Biondi, A. Bonaf´e, W. Reith, and A. Casasco, "Endovascular treatment of brain arteriovenous malformations using a liquid embolic agent: Results of a prospective, multicentre study (bravo)," European Radiology, vol. 23, pp. 2838–2845, 10 2013.

[4] Micro Therapeutics, Inc. (MTI), Onyx® Liquid Embolic System: Instructions
for Use, Medtronic, 2023, retrieved from product labeling. [Online]. Available:
https://www.accessdata.fda.gov/scripts/cdrh/cfdocs/cfpmn/pmn.cfm

[5] ANSYS Fluent Theory Guide, ANSYS Inc., 2013, release 15.0. [Online]. Available: https://www.ansys.com

[6] Klabunde, Richard E., "Determinants of resistance to flow (poiseuille's equation)," CV Physiology, 2023. [Online]. Available: https://cvphysiology.com/hemodynamics/h003

[7] Klabunde, Richard E., "Basic hemodynamic principles," CV Physiology, 2023.
[Online]. Available: https://cvphysiology.com/hemodynamics/h001

[8] L. Zacchetti, S. Magnoni, F. D. Corte, E. R. Zanier, and N. Stocchetti, "Accuracy of
intracranial pressure monitoring: Systematic review and meta-analysis," Critical Care,
vol. 19, 12 2015.

[9] A. G. Morgan, M. J. Thrippleton, J. M. Wardlaw, and I. Marshall, "4d flow mri for non-
invasive measurement of blood flow in the brain: A systematic review," pp. 206–218,
2 2021.

[10] C. Hoffman, S. Periyasamy, C. Longhurst, R. Medero, A. Roldan-Alzate, M. A. Speidel,
and P. F. Laeseke, "A technique for intra-procedural blood velocity quantitation using
time-resolved 2d digital subtraction angiography," CVIR Endovascular, vol. 4, no. 1,
p. 11, 2021. [Online]. Available: https://doi.org/10.1186/s42155-020-00058-7

[11] M. Hu, B. Chen, and Y. Luo, "Computational fluid dynamics modelling of hemody-
namics in aortic aneurysm and dissection: a review." Frontiers in bioengineering and biotechnology, vol. 13, p. 1556091, 2025

Contents

1 Arteriovenous Malformations **1**

1.1 Cerebral Arteriovenous Malformations 1

1.1.1 Introduction to Cerebral Arteriovenous Malformations 1

1.1.2 Epidemiology 3

1.1.3 Clinical Symptoms 4

1.1.4 Diagnosis 5

1.1.4.1 Computed Tomography 5

1.1.4.2 Magnetic Resonance Imaging 6

1.1.4.3 Angiography 7

1.1.5 Pathophysiology 7

1.1.6 Treatment 9

1.1.6.1 Microsurgery 12

1.1.6.2 Radiosurgery 14

1.1.6.3 Endovascular Embolization 15

1.2 Modeling of Arteriovenous Malformations 22

1.2.1 Limitations of the State of the Art for AVM Treatment 22

1.2.2 Computational Fluid Modeling of AVMs in Literature 22

1.2.3 Added Value of Computational Modeling 29

1.2.3.1 Importance of Personalized Medicine 29

1.2.3.2 Relevant Outcomes of Computational AVM Models 29

1.2.3.3 Long-term Goal 30

1.2.3.4 Current Bottlenecks 31

1.2.4 Goal of the Thesis 32

1.2.4.1 Case Description 32

2 Methods **34**
2.1 Mesh Generation . . . 34
2.1.1 Data Acquisition . . . 34
2.1.2 Geometry Segmentation . . . 35
2.1.3 Mesh Generation . . . 37
2.1.4 Introducing Catheters into the Model . . . 38
2.1.5 Mesh Sensitivity Analysis . . . 40
2.1.5.1 Mesh Sensitivity Analysis for Single-phase Case . . . 40
2.1.5.2 Mesh Sensitivity Analysis for Multi-phase Case . . . 41
2.2 Computer Simulations . . . 46
2.2.1 Multi-phase flow: Volume-of-Fluid method . . . 46
2.2.2 Simulation Setup . . . 48
2.2.3 Boundary Conditions . . . 48
2.2.3.1 Velocity Inlet Boundary Conditions for Blood . . . 48
2.2.3.2 Velocity Inlet Boundary Conditions for Onyx . . . 50
2.2.3.3 Vessel Wall Boundary Conditions . . . 50
2.2.3.4 Pressure Boundary Conditions . . . 51
2.2.4 Solution Methods for CFD Simulations . . . 52
2.2.5 Convergence assessment . . . 53
2.3 Methods for Quantification of Onyx Distribution . . . 54

3 Results and Discussion **56**
3.1 Results and Interpretation . . . 56
3.1.1 Baseline AVM Hemodynamics Prior to Onyx Injection . . . 56
3.1.1.1 Pressure contours at a Selected Time Point . . . 56
3.1.1.2 Velocity Path Lines at a Selected Time Point . . . 59
3.1.1.3 Outflow Fractions over Time . . . 61
3.1.2 Onyx Progression over Time for Various Injection Rates . . . 64
3.1.3 Local Pressure Differences for Various Injection Rates . . . 71
3.1.4 Implications for Clinical Practice . . . 76
3.2 Limitations . . . 77
3.2.1 Limitations of Model Reconstruction . . . 77
3.2.2 Assumptions of Boundary Conditions . . . 77
3.2.3 Assumptions in the Simulation Setup . . . 78
3.2.4 Scope Limited to a Single Case . . . 79

3.2.5 Simplifications in Onyx Modeling 79
3.3 Future Perspectives 80
3.3.1 Personalized Boundary Conditions 80
3.3.2 Wall Shear Stress Analysis: Preliminary Observations and Future Work 81
3.3.3 Expansion of patient cohort 83
3.3.4 Modeling the Onyx Solidification Process 83
3.3.5 Validation Through Experimental and Clinical Studies 83
3.3.6 Monitoring or Controlling Injection Rate 84
3.3.7 Optimizing Workflow Efficiency 84

4 Conclusion **85**

5 Societal Reflection **86**

Appendices **106**

A Additional Information on Tools and Settings in Mimics, 3-Matic, ANSYS Discovery, and Fluent Meshing **106**

B Workflow for Implementation of Catheters in ANSYS Discovery **109**

C Convergence Evaluation of CFD Simulations **112**

D Workflow in Fluent for Mass Flow Rate Calculations **115**

E Approval Letter from Ethics Committee **117**

List of Figures

1.1 **a)** Normal situation: (i) the artery delivers oxygenated blood, (ii) which flows through the capillaries, the site of nutrient and gas exchange, before (iii) draining into the vein for return to the heart. **b)** AVM: an abnormal connection where (i) the feeding artery delivers blood directly into (ii) the nidus, a tangled network of vessels that bypasses capillaries, and then into (iii) the draining vein, resulting in a high-flow, low-resistance shunt between the arterial and venous systems.
(Figure adapted from [1].) 2

1.2 The AVM under investigation for this thesis visualized by various imaging modalities: **a)** CT, **b)** MRI, specifically a T2-weighted turbo spin echo image, and **c)** angiography. 5

1.3 Illustration of various steps during microsurgical resection of AVMs. Via a craniotomy, the cortical surface of interest is exposed. Subarachnoid dissection (step 1) and pial dissection (step 2) take place. The feeding arteries and draining veins are closed off or clipped (step 3). The perinidal brain tissue is carefully dissected (step 4), and the nidus is then removed (step 5).
(Figure adapted from [2].) 13

1.4 Illustration of radiosurgery for AVM treatment. A typical approach for radiosurgery is using narrow beams of gamma radiation focussed on the AVM nidus that will in the long term (2 - 4 years) cause damage to the vessels of the AVM and will eventually close these vessels, if treatment is successful.
(Figure from [3].) 15

1.5 **a)** Endovascular embolization procedure performed using the trans-arterial route. **b)** Endovascular embolization procedure performed using the transvenous route (with balloon catheterization trans-arterially, sometimes used for assistance to control and slow down the blood flow to the AVM).
(Figure from [4].) 17

1.6 Overview of most commonly used embolic agents (non-liquid, adhesive liquid, and non-adhesive liquid) for endovascular embolization of AVMs. 18
1.7 **a)** Chemical structure of EVOH, with x the number of vinyl alcohol units ($-CH_2-CHOH-$) and y the number of ethylene units ($-CH_2-CH_2-$). **b)** Chemical structure of DMSO. **c)** Macroscopic appearance of Onyx. (Figure adapted from [5].) 19
1.8 Apollo Microcatheter with detachable tip. (Figure adapted from [6].) 21
1.9 Onyx progression over 0.45 s after the start of Onyx injection in the patient-specific AVM modeled by porous media. A1 and A2 indicate the arterial feeders and V1 indicates one of the venous drainers of the AVM (the second venous drainer is not visible in this specific visualization, as it is located at the back of the AVM). The purple zone indicates the cells in which Onyx is present. (Figure adapted from [7].) 25
1.10 Schematic of the injection progress and solidification progress of trans-arterial embolization from a certain feeding artery for patient 1 and patient 2. Two steps of injections of liquid embolic agents were simulated. The three columns left show 3D rendering (black) for volume fractions from 3 to 6 % of EVOH after the first injection and second injection at t = 15 s, 30 s, and 60 s for both patients. The last column shows 3D rendering for EVOH viscosity above 400 cP after the solidification of the first injection (red) and second injection (blue) for both patients. (Figure from [8].) 28
1.11 The patient-specific AVM under investigation for this thesis. **a)** Sagittal angiography image with black arrow indicating the nidus. **b)** Coronal DSA image with black arrow indicating the nidus and white arrows indicating the feeding arteries and draining veins: (i) feeding pericallosal artery, branch of the left ACA, (ii) feeding branch of the left MCA, (iii) deep venous drainage towards the great cerebral vein, and (iv) superficial venous drainage via a cortical vein towards the superior sagittal sinus. 33

2.1 One slice of the 3DRA imaging dataset with 256 × 256 pixels and slice thickness of 0.44 mm. The vasculature is visualized in white, while the surrounding tissue is visualized in black. 35

2.2 Initial threshold-based segmentation of the vasculature after using the 'Threshold' tool with a range of gray values from 1250 to 14084 on the provided 3DRA images of the patient. 36
2.3 **a)** Segmentation after removing vessels that are not of interest and smoothing. **b)** Segmentation after cutting in- and outlets. **c)** Segmentation after extruding the outlets. Outlet 1 (circular equivalent diameter of 2.99 mm) was extruded 14.95 mm, and outlet 2 (circular equivalent diameter of 3.31 mm) was extruded 16.55 mm. Inlet 1 corresponds to the feeder from the left ACA, inlet 2 to the feeder from the left MCA, outlet 1 to the deep draining vein towards the great cerebral vein, and outlet 2 to the superficial cortical draining vein. 36
2.4 **a)** 'Fix Wizard' panel for the final mesh in 3-Matic after the diagnostic options were reviewed and updated as needed. **b)** 'Histogram parameters' for the final mesh in 3-Matic, with the shape measure being 'Skewness'. 37
2.5 The final mesh after optimization in 3-Matic. The inlets and outlets are indicated. 37
2.6 **a)** An angiography image during embolization showing black dots corresponding to the locations of the beginnings and ends of the 15 mm detachable tips of the Apollo microcatheters. **b)** Model in ANSYS Discovery with catheters. The tip of the catheter in blood inlet 1, or the arterial feeder from the ACA, is indicated by the orange arrow; and the tip of the catheter in blood inlet 2, or the arterial feeder from the MCA, is indicated by the red arrow. 39
2.7 The final mesh from Fluent Meshing for the AVM geometry with the implemented catheters. The three boundary layers and mesh refinement around the catheters are apparent on the zoomed-in panels. 39
2.8 Percentual differences for local facet-averaged static pressures at in- and outlets for each mesh compared with the finest mesh in function of the number of mesh elements. The red dotted lines indicate +5 and -5 %. 41
2.9 Percentual differences for averages and 95th percentiles of global and local (in plane approximately through the middle of the nidus) velocities for each mesh compared with the finest mesh in function of the number of mesh elements. The red dotted lines indicate +5 and -5 %. 42

2.10 Percentual differences for averages and 95th percentiles of global and local (in planes in each of the in- and outlet vessels positioned close to the nidus) pressures for each mesh compared with the finest mesh in function of the number of mesh elements. The red dotted lines indicate +5 and -5 %. . . . 43
2.11 Percentual differences for averages and 95th percentiles of global and local (in plane after the Onyx inlet from catheter 1) volume fractions of the blood phase for each mesh compared with the finest mesh in function of the number of mesh elements. The red dotted lines indicate +5 and -5 %. 44
2.12 Percentual differences for averages and 95th percentiles of global and local (in plane after the Onyx inlet from catheter 1) volume fractions of the Onyx phase for each mesh compared with the finest mesh in function of the number of mesh elements. The red dotted lines indicate +5 and -5 %. 45
2.13 A schematic representation of the simplified cerebral arterial tree and corresponding segment numbering from the Stergiopulos/Reymond model. Data for segments 78 and 73 are extracted, representing segment 2 of the ACA and segment 1 of the MCA, respectively.
(Figure from [9]) 49
2.14 Input velocity profiles over time implemented as boundary conditions for blood in inlet 1 from the ACA (continuous line) and in inlet 2 from the MCA (dashed line). 50
2.15 Two successive DSA images used to estimate the percentages of outflow in both of the outlets. 52
2.16 Indication of the two branches after the injection site and the location of the planes in each branch over which the mass flow rates were calculated. 54

3.1 **a)** The chosen time point for figure in panel b) is shown on the inlet velocity profiles: 0.40 s into the second blood flow cycle with inlet velocities near average values. **b)** Static pressure contours on the AVM vessel walls, with a color scale from -100 Pa (deep blue) to 500 Pa (dark red). Orange lines indicate planes in all in-and outlets close to the nidus, while pink lines indicate the in- and outlets, for which the facet-averaged static pressures are indicated (these values were calculated over the whole cross-section, not only the outer vessel wall). 58

3.2 **a)** The chosen time point for figure in panel b) is shown on the inlet velocity profiles: 0.40 s into the second blood flow cycle with inlet velocities near average values. **b)** Path lines through the AVM geometry, with color indicating velocity magnitudes from 0 m/s (deep blue) to 0.4335 m/s (dark red) and arrows indicating flow directions. 60

3.3 Outflow fractions to outlets 1 and 2 over time for two blood flow cycles, indicated in full and dashed black lines, respectively. The inlet velocity profiles at inlets 1 and 2 are also added in this figure (full and dashed light blue lines, respectively) to provide some context on the timeline. Outlet 1 is the deep venous drainer towards the great cerebral vein, outlet 2 the superficial cortical venous drainer going towards the superior sagittal sinus, inlet 1 the branch from the ACA, and inlet 2 the branch from the MCA. 61

3.4 Flow path lines through the AVM geometry, colored by their velocity magnitudes from 0 m/s (deep blue) to 0.4335 m/s (dark red) and arrows indicating flow directions. The left panel indicates flow path lines coming from both inlets of the model. The middle panel selectively shows the flow path lines coming from inlet 1 (branch of the ACA). The right panel selectively shows the flow path lines coming from inlet 2 (branch of the MCA). Outlet 1 is the deep venous drainer towards the great cerebral vein, outlet 2 the superficial cortical venous drainer going towards the superior sagittal sinus, inlet 1 the branch from the ACA, and inlet 2 the branch from the MCA. 63

3.5 Progression of Onyx over time for various injection rates (0.08, 0.16, and 0.32 ml/min). The vessels of the AVM are seen in light blue and are made transparent to visualize Onyx in dark red and catheter 1 (from where Onyx is injected) in dark blue. The red color indicates cells that contain Onyx, but are not necessarily fully filled with Onyx: the criterion to indicate the cells red was a volume fraction for the Onyx phase greater than 10^{-6}. On the bottom right, the zone of the AVM depicted in the pictures in the table is indicated (same zone as in Figure 3.6). 68

3.6 Spread of Onyx over time visualized in various planes around the injection site for various injection rates (0.08, 0.16, and 0.32 ml/min). The vessels of the AVM are seen in light blue and are made transparent to visualize catheter 1 (from where Onyx is injected) in dark blue and the volume fraction of Onyx in the defined planes. For the volume fractions, a deep blue color indicates 0 % Onyx in the cell (i.e. fully filled with blood) and a dark red color indicates 100 % Onyx in the cell. On the bottom right, the zone of the AVM depicted in the pictures in the table is shown (same zone as in Figure 3.5). 69

3.7 **a)** Indication of the two branches after the injection site and the location of the planes in each branch over which the mass flow rates are calculated. **b)** Cumulative fractions of injected Onyx mass through branches 1 (solid bars) versus 2 (dashed bars) over time for three blood flow cycles (2.40 s in total) for various Onyx injection rates (0.08, 0.16, and 0.32 ml/min in blue, green, and orange, respectively). At each time point, the height of the bar for a specific branch and a specific injection rate represents the fraction of the total injected mass (up to that time and for that injection rate) that has passed through that specific branch. 70

3.8 **a)** Two planes downstream of the injection site delimiting the zone over which pressure difference (i.e. facet-averaged static pressure in plane 1A minus plane 1B) is calculated. The yellow arrow indicates a distance of 4 mm. **b)** The pressure difference over zone in panel a) over time for the case before Onyx injection (black) and for various Onyx injection rates: 0.08, 0.16, and 0.32 ml/min (blue, green, and orange, respectively). Yellow vertical lines mark the end of each 0.80 s cardiac cycle, and red and blue arrows on the time-axis mark the start of systole and diastole, respectively. **c)** Boxplots of the pressure difference ratios for injection rates of 0.08 ml/min (blue) and 0.32 ml/min (orange), relative to the recommended rate of 0.16 ml/min (Equation 3.2). Each boxplot shows the distribution of this ratio for a specific injection rate over a 0.80 s interval corresponding to either cycle 1, 2, or 3. Values for the mean, minimum, and maximum are shown to the right of each boxplot. A horizontal dashed green line denotes the reference ratio of 1. 75

3.9 The WSS on the outer vessel walls of the AVM around the injection site over time for various injection rates (0.08, 0.16, and 0.32 ml/min). The WSS is indicated by a color scale from deep blue for 0.0 Pa to dark red for 10.0 Pa (legend for all figures is shown on the upper right). On the bottom right, the zone of the AVM depicted in the pictures in the table is shown. 82

C.1 Blood velocity at inlet 1 (branch from ACA) over time for three blood flow cycles with each point representing a simulation time step (of 0.10 s) for the simulation with only blood (before any Onyx injection). Green indicates time steps where full convergence was achieved (residuals relatively dropped by three orders of magnitude for continuity and velocity components), while red indicates time steps that did not meet the convergence criterion. 113

C.2 Blood velocity at inlet 1 (branch from ACA) over time for three blood flow cycles with each point representing a simulation time step (of 0.10 s) for the simulations with Onyx injected at **a)** 0.08 ml/min, **b)** 0.16 ml/min, and **c)** 0.32 ml/min. Green indicates time steps where full convergence was achieved (residuals dropped by three orders of magnitude for continuity and velocity components), while red indicates time steps that did not meet the convergence criterion. 114

List of Tables

1.1 SM grading system for AVMs based on AVM size, eloquence of adjacent brain tissue, and type of venous drainage. The summation of the points per category results in an SM grade from I to V. 10
1.2 Properties of Onyx-18, Onyx-20, and Onyx-34 20

2.1 Mesh parameters and cell counts of meshes for the single-phase flow case. (Curvature 1 refers to the outer surface of the model, curvature 2 refers to the in- and outlets, and curvature 3 refers to the catheters.) 41
2.2 Mesh parameters and cell counts of meshes for the multi-phase flow case. (Curvature 1 refers to the outer surface of the model, curvature 2 refers to the in- and outlets, and curvature 3 refers to the catheters.) 42
2.3 Material parameters of blood and Onyx phase. 48
2.4 Amount of converged time steps per conducted simulation. The convergence criterion was defined as a relative drop of at least three orders of magnitude for all residuals. 53

3.1 Mass distribution through branches indicated in Figure 3.7.a over one cycle (0.80 s), two cycles (1.60 s), and three cycles (2.40 s) for various Onyx injection rates. 67

A.1 Overview of operations in Mimics with explanations and relevant settings. . 107
A.2 Overview of operations in 3-Matic with explanations and relevant settings. . 107
A.3 Overview of meshing operations in Fluent Meshing with explanations and relevant settings. 108
A.4 Overview of operations in Ansys Discovery with explanations. 108

C.1 Amount of converged time steps per conducted simulation. The convergence criterion was defined as a drop of at least three orders of magnitude for all residuals. 113

Abbreviations

Chapter 1: Arteriovenous Malformations

AVM	Arteriovenous Malformation
AVF	Arteriovenous Fistula
VEGF	Vascular Endothelial Growth Factor
MRI	Magnetic Resonance Imaging
CTA	Computed Tomography Angiography
DSA	Digital Subtraction Angiography
CT	Computed Tomography
HU	Houndsfield Units
MAP	Mean Arterial Pressure
CPP	Cerebral Perfusion Pressure
ICP	Intracranial Pressure
CBF	Cerebral Blood Flow
SM	Spetzler-Martin (grading system)
WSS	Wall Shear Stress
NBCA	N-butyl Cyanoacrylate
LEA	Liquid Embolic Agent
EVOH	Ethylene-Vinyl Alcohol Copolymer
DMSO	Dimethyl Sulfoxide
FDA	Food and Drug Administration
CFD	Computational Fluid Dynamics
3DRA	3D rotational angiography
VOF	Volume-of-Fluid
FSI	Fluid-Structure Interaction
AI	Artificial Intelligence
ACA	Anterior Cerebral Artery
MCA	Middle Cerebral Artery

Chapter 2: Methods

MSA	Mesh Sensitivity Analysis

Chapter 5: Societal Reflection

SDG	Sustainable Development Goal

Chapter 1

Arteriovenous Malformations

1.1 Cerebral Arteriovenous Malformations

1.1.1 Introduction to Cerebral Arteriovenous Malformations

Vascular malformations are abnormalities in blood vessel development that result from errors in vascular morphogenesis, of which arteriovenous anomalies are one type, alongside venous malformations, cavernous malformations, and telangiectasia [10–12]. Arteriovenous anomalies—vascular malformations involving abnormal connections between arteries and veins—are broadly categorized into arteriovenous malformations (AVMs) and arteriovenous fistulas (AVFs). AVFs are direct connections between arterial and venous systems without a complex network of vessels [11, 13–15]. AVMs, on the other hand, are abnormal complexes of arteries and veins that are directly connected through a network of tangled vessels (Figure 1.1.b), rather than through the intervening capillary beds, as usual (Figure 1.1.a) [10–12]. Although precise epidemiological data on the prevalence of cerebral AVFs versus cerebral AVMs are missing, the literature suggests that AVMs are more prevalent, and they also constitute the primary focus of this thesis [11,14,15]. Moreover, several sources indicate that fistulous lesions are more commonly observed in pediatric populations, while complex network AVM lesions are more frequently encountered in adults, although precise statistics are lacking [11, 14, 15]. Vascular malformations, including AVMs, pose an ongoing threat to the patient (hemorrhage is the most common symptom, but also headaches, seizures, or neurological deficits) and should be treated if possible, for instance, by endovascular embolization [4, 10, 11, 16, 17].

The arterial system carries oxygen-rich blood from the heart to the tissues in the body, whereas the venous system returns deoxygenated blood from the tissues back to the heart. Typically, these two systems only communicate through the capillaries, where oxygen and

nutrient exchange takes place. Direct communication between these systems is typically prevented by regulatory mechanisms (e.g. the vascular endothelial growth factor (VEGF) signaling pathway) that inhibit vascular malformations, but in some individuals, errors in these control systems lead to the formation of AVMs [11,18]. AVM formation leads to a high-flow, low-resistance shunt between the arterial and venous systems, bypassing the capillary network and disrupting normal blood circulation [10].

Structurally, an AVM consists of three main components: (i) the feeding arteries, (ii) the nidus, and (iii) the draining veins (Figure 1.1.b). The nidus is the central part of the AVM, consisting of abnormal tangles of blood vessels directly connecting the arteries and veins [1, 11]. The feeding arteries (also called feeders) are typically enlarged vessels that supply blood to the AVM. These can be classified as direct feeding arteries, which end in the AVM, or indirect feeding arteries, which continue to supply blood towards normal brain tissue [1,11]. Lastly, draining veins (or drainers) are typically dilated vessels that drain blood from the AVM [1, 11].

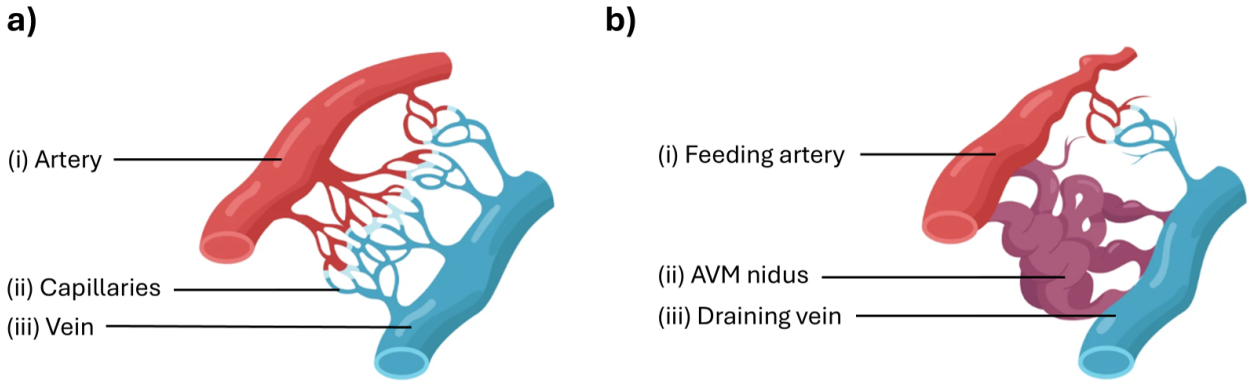

Figure 1.1: a) Normal situation: (i) the artery delivers oxygenated blood, (ii) which flows through the capillaries, the site of nutrient and gas exchange, before (iii) draining into the vein for return to the heart. **b)** AVM: an abnormal connection where (i) the feeding artery delivers blood directly into (ii) the nidus, a tangled network of vessels that bypasses capillaries, and then into (iii) the draining vein, resulting in a high-flow, low-resistance shunt between the arterial and venous systems.
(Figure adapted from [1].)

The precise pathogenesis and pathophysiology of AVMs remain not fully understood. However, they were believed to be congenital (i.e. present from birth) malformations for a long time. It is hypothesized that malformations may result from disruption in vascular communication during embryogenesis, when the arteries and veins are in direct contact. AVMs develop if this abnormal connection remains after birth due to atypical vascular maturation.

Another hypothesis is that structural defects or signaling errors caused by underlying genetic abnormalities contribute to AVM formation. However, some studies opposed a family risk factor [10, 11], leading to ongoing debate regarding the role of genetics in AVM formation. Another potential cause of AVMs is injury or trauma [10, 11].

The sizes of AVMs can vary widely, ranging from small AVMs of less than 1 cm in diameter to giant AVMs that occupy multiple lobes within the brain [10]. AVMs may appear in the brain or in the spinal cord. Cerebral AVMs are most commonly located in the cerebral hemispheres, although they can also appear in the cerebellum or brain stem [10]. For the remainder of this work, 'AVM' will always refer to cerebral AVMs.

1.1.2 Epidemiology

The worldwide incidence (i.e. the number of new cerebral AVM cases occurring in a given population over a specific time period) is estimated to be between 0.9 and 1.4 per 100 000 person-years over various population-based studies [10, 11, 17, 19–24], while the prevalence (i.e. the total number of existing cases in the population at a given time) is determined to be in the range of 5 to 50 per 100 000 individuals [10,11,17,20]. The rarity of cerebral AVMs and consequent lack of large-scale epidemiological research pose challenges in accurately determining the true incidence and prevalence of the condition [10, 19]. However, recent advancements in diagnostic magnetic resonance imaging (MRI) and other high-resolution imaging techniques, such as computed tomography angiography (CTA) and digital subtraction angiography (DSA), have facilitated the detection of unruptured and asymptomatic AVMs [11], while the incidence of ruptured AVMs has always been rather stable over time (around 0.51 to 0.55 per 100 000 person-years) [10, 11, 21, 24, 25].

Although AVMs are generally present at birth, most natural history studies indicate that they are often diagnosed in younger adults of 20 to 40 years [10, 11, 19, 26].

Most studies suggest there is no significant sex dependency in the occurrence of AVMs, as men and women are equally likely to develop these malformations [10, 11, 19].

Hemorrhage associated with AVMs has mortality rates ranging from 10 to 30 % and morbidity rates ranging from 20 to 30 % [10, 11, 27–29]. Various factors such as previous rupture, deep location (e.g. nearby the basal ganglia, thalamus, or insula), deep venous drainage (i.e. when some or all drainage is through deep veins such as the internal cerebral veins, basal veins, or precentral cerebral vein), associated aneurysms, and pregnancy can considerably decrease the survival rates (see Section 1.1.3 *Clinical Symptoms*) [10, 11, 30–32]. Furthermore, significant morbidity (e.g. seizures, headaches, and neurological deficits) is

linked to AVMs, even in unruptured cases (more on this in Section 1.1.3 *Clinical Symptoms*).

1.1.3 Clinical Symptoms

AVMs cause a wide range of clinical symptoms because of their heterogeneity in location, size, and other features.

Hemorrhage is the most common (initial) clinical presentation associated with AVMs, occurring in approximately 50 % of patients [10,11,17,33]. Although AVMs are relatively rare, they are a major cause of hemorrhage in young, otherwise healthy individuals, accounting for up to 33 % of all hemorrhagic strokes in this group [10, 24, 34]. AVM-related hemorrhages typically present as intracerebral hemorrhages and less commonly as subarachnoid or intraventricular bleeding [10, 35].

The annual bleeding risk for patients with previously unruptured AVMs is around 1 %, but prior hemorrhage increases this risk significantly, particularly in the first year after hemorrhage, when the re-rupture rates can range from around 6 to 15.8 % [10,11,36]. However, the influence of this factor on the hemorrhage risk gradually diminishes again over time [10, 11].

Pregnancy is generally considered a risk factor for AVM-related hemorrhage [10, 37, 38]. While the precise mechanisms are unclear, Can et al. (2017) hypothesized that significant physiological alterations of the cardiovascular, hormonal, and hemostatic-thrombotic systems play a role [10]. Furthermore, deep location of the AVM is associated with increased hemorrhage risk, as well as deep venous drainage, which leads to increased pressure gradients over the AVM due to the fewer venous pathways causing a reduced drainage area [10,11,35,39,40]. Moreover, associated aneurysms are also proven to be a risk factor. These aneurysms can be found in the nidus, in feeding arteries or draining veins, or even in surrounding vessels [10, 11, 17, 40]. While some debate exists regarding risk factors for AVM-related hemorrhage, age and sex are generally not considered to significantly influence the likelihood of bleeding [10, 39, 40]. Although certain studies suggest that older age may be associated with increased hemorrhage risk, robust evidence from large-scale studies is lacking. However, elderly patients may experience poorer outcomes following treatment [10].

Seizures are the second most common (first) clinical manifestation of AVMs with an occurrence ranging from 17 to 31 % [10, 11, 17, 35]. The exact mechanisms by which seizures are caused by AVMs remain unclear. Various studies have suggested larger AVM size as a risk factor. Also, frontal, temporal, or superficial location, as well as prior hemorrhage, are considered risk factors for presenting with seizures as a clinical manifestation [10, 33, 41].

In addition, headaches appear (as the first symptom) in approximately 6 to 14 % of

patients with AVM, while focal neurologic deficits and ischemia manifest (as the first clinical manifestation) in approximately 3 to 10 % of patients [10, 11, 17, 35].

Some other less prevalent clinical symptoms include cognitive dysfunction and disordered behavior, movement disorders, and pulsatile tinnitus [10]. Neurological deficits, such as cognitive or motor disorders and seizures, and the psychological burden of having an AVM can severely influence the quality of life of patients, for example, by causing anxiety or the inability to live independently in their daily life [10, 11].

1.1.4 Diagnosis

Accurate diagnosis and characterization of AVMs rely on medical imaging techniques, which are essential to visualize the nidus, feeding arteries, draining veins, and adjacent brain tissue. The most used diagnostic tools include computed tomography (CT), MRI, and angiography. Figure 1.2 depicts the AVM under investigation for this thesis with various imaging modalities. The principles and strengths of each modality are briefly discussed in the following paragraphs.

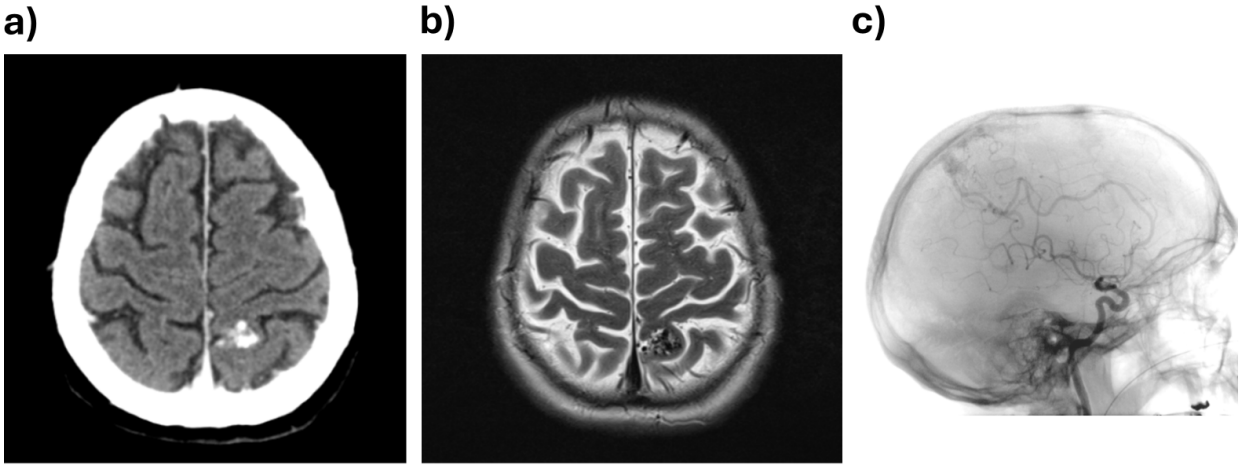

Figure 1.2: The AVM under investigation for this thesis visualized by various imaging modalities: **a)** CT, **b)** MRI, specifically a T2-weighted turbo spin echo image, and **c)** angiography.

1.1.4.1 Computed Tomography

CT imaging creates a pixel-by-pixel map of X-ray beam attenuation in Hounsfield units (HU) by rotating an X-ray source around the patient. X-ray measurements are taken from multiple angles, each representing a projection of the beam through the body at a specific orientation.

Typically around 1000 projections are taken over a whole rotation, which are then processed to reconstruct detailed cross-sectional images (or slices) of internal structures [42, 43].

CT imaging is mostly utilized as a first-line imaging modality in emergency settings when acute intracranial hemorrhage is suspected (typically in patients with acute headaches or loss of consciousness), as CT scans are faster and more readily available than other imaging methods [11,24]. Furthermore, also in non-urgent cases where MRI is contraindicated (e.g. in patients with non-MRI-compatible implants), CT is the imaging modality of choice [11, 24].

If bleeding is confirmed by the CT scan, CT angiography can be subsequently performed, using injection of contrast dye to identify the AVM's architecture, the precise region of hemorrhage, and potentially aneurysms or other vulnerable sites [11, 24, 35]. If the source of bleeding cannot be detected from CT or CT angiography, DSA can be conducted to identify the location of bleeding and the features of the AVM [24]. After discovering hemorrhage, the main goal is to detect the sensitive sites and secure these (typically by endovascular embolization) [24]. However, if these imaging modalities do not indicate bleeding but an AVM is nonetheless expected, MRI will be conducted [24].

Perfusion CT is a special case of CT imaging involving rapid repeated CT scans and the use of a contrast dye. This modality enables visualization of brain perfusion and can point out various abnormal perfusion patterns in the adjacent brain tissues. For example, functional steal (redirection of blood flow from surrounding brain tissue towards the AVM, often associated with seizures) is shown by reduced cerebral blood flow, cerebral blood volume and mean transit time; ischemic steal (redirection of blood flow towards the AVM causing a lack of oxygen towards surrounding brain tissues, often associated with neurological deficits) is shown by decreased cerebral blood flow and cerebral blood volume, but by increased mean transit time; and venous congestion (accumulation of blood in the venous system causing venous hypertension) is shown by increased cerebral blood volume and increased mean transit time [11, 24].

1.1.4.2 Magnetic Resonance Imaging

MRI is a non-invasive imaging technique to visualize soft tissues using strong magnetic fields (typically 1.5 or 3 T) and radio waves (wavelengths around 4.7 meters for 1.5 T or 2.3 meters for 3 T systems) to exploit the magnetic properties of hydrogen atoms in the body [44]. When placed in a strong magnetic field, hydrogen nuclei align with the field; radio-frequency pulses then disturb this alignment, and the nuclei emit signals when they return to their original state, which can be detected and converted into images [11, 45].

MRI is a popular imaging modality for initial detection of AVMs or to investigate AVMs and the surrounding parenchymal tissue due to its non-invasive nature and ability to visualize soft tissues. In particular, MRI can be used to discover evidence of potential prior hemorrhage or brain edema [11, 24]. A special type of MRI, magnetic resonance venography, uses intravenous contrast dye to assess venous outlet obstruction and sinus thrombosis (i.e. blood clot formation in the brain's venous sinuses [46]). MRI is typically used for patients with suspected AVMs experiencing non-acute symptoms, for example, unexplained headaches, seizures, or neurological deficits, but will not be the method of choice in acute hemorrhagic situations due to long acquisition times [11].

1.1.4.3 Angiography

Angiography provides high-resolution, real-time imaging of the vasculature in the brain using X-rays and injection of contrast agents via a catheter [47]. Angiography is the most invasive modality of the ones mentioned here, but it also provides additional insights and superior spatial resolution (typically in a range of 0.2 to 0.6 mm) [7, 11, 48]. A specific type is DSA, which subtracts images acquired prior to contrast injection (called a mask) from the angiography images during contrast injection to visualize progression of the contrast (typically iodine-based contrast) with superior spatial resolution (in the range of 0.25 to 0.5 mm) [24, 49–51].

Angiography is used during endovascular treatment or to map the vasculature for surgical planning. In particular, angiography, or more specifically DSA, is used to assess the nature (direct or indirect) and number of feeding arteries, the nature (deep or superficial) of venous drainage, and the presence of aneurysms, and to get insights into the flow patterns within the AVM [7, 11, 24, 48].

1.1.5 Pathophysiology

The presence of AVMs can significantly alter the blood flow dynamics in surrounding vessels. However, there is considerable uncertainty when it comes to the exact mechanisms that are at the base of certain pathophysiological changes due to AVMs. In this section, the main phenomena of the pathophysiology of AVMs are discussed, being high-flow shunt, vascular steal, venous hypertension, and disrupted autoregulation [11].

High-flow shunt: An AVM is a tangle of vessels directly connecting arteries and veins, bypassing the normal capillary bed. Since the diameters of nidal vessels (in the order of

0.1 to 10 mm [52, 53]) are bigger than those of capillaries (around 2 to 5 µm [54]) and flow resistance is inversely related to vessel diameter (Equations 1.1 to 1.3 [55–57]), the nidus presents lower blood flow resistance compared to a healthy situation. This makes an AVM a high-flow shunt between the arterial and venous systems, which can significantly disrupt normal cerebral blood flow and increase hemorrhage risks (see Section 1.1.3 *Clinical Symptoms*) [11, 58].

Ohm's law for fluid flo(w:

$$R = \frac{\Delta P}{Q} \tag{1.1}$$

With R flow resistance [$\mathrm{Pa} \cdot \mathrm{s/m^3}$], ΔP pressure difference [Pa], and Q volumetric flow rate [$\mathrm{m^3/s}$].

Hagen–Poiseuille's law:

Theoretical assumptions of this law are steady, laminar flow of incompressible, Newtonian fluid through a tube with a uniform circular cross-sectional area. However, the principles of the relationship between pressure, flow, and resistance still provide valuable insights into the real blood flow dynamics in vessels, despite the strict assumptions not being satisfied.

$$Q = \frac{\Delta P \cdot \pi \cdot r^4}{8 \cdot \eta \cdot L} \tag{1.2}$$

With ΔP pressure difference [Pa], r vessel radius [m], η dynamic viscosity [$\mathrm{Pa} \cdot \mathrm{s}$], and L vessel length [m].

Resistance from Hagen–Poiseuille's and Ohm's law:

$$R = \frac{8 \cdot \eta \cdot L}{\pi \cdot r^4} \tag{1.3}$$

With R flow resistance [$\mathrm{Pa} \cdot \mathrm{s/m^3}$], η dynamic viscosity [$\mathrm{Pa} \cdot \mathrm{s}$], L vessel length [m], and r vessel radius [m].

Vascular steal: As AVMs are low-resistance, high-flow shunts, they draw blood away from nearby vessels, thereby reducing perfusion to surrounding brain tissue, as flow follows the path of least resistance [59]. These surrounding brain regions are at risk of hypoperfusion (i.e. inadequate blood flow resulting in insufficient delivery of oxygen and nutrients), which

is referred to as the steal phenomenon, since AVMs 'steal' the blood flow that was actually destined for healthy brain parenchyma in the surroundings [11].

Venous hypertension: AVMs directly link the high-pressure arterial and low-pressure venous systems, causing venous hypertension (i.e. increased pressure in the veins), diverting more cerebral blood flow towards veins, and causing vein enlargement [8, 58].

Autoregulation: Autoregulatory mechanisms that maintain a stable blood flow in the cerebral vasculature despite fluctuations in blood pressure [60], can be disrupted by the presence of AVMs [61–63]. For instance, if blood pressure rises, vascular resistance should rise as well, by vasoconstriction (i.e. reduction in diameter) of arteries and arterioles to stabilize the blood flow (see relationship between resistance and vessel diameter in Equation 1.3). Normal values for the mean arterial pressure (MAP, i.e. the average arterial blood pressure during a single cardiac cycle) are 70 to 100 mm Hg [64], for the cerebral perfusion pressure (CPP, i.e. net pressure gradient that drives blood flow to the brain) these lie between 60 and 80 mm Hg [64], and for intracranial pressure (ICP, i.e. the pressure within the skull) these range between 5 and 10 mm Hg [64], while normal average cerebral blood flow (CBF) is around 50 ml/100 g/min [65, 66]. The relationship between these pressures is given by CPP = MAP - ICP, so CPP expresses how much effective pressure is available to drive blood through the brain. In healthy individuals, autoregulation can maintain normal values for CBF and CPP for MAPs ranging from 50 to 150 mm Hg [64]. However, vessels surrounding AVMs are often enlarged, fragile, and prone to rupture or aneurysms, potentially resulting in impaired autoregulation [61–63].

1.1.6 Treatment

The main therapeutic goal of any approach to AVM treatment is complete obliteration of the malformation. Treatment that results in only partial obliteration not only puts the patient at risk of rupture and bleeding but also subjects them to treatment-related risks (e.g. blood loss or damage to surrounding brain tissue for microsurgery, radiation damage to healthy surrounding neuronal tissue for radiosurgery, hemorrhage, ischemia, or vessel perforation due to catheter maneuvering for endovascular embolization, etc.) [11, 17]. However, sometimes several treatment sessions are necessary to achieve full occlusion or resection of the AVM in order to avoid drastic changes to the hemodynamics by altering the situation too much in one procedure [67–69].

Current treatment options for AVMs include observation with medical management, treatment by microsurgical resection (Section 1.1.6.1 *Microsurgery*), radiosurgery (Section 1.1.6.2 *Radiosurgery*), endovascular embolization procedures (Section 1.1.6.3 *Endovascular Embolization*), or a combination of these approaches. Treatment selection is generally done by a multidisciplinary team (consisting of neurosurgeons, radiotherapists, and interventional radiologists), based on established grading systems, mainly considering the size and location of the AVMs [24,33]. A thorough understanding of the disease's natural history is imperative, as the spontaneous rupture risk must be carefully weighed against potential treatment-related risks for various treatments [24, 33].

Grading systems: To minimize complications and optimize treatment outcomes, several grading systems have been proposed to help the multidisciplinary team determine the complexity of AVMs and assess the safety and feasibility of various interventions by considering relevant criteria for AVM complexity and intervention-related risks [11, 24].

The Spetzler-Martin (SM) grading system is the most widely used classification method to evaluate AVMs. This grading system was developed by Dr. Spetzler and Dr. Martin in 1986 [70] and is based on three key features: size ($<$ 3 cm: 1 point, 3-6 cm: 2 points, $>$ 6 cm: 3 points), eloquence or functional importance of adjacent brain tissue (non-eloquent area: 0 points, eloquent area: 1 point), and venous drainage pattern (superficial/ into cortical veins: 0 points, deep drainage/ into deep structures: 1 point) (Table 1.1). The resulting score—by adding up the points for these three categories—indicates a grade from I to V, with a lower grade indicating reduced peri- and postsurgical complication risks, such as hemorrhage [11, 17, 24, 70].

Table 1.1: SM grading system for AVMs based on AVM size, eloquence of adjacent brain tissue, and type of venous drainage. The summation of the points per category results in an SM grade from I to V.

Feature	**Category**	**Points**
AVM size	$<$ 3 cm	1
	3 - 6 cm	2
	$>$ 6 cm	3
Eloquence of adjacent tissue	Non-eloquent area	0
	Eloquent area	1
Venous drainage	Superficial/cortical veins	0
	Deep venous drainage	1

In addition to the SM grading system, other grading systems have been developed. For instance, the Lawton-Young grading system also accounts for age, hemorrhagic presentation, and compactness [71, 72]. The Buffalo score is used to estimate the endovascular treatment complication rate for AVMs and incorporates features that complicate an angiographic approach (e.g. number of arterial pedicles (i.e. an artery directly supplying blood to AVM, which can be branch of a larger artery), diameter of pedicles, and the eloquence of brain tissue at the nidus) [17, 24, 73]. Furthermore, a three-tier system is often used for treatment decisions, with class A (SM grades I and II; suitable for microsurgical resection), B (SM grade III, suitable for multimodal treatment), and C (SM grades IV and V, suitable for observation) [11, 17, 24].

Microsurgery and radiosurgery are considered for AVMs of SM grades I and II, while, typically, endovascular embolization is considered a safe and effective treatment for AVMs of SM grade III, which can be performed as a stand-alone treatment or in combination with microsurgical resection or radiosurgery [10, 11, 24]. For AVMs of SM grades IV and V, generally, observation with medical management is the preferred method in case of no imminent rupture risk, as interventions are associated with too high risks (e.g. treatment-related thrombosis or hemorrhage) compared to the potential benefits in these specific cases [10, 11, 24]. In these cases, symptoms are controlled (e.g. with pain medication for headaches or anti-epileptic drugs for seizures), and, in some cases, the patient is advised to avoid activities associated with increased ICP and increased risks for head traumas or injuries [10, 11, 24, 74].

Treatment evaluation: To evaluate the outcome of an intervention, imaging techniques are standard practice to confirm obliteration of the AVM and to rule out posttreatment hemorrhage. The most important imaging modality for incomplete obliteration detection is angiography, which provides detailed images of the resulting vascular architecture, but MRI and CT angiography are also valuable for evaluation. Typically, patient follow-up involves a control MR, angiography, and/or CT one day after intervention, followed by a repeat MR and XA 6 months later. After complete obliteration is confirmed, it is standard practice to conduct an MRI annually and an angiography two or three times a year [11, 24]. Upon awakening of the patient in the recovery room or, in some cases, in the intensive care unit, functional outcomes and the overall recovery of a patient are evaluated. Scales like the Modified Rankin Scale, which measures disability or dependence in daily activities from 0 (no disability) to 6 (death), and the Glasgow Outcome Scale, which measures overall functional recovery from 1 (death) to 5 (good recovery), can be utilized [11].

1.1.6.1 Microsurgery

Microsurgery, or microsurgical resection, is a first treatment possibility for AVMs. This modality used to be the gold standard in the past and is still quite often used, either as a stand-alone treatment or in combination with, for example, embolization. Microsurgery is today still often used for AVMs with SM grades I and II, located in the cerebellum, subarachnoid cisterna, and pial surfaces of the brain stem [75]. Surgery comes with inherent risks (including intraoperative or postoperative hemorrhage, vascular complications, and seizure development), so sufficient operator experience and skill are crucial for successful treatment [17].

Preoperative planning involves advanced imaging techniques such as CT, MRI, or angiography to map the critical vasculature (feeding arteries, draining veins, nidus, and surrounding vasculature) in sufficient detail. During surgery, the patient is under general anesthesia, and via a craniotomy, the cortical surface of interest is exposed. Figure 1.3 illustrates various steps during the microsurgical resection procedure [11]. First, subarachnoid dissection (step 1) and definition of the feeding arteries and primary draining vein—which need to be preserved until the end of the procedure—take place. Next, pial dissection (step 2) occurs. After this, the feeding arteries are closed and the secondary draining veins are trimmed (step 3). During parenchymal dissection, perinidal brain tissue is carefully dissected to free the AVM (step 4). Finally, ependymal or deep dissection takes place if necessary to avoid residual vascular malformations. For the final resection, the nidus is removed (step 5), and the primary draining vein is occluded [11].

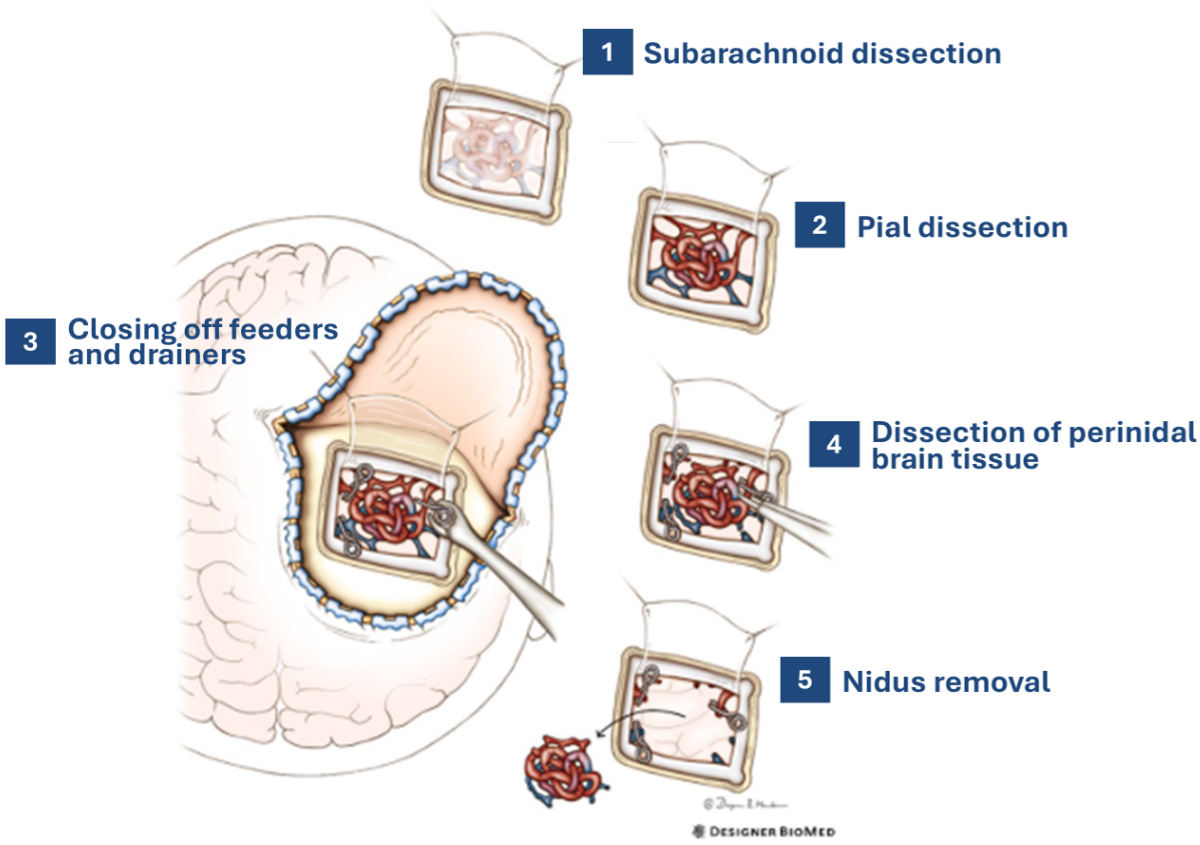

Figure 1.3: Illustration of various steps during microsurgical resection of AVMs. Via a craniotomy, the cortical surface of interest is exposed. Subarachnoid dissection (step 1) and pial dissection (step 2) take place. The feeding arteries and draining veins are closed off or clipped (step 3). The perinidal brain tissue is carefully dissected (step 4), and the nidus is then removed (step 5).
(Figure adapted from [2].)

1.1.6.2 Radiosurgery

Secondly, radiosurgery can be performed alone or in combination with, for example, embolization to treat AVMs. Generally, radiosurgery is considered for AVMs with SM grades I and II, in cases where the AVM is located superficially and the surrounding brain tissue is non-eloquent, because of radiation risks (e.g. brain edema and radiation necrosis) [76]. Specifically, AVMs less than 3 cm in diameter are suited, as larger AVMs would require too high doses causing radiation risks [76, 77]. For larger AVMs, for example embolization is needed prior to the radiosurgery [11, 24, 76, 77].

Radiosurgery uses precise, image-guided delivery of a radiation dose to the vessels composing the AVM to obliterate it by damaging the vessels by slowly inducing fibrosis and thickening and shrinkage of these vessels to close them off over time [78]. Because of these gradual radiation-induced biological changes, complete obliteration of the AVM typically takes 2 to 4 years [11, 17, 24]. So, because radiation dose is limited to protect surrounding brain tissue, the therapeutic effect takes longer to develop, making radiosurgery unsuitable for urgent cases [11, 17, 24].

Gamma knife radiosurgery is a typical radiosurgery procedure to obliterate AVMs, where the patient's head is placed inside a helmet, and stereotactic frame placement is used to deliver targeted gamma radiation to the AVM (Figure 1.4) [3, 79, 80].

The goal is to achieve low healthy tissue damage but high obliteration rates; therefore, careful pretreatment planning and high-resolution imaging are crucial. Two key principles are applied in practice to maximize damage to the target while preserving healthy tissue (i.e. minimizing radiation necrosis): 1) volume-staged radiosurgery: large AVMs are divided into smaller parts that are treated sequentially in various sessions using relatively lower doses, 2) dose-staged radiosurgery: large AVMs are treated by hypofractionated radiosurgery, i.e. division of radiation dose into multiple consecutive lower doses applied to the entire volume (typically a number of approximately four fractions is standard) [11, 79, 81].

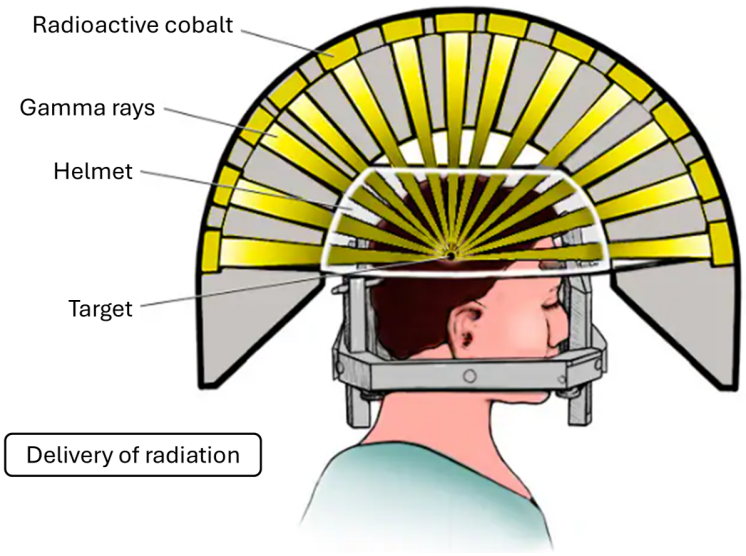

Figure 1.4: Illustration of radiosurgery for AVM treatment. A typical approach for radiosurgery is using narrow beams of gamma radiation focussed on the AVM nidus that will in the long term (2 - 4 years) cause damage to the vessels of the AVM and will eventually close these vessels, if treatment is successful.
(Figure from [3].)

1.1.6.3 Endovascular Embolization

Finally, endovascular embolization treatment will be discussed, which is a minimally invasive procedure. This thesis focuses on AVMs treated by this specific procedure.

Currently, minimally invasive procedures have gained significant popularity because of relatively low complication rates (3.9 % rate of death or permanent damage per patient based on the Brain Vascular Malformation Study Group database from the University of Toronto [82]) and faster patient recovery times (hospitalization of 1-2 days for endovascular embolization [83–86] compared to 3-15 days for microsurgery [87,88]) . Reasons for reduced complication rates associated with minimally invasive interventions include reduced tissue trauma, a more targeted approach, reduced blood loss compared to open surgery, and a more immediate effect compared to radiosurgery [89, 90]. In the field of neuro-interventions, catheter-based procedures such as embolization have become standard therapeutic approaches for AVMs of SM grade III (as a stand-alone procedure or combined with other modalities) [90–93].

Despite the benefits, these kinds of procedures still present some challenges. Catheter navigation in the small and tortuous brain vasculature is a very complex process that requires a high level of operator skill and experience. Difficulties in catheter navigation cause prolonged procedure times and result in an associated increased radiation exposure from

imaging [94–96]. Furthermore, suboptimal catheter positioning can increase the risks of incomplete embolization, recanalization (i.e. reopening of previously occluded vessels), reflux (i.e. retrograde flow of embolic agent), and even rupture [17]. These complications can alter the hemodynamics (for example, properties such as flow and wall shear stress (WSS)) within the AVM and its surroundings [17].

Embolization procedure: Endovascular embolization is performed as both a planned or an emergency procedure. Detailed preoperative imaging is imperative for vasculature mapping. In emergency settings, only a CT is done preoperatively, but for a planned procedure, a combination of a CT, angiography, and/or MRI is commonly conducted. During the procedure, the patient is sedated, and an anesthetist is present throughout the whole procedure [97]. Generally, the patient is brought to hypotension (i.e. MAP below 70 mmHg) during the procedure to avoid high pressures on the wall, reduce risks for hemorrhage, and reduce shunting of embolic agent towards the veins [97–100].

Catheter insertion is performed under angiographic guidance using one of two approaches: 1) the trans-arterial route (Figure 1.5.a), or 2) the trans-venous route (Figure 1.5.b) [4, 11, 17, 24]. The trans-arterial route used to be the standard approach, typically via the femoral artery [11, 17, 24], but nowadays the trans-venous approach has gained popularity [101–104]. The choice between trans-arterial or trans-venous depends on the specific AVM geometry and accessibility [11, 17].

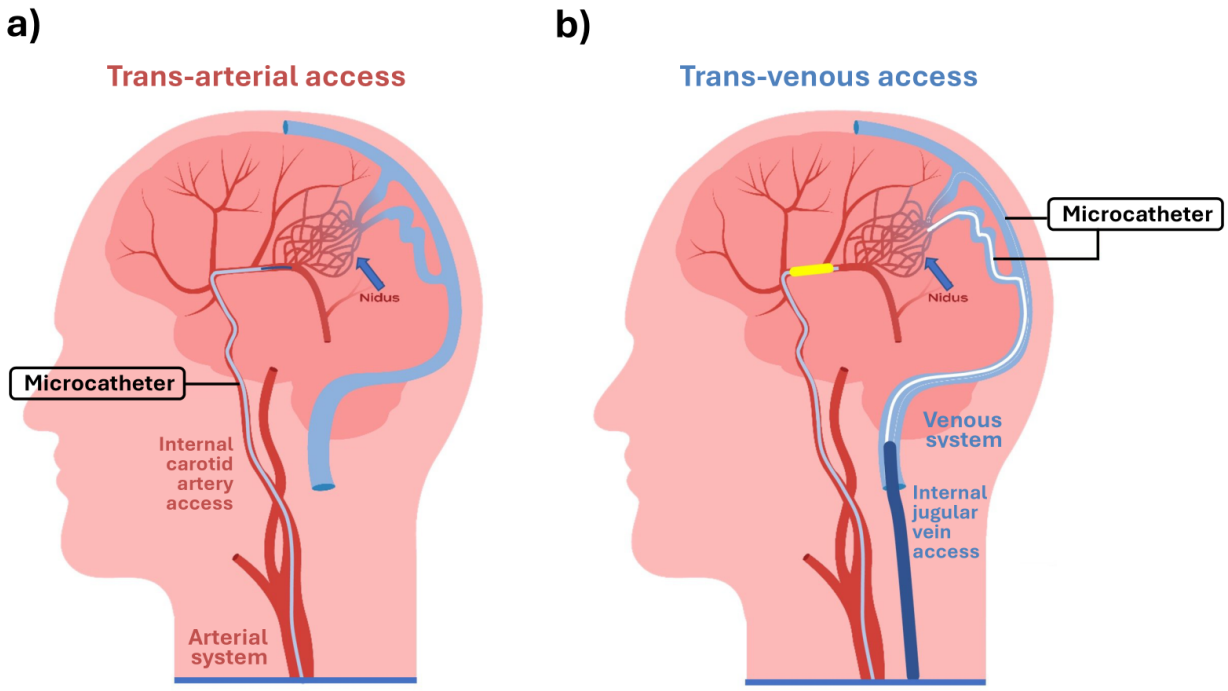

Figure 1.5: a) Endovascular embolization procedure performed using the trans-arterial route. **b)** Endovascular embolization procedure performed using the trans-venous route (with balloon catheterization trans-arterially, sometimes used for assistance to control and slow down the blood flow to the AVM).
(Figure from [4].)

The procedure involves the injection of an embolic agent such as N-butyl cyanoacrylate (NBCA) or Onyx (Medtronic, Dublin, Ireland) to occlude the AVM nidus by blocking the feeding arteries while avoiding migration of embolic agents into the draining veins [5, 11, 17, 105]. Larger vessels are typically occluded first, followed by smaller vessels as pressure increases (or, less commonly, as the injected material's viscosity decreases) [105]. An endovascular embolization intervention is deemed sufficient when no contrast is observed going through the draining veins on the angiography [8, 106].

Multiple embolization interventions are sometimes required, especially for larger AVMs, which are often treated in different stages, with each session potentially targeting a distinct portion of the AVM. The aim of this staged approach is to avoid too drastic alterations of the cerebral blood flow dynamics [67, 68]. Furthermore, over time, occluded blood vessels might open up again as a result of a foreign body reaction [107] (i.e. inflammatory response, involving macrophages and giant cells against body-foreign material, resulting in fibrosis (i.e. scarring) and granuloma formation (i.e. group of immune cells), aiming to degrade the foreign material [108]). In this case, the body will attempt to degrade the embolic material,

so repeated embolization or another type of treatment might be required to reinforce vessel occlusion and limit the body's ability to attack the embolic agent [107].

Embolic agents: The choice of embolic agents is crucial for good treatment outcomes. Embolic agents can be classified as liquid or non-liquid, and liquid embolic agents (LEAs) as adhesive or non-adhesive (Figure 1.6). Non-adhesive LEAs do not tend to stick to the vessel wall, causing an easier spread in the vasculature and allowing more controlled filling of the vessels, but also increasing their risk of migration. On the other hand, adhesive LEAs are based on cyanoacrylate and do tend to stick to the vessel walls. These agents solidify more rapidly upon contact with blood [105].

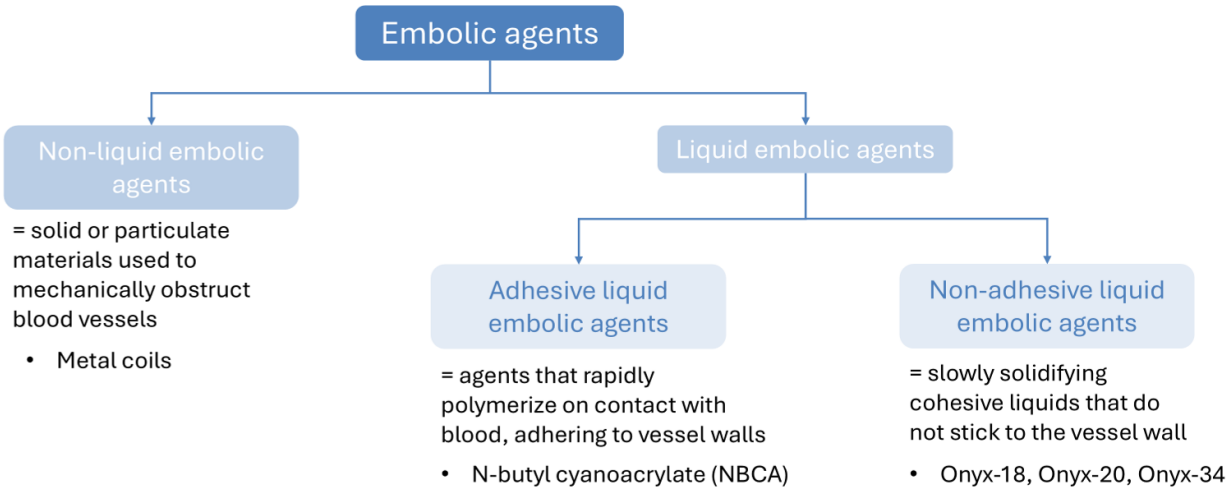

Figure 1.6: Overview of most commonly used embolic agents (non-liquid, adhesive liquid, and non-adhesive liquid) for endovascular embolization of AVMs.

The most commonly used embolic agents are:

- **Non-liquid embolic agents:**

  Metal coils: Metal coils can be deployed to provide mechanical occlusion and prevent distal embolization by migration of LEAs. A specific type of embolization treatment, termed the 'Pressure Cooker Technique', focuses on a more comprehensive, forceful, and controlled Onyx embolization by trapping a detachable catheter tip using glue and coils to create an anti-reflux plug [16].

- **Adhesive liquid embolic agents:**

  N-butyl cyanoacrylate: NBCA is a fast-acting adhesive liquid embolic agent that rapidly polymerizes via an exothermic reaction (i.e. with heat release) upon contact with blood (due to the alkaline ionic composition of blood) and solidifies. To decrease

the polymerization time, thus decreasing the released heat, and to make it radio-opaque, NBCA is mixed together with ethiodized oil. Before injection, the catheter must be flushed with an acidic nonionic solution (e.g. 5 % dextrose in water). Typically, a detachable-tip microcatheter is employed, so the catheter can be removed quickly after deployment to prevent it from being glued in place, while the tip of the catheter remains inside the body [17].

- **Non-adhesive embolic agents:**

  Onyx: Onyx is a widely used non-adhesive liquid embolic agent. This pasty suspension consists of ethylene-vinyl alcohol copolymer (EVOH; chemical structure in Figure 1.7.a) and tantalum powder (added for visualization) dissolved in dimethyl sulfoxide (DMSO; chemical structure Figure 1.7.b) [5,105]. Following injection, DMSO leaves the mixture since it is highly miscible in aqueous fluids such as blood. Consequently, the EVOH solidifies, since EVOH is miscible in DMSO but not in blood [5, 105]. Generally, solidification occurs within five minutes, causing vessel occlusion [5]. The addition of homogeneously dispersed tantalum powder particles ensures radiopacity of the embolic agent for visualization during the procedure [5, 105]. The macroscopic appearance of Onyx is shown in Figure 1.7.c.

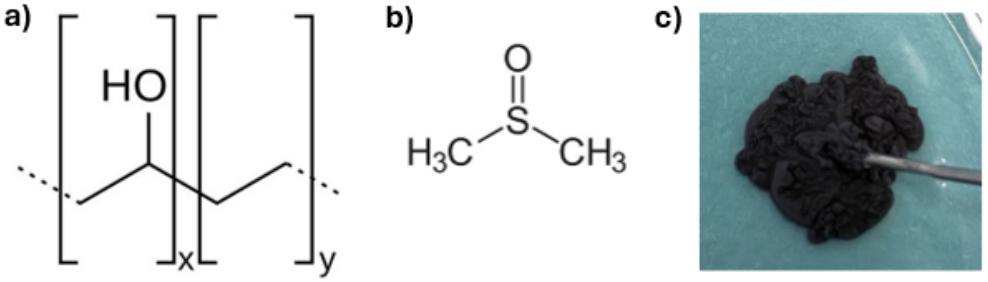

Figure 1.7: a) Chemical structure of EVOH, with x the number of vinyl alcohol units ($-CH_2-CHOH-$) and y the number of ethylene units ($-CH_2-CH_2-$). **b)** Chemical structure of DMSO. **c)** Macroscopic appearance of Onyx. (Figure adapted from [5].)

Three different compositions of Onyx are commercially available: Onyx-18, Onyx-20, and Onyx-34 (see Table 1.2 for composition and properties) [5,8,106]. The number mentioned in the name of the product refers to its viscosity in centipoise (at 40°C), so a higher amount of EVOH corresponds to a higher viscosity and, consequently, a shorter solidification time. The viscosity of Onyx is also temperature dependent: the viscosity decreases with increasing temperature. The density of DMSO equals 1100 kg/m^3, while the density of EVOH is in the range of 1140 to 1190 kg/m^3 (for further

calculations here the mean value of 1165 kg/m^3 was considered) [109, 110]. The most commonly used formulation for the embolization of AVMs is Onyx-18 (composition of 6 m% EVOH and 94 m% DMSO) [5, 7, 16, 106].

Table 1.2: Properties of Onyx-18, Onyx-20, and Onyx-34

	Onyx-18	**Onyx-20**	**Onyx-34**
EVOH content [mass %]	6	6.5	8
DMSO content [mass %]	94	93.5	92
Viscosity (at 40°C) [Pa.s]	0.018	0.020	0.034
Density of suspension [kg/m^3]	1103.9	1104.2	1105.2

Around 20 minutes before use, Onyx is placed in a shaker to ensure homogeneous distribution of tantalum particles in the suspension to guarantee accurate visualization of the embolic agent during the procedure [5]. For this reason, long procedure durations should be avoided, as after a certain duration the tantalum particles are not homogeneously distributed anymore, which can have a negative impact on the visibility. Before injection, the microcatheter is flushed with DMSO to prevent precipitation of Onyx inside the microcatheter. Typically, Onyx is injected very slowly over several minutes to prevent reflux and distal embolization [16, 17]. An injection flow rate of 0.16 ml/min is recommended by the Food and Drug Administration (FDA), and an upper limit of 0.30 ml/min is stated, as rates above this value have been shown to lead to vasospasm (i.e. narrowing of blood vessels, linked with risks for ischemia [111]) and/or angionecrosis (i.e. death of blood vessel tissue, linked with risks for leakage or rupture [112]) in animal studies [106, 113, 114]. Furthermore, it is advised to put pressure on the plunger of the syringe using only the thumb when injecting Onyx, and to not interrupt injection for longer than two minutes, since excessive pressurization may lead to catheter rupture [106, 113, 114]. Within a single embolization procedure, Onyx can be injected in various steps (for instance, via different arterial feeders or draining veins) until full occlusion is achieved [106, 113–115]. There is no strict universal upper limit on the amount of Onyx injected during one procedure; however, a retrospective single-center study including 250 cases of endovascular embolization using Onyx (type not specified) indicated that the volumes of injected Onyx ranged from 1 to 10 ml [115], and another single-center study including 82 patients treated with endovascular embolization using Onyx (type not specified) indicated an average amount of 2.6 ml injected Onyx [116]

The use of an Apollo Microcatheter (Medtronic, Dublin, Ireland) with a detachable tip of 15 or 30 mm is recommended (Figure 1.8) [6, 117]. This type of microcatheter is

DMSO compatible and can be retracted while the tip stays inside the vessel, which reduces the risk for catheter retraction (i.e. when microcatheter becomes stuck and cannot be safely withdrawn, which can lead to thromboembolisms) and disrupted hemodynamics, as well as the risk for Onyx reflux [6, 118]. It is advised to wait a few seconds to retrieve the catheter after completion of Onyx injection to avoid fragmentation and migration [106]. Furthermore, it is interesting to note that Onyx solidifies progressively from the outer layer to the inner core. Consequently, a blood vessel appearing completely opaque during the procedure might not be fully embolized yet, as a slightly perfused central core could still remain [5, 7]. Because of this, angiography is employed to confirm vessel occlusion by evaluating any residual contrast passage through the vessel [8, 106].

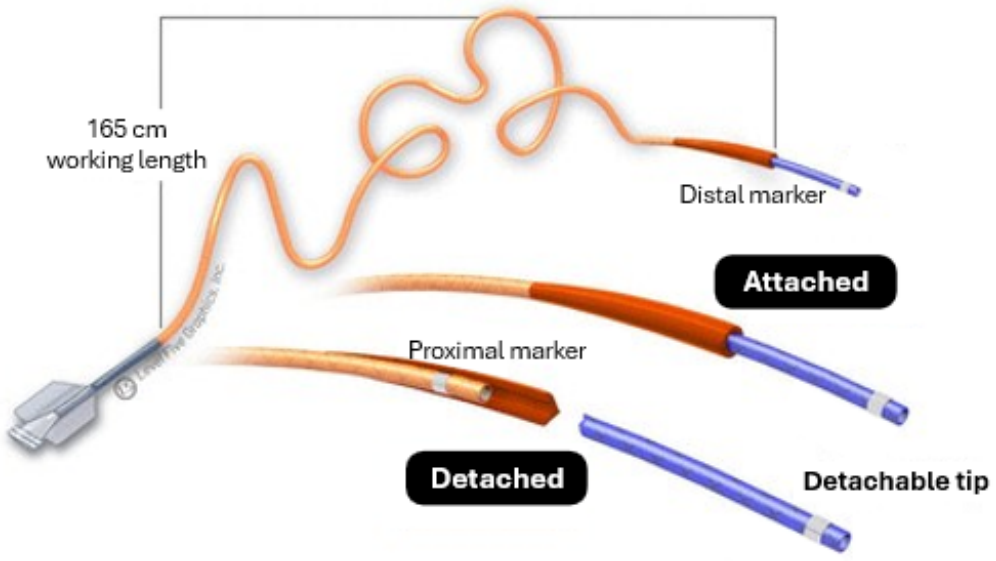

Figure 1.8: Apollo Microcatheter with detachable tip.
(Figure adapted from [6].)

A prospective multicenter study considering 117 patients, called the BRAVO (BRain ArterioVenous malformations embolization with Onyx) study, evaluated the safety and efficacy of the use of Onyx (type not specified) in AVM embolization treatments. Treatment with only embolization led to complete obliteration in 23.5 % of the cases. Morbidity and mortality rates of respectively 5.1 % and 4.3 % were observed, which is deemed acceptable for this kind of procedure [119].

1.2 Modeling of Arteriovenous Malformations

1.2.1 Limitations of the State of the Art for AVM Treatment

As previously stated, minimally invasive embolization procedures have become standard treatment for AVMs due to their lower complication rates and faster patient recovery. However, several challenges remain related to these procedures. Catheter navigation through the delicate cerebral vasculature requires careful handling and a high degree of expertise to avoid prolonged procedure times and associated increased radiation exposures [6, 118, 119]. Furthermore, there is a risk for incomplete embolization, which may lead to complex and potentially dangerous hemodynamic alterations within the vasculature [6, 107, 118, 119].

As a result, there is a strong interest in improved methods for procedural planning and catheter navigation. Achieving shorter neuro-intervention times (and consequently minimizing radiation exposure), together with increasing the chances of complete embolization, are key improvements that should be investigated. Detailed vasculature mapping tools and cerebral blood flow modeling are particularly promising to achieve these goals, especially using a patient-specific approach tailored to the unique vascular anatomy and hemodynamics of the patient.

1.2.2 Computational Fluid Modeling of AVMs in Literature

While research on computational fluid modeling (CFD) within the context of AVMs is limited, some notable studies exist in literature.

First, Orlowski et al. (2011) developed three patient-specific computational AVM models to investigate the hemodynamics in AVMs [120]. In this study, only blood flow through the nidus was investigated, while embolic agents were not considered. The nidus was modeled using the principle of porous media, since a realistic geometry extraction was not possible due to the insufficient resolution of the 3D rotational angiography (3DRA) data in the order of 0.6 mm. The extraction of parameters (i.e. porosity and permeability) was based on the intensities of the voxels from the 3DRA images (voxels of $0.578 \times 0.578 \times 0.578$ mm). In this study, the behavior of porous media implementation was first tested by simulations on four simplified, or idealized, digital phantoms. Blood was treated as an incompressible Newtonian fluid with a constant viscosity of 0.004 Pa.s (= 4 cP), although the apparent viscosity in vessels with diameters around 0.05 to 0.15 mm would probably be more in the order of 10 to 50 % of this value due to non-Newtonian effects [120, 121].

Further, boundary conditions for flow were set by manually assigning flow values to vessels based on the 3DRA images, and vessels without measurable flow were given a background noise-level flow from phase contrast magnetic resonance angiography images.

This study validated the simulation results using clinical 3DRA and 2D angiography imaging data, and 22 out of 24 determined flow paths were claimed to be very probable to be accurate. However, the main limitation of this study was the absence of embolic agents in the simulations.

In the next year, Orlowski et al. (2012) investigated two aspects of AVM treatment planning: simulation of an LEA (being Onyx) transport and simulation of change in blood flow due to embolization [7]. The propagation was modeled using two-fluid modeling and scalar transport. The two-fluid model computed the flow of blood and LEA within a domain by solving continuity and mass conservation equations. In parallel, scalar transport was used to model the movement of a passive substance, representing DMSO, injected alongside Onyx. This scalar is transported by convection and diffusion, over a velocity field determined by the fluid flow. The velocity field was obtained through the simultaneous solution of mass and momentum conservation equations for both blood and Onyx. The solidification was modeled by an increase in viscosity, which was assumed to only depend on the composition (i.e. increased viscosity if lower DMSO content, so higher EVOH content); while the temperature dependency (i.e. increased viscosity for increased temperature) was ignored. Both linear and exponential models were explored to describe the viscosity increase as a function of the DMSO content decrease; with the DMSO content influenced by the concentration of the scalar.

Two-fluid model equations:

Continuity equation:

$$\frac{\partial \alpha_k}{\partial t} + \nabla \cdot (\alpha_k \mathbf{u}_k) = 0 \tag{1.4}$$

Conservation of mass equation:

$$\frac{\partial (\rho_k \alpha_k \mathbf{u}_k)}{\partial t} + \nabla \cdot (\rho_k \alpha_k \mathbf{u}_k \mathbf{u}_k) = \nabla \cdot (\alpha_k \boldsymbol{\tau}_k) - \alpha_k \nabla p + \mathbf{F}_k \tag{1.5}$$

Condition for volume fractions:

$$\alpha_b + \alpha_s = 1 \tag{1.6}$$

With k indication of the phase (b for blood and s for solvent (or Onyx), α_k volume fraction of phase k [-], $\mathbf{u}_k$ velocity of phase k [m/s], ρ_k density of phase k [kg/m^3], $\boldsymbol{\tau}_k$ stress tensor of phase k [Pa], p pressure [Pa], and $\mathbf{F}_k$ additional forces (e.g. interphase slip) [N/m^3].

Relation between scalar concentration and Onyx viscosity:

For linear relationship:

$$\mu_i(t) = \mu_{\text{Onyx}} \cdot (1 + \beta \cdot (1 - \gamma_{s,i}(t))) \tag{1.7}$$

For exponential relationship:

$$\mu_i(t) = \mu_{\text{Onyx}} \cdot \beta^{(1-\gamma_{s,i}(t))} \tag{1.8}$$

With $\mu_i(t)$ viscosity at cell i and time t [Pa $\cdot$ s], μ_{Onyx} initial viscosity of Onyx [Pa $\cdot$ s], $\gamma_{s,i}(t)$ scalar (DMSO) concentration at cell i and time t with ($0 \leq \gamma_s \leq 1$) [-], β model parameter defining the maximum viscosity increase [-].

Various pressure and flow boundary conditions and various solidification models (scenarios 1 - 4) were investigated using digital phantoms (simplified 2D representations of AVMs composed of tubular in- and outlets and a rectangular chamber):

- Scenario 1: Onyx injected at constant speed (0.15 m/s) into still blood through one inlet, with a linear solidification model, and zero-pressure at outlet.
- Scenario 2: Onyx injected with constant pressure (50 Pa) into still blood through one inlet, with a linear solidification model, and zero-pressure at outlet.
- Scenario 3: Onyx injected with constant pressure (50 Pa) into still blood through one inlet, with an exponential solidification model, and zero-pressure at outlet.
- Scenario 4: Onyx injected with constant pressure (50 Pa) through one inlet into moving blood inflowing at constant pressure (40 Pa) through two inlets, with a linear solidification model, and zero-pressure at outlet.

Additionally, one patient-specific AVM case (with two feeding arteries and two draining veins) was modeled. The nidus was modeled using porous media, since a realistic geometry extraction was not possible due to the insufficient resolution of 0.6 mm of the 3DRA images.

The extraction of parameters (i.e. porosity and permeability) was again based on pixel intensities from 3DRA images. Boundary conditions for the blood flow were determined from phase contrast magnetic resonance angiography. In particular, a constant 0.15 m/s Onyx velocity in one of the feeding arteries, and a constant 0.065 m/s blood velocity were applied. Figure 1.9 visualizes the progression of Onyx over a time of 0.45 s after the start of Onyx injection, for these simulations.

Their results indicated that blood flow paths are not necessarily predictive for Onyx trajectories (probably because of the different viscosity and solidification process for Onyx), and that the increase in Onyx viscosity occurs gradually from the surface towards the core of the Onyx.

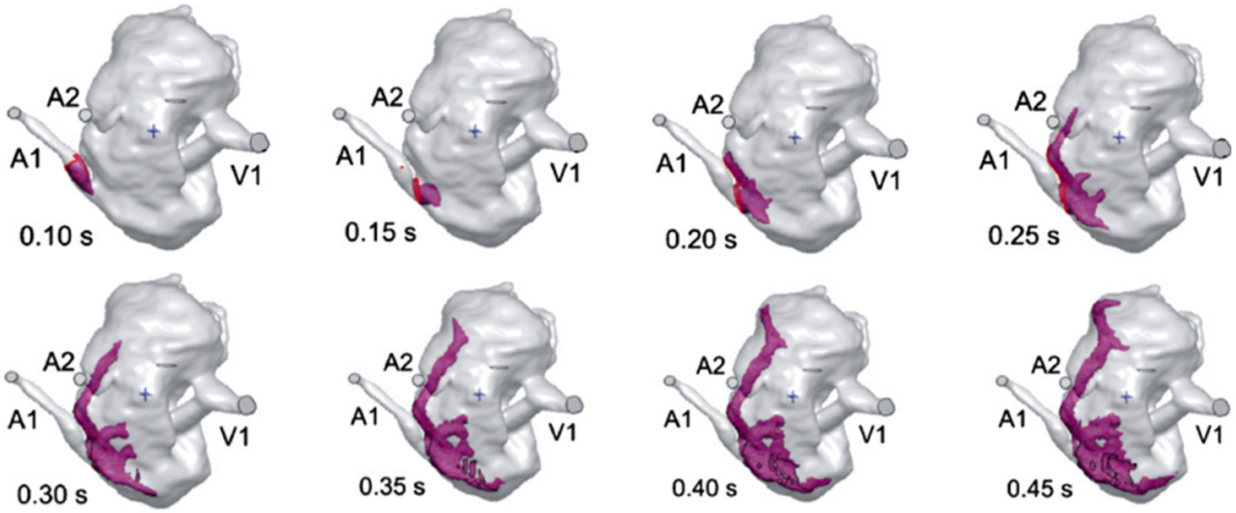

Figure 1.9: Onyx progression over 0.45 s after the start of Onyx injection in the patient-specific AVM modeled by porous media. A1 and A2 indicate the arterial feeders and V1 indicates one of the venous drainers of the AVM (the second venous drainer is not visible in this specific visualization, as it is located at the back of the AVM). The purple zone indicates the cells in which Onyx is present.
(Figure adapted from [7].)

A novel mathematical model for the embolization process was introduced by White et al. (2013), using a two-phase fluid approach to represent the dynamic interactions between blood and an adhesive LEA (glue mixture of 80 % Lipiodol and 20 % N-butyl-2-cyanoacrylate) [107]. This study profiles itself as the first to investigate the complex AVM embolization in two dimensions (2D), but still using simplified, idealized geometries. The goal was to examine the dynamics of injected embolic agents and explore possible blocking strategies, while considering surface tension effects.

In this study, both fluids were considered incompressible and viscous—a reasonable assumption for blood in small vessels, but less realistic for the glue (as glue would actually behave viscoelastically). Also, laminar flow—with fixed Reynolds numbers (Equation 1.9) of 400—and rigid walls with a no-slip condition were assumed, and the glue and blood were assumed to have equal density at the start of the simulation. The glue viscosity was exponentially increased over time to simulate solidification.

Furthermore, the open-source Gerris flow solver (available via `https://sourceforge.net/projects/gfs/files/gfsview/`) was employed to solve the multi-phase system, and the Volume-of-Fluid (VOF, explained in more detail in Section 2.2.1 *Multi-phase flow: Volume-of-Fluid method*) was used as a solution method for modeling blood and embolic agent interactions, with the glue modeled as droplets rather than a continuous stream. The geometry investigated in this study was a simplified 2D representation of mother-daughter branching vessels. Results indicated that glue injection close to the bifurcation of the AVM increases the effectiveness of blockage, especially when the targeted vessel is small relative to its neighboring vessels.

Furthermore, simulations for increasing glue viscosity over time showed that more viscous glue was more effective in larger daughter vessels by slowing down the glue propagation and allowing time for solidification before the glue passed through the vessel (for the smaller daughter vessel this was less important, because of lower flow rates). Finally, surface tension effects were investigated by examining Weber numbers (Equation 1.10) over a range of 100 to 10 000 to assess various surface tension effects. Results suggested that surface tension effects on the glue shape were significant, as especially at lower Weber numbers the droplet shapes remained more realistic. The main limitations of this study are the simplified geometry (no realistic AVM case), the modeling of glue as discrete droplets rather than a continuous stream, and the lack of experimental validation to assess the realism of various simulations.

Reynolds number definition:

$$\mathrm{Re} = \frac{\rho \cdot v \cdot L}{\mu} \tag{1.9}$$

With ρ fluid density [kg/m^3], v characteristic velocity [m/s], L characteristic length [m], and μ dynamic viscosity [Pa $\cdot$ s].

Weber number definition:

$$\mathrm{We} = \frac{\rho v^2 L}{\sigma} \tag{1.10}$$

With ρ fluid density [kg/m^3], v characteristic velocity [m/s], L characteristic length [m], and σ surface tension [N/m].

Lastly, Zhang et al. (2023) developed computational models for two patient-specific AVM cases to simulate Onyx embolization processes through different feeding arteries [8]. Porous media models were employed to simplify the complex nidus geometry, as the imaging resolution of 0.5 mm did not allow for realistic geometry extraction of the nidus. The parameters for the porous media (i.e. porosity and permeability) were derived based on the work of Orlowski et al. (2011), and patient-specific DSA and either magnetic resonance angiography or CTA imaging data were provided.

The mixture model was used as the multi-phase flow model to simulate the interactions between blood and LEAs (Onyx-18 and Onyx-34). In this study, laminar flow, blood as incompressible Newtonian fluid, rigid walls, velocity inlet boundary conditions, and pressure differences of 10 mmHg over the AVMs were assumed. The diffusion process of the DMSO solvent was calculated by solving the species transport equation, and the coagulation process was modeled by establishing a relationship between the viscosity of Onyx and the corresponding concentration of EVOH. The relationship between Onyx viscosity and EVOH concentration was assumed to be exponential and was obtained by curve fitting to experimental data [122]. The coagulation process was simulated for 5 minutes, and complete solidification was assumed to occur at 0.4 Pa.s (= 400 cP). For both AVM cases, multiple Onyx injections were simulated until the flow in the feeding artery was reduced to 5 % of its preinterventional flow rate. So, the focus was on determining the flow rate changes after injections to assess the degree of embolization, assuming that a 95 % decrease in preinterventional arterial feeder flow rate indicates sufficient embolization. The total amount of Onyx injected during the embolization procedure for a specific patient was known, yet the amount of Onyx used in batches was unknown. Thus, the number of injections and amount of Onyx per injection did not exactly match the real situation, but were still realistic, and the results could provide useful insights.

Figure 1.10 shows some results of various simulated embolization treatments in this study, illustrating the injection progress and solidification progress of trans-arterial embolization in two patient-specific AVMs. Overall, the simulations successfully reproduced the flow trajec-

tories and coagulation sites of the embolic agents within the nidus, showing good correspondence with clinical DSA and CTA imaging data from the patients. A noteworthy limitation of this work is the use of non-patient-specific velocity and pressure boundary conditions.

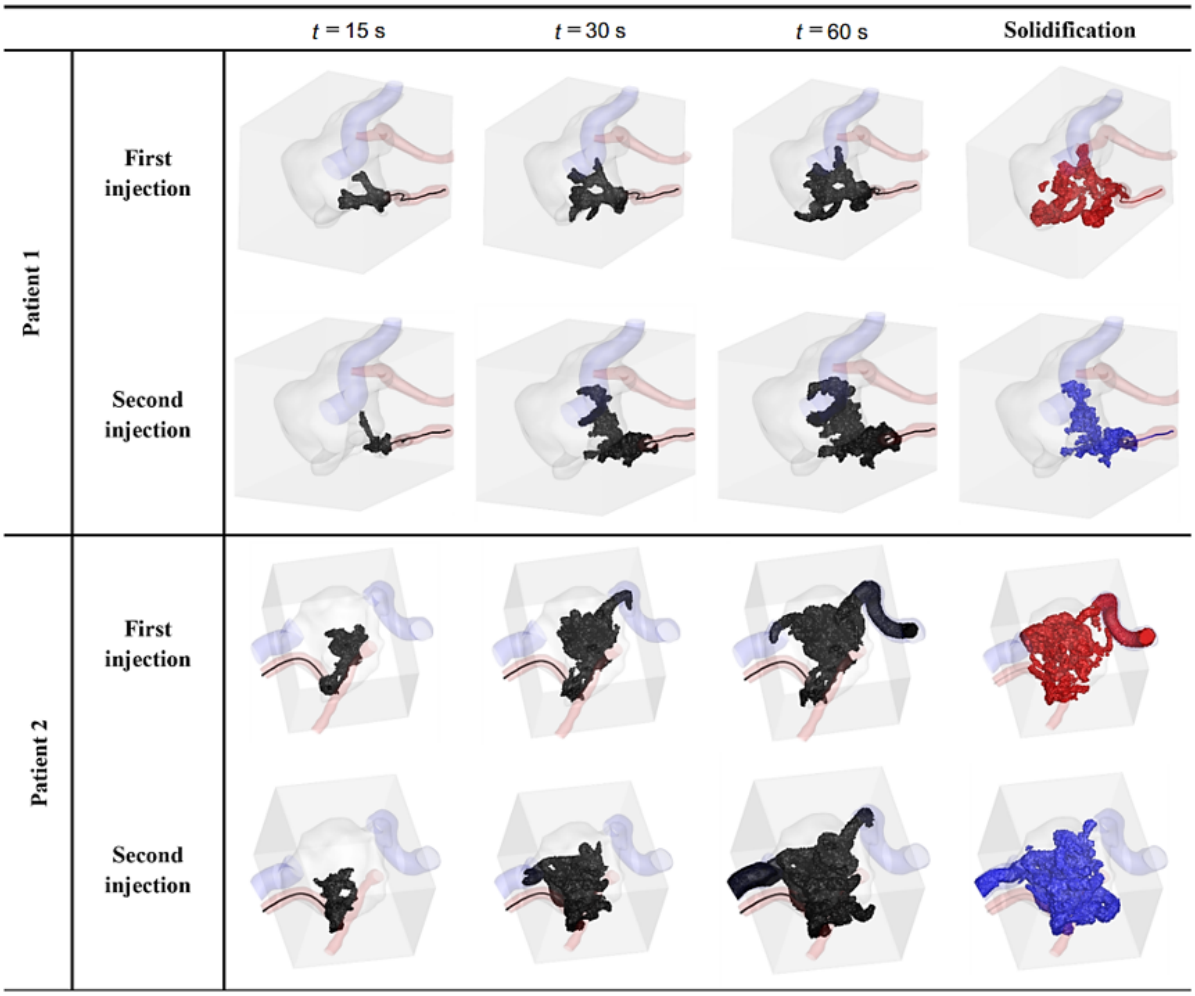

Figure 1.10: Schematic of the injection progress and solidification progress of trans-arterial embolization from a certain feeding artery for patient 1 and patient 2. Two steps of injections of liquid embolic agents were simulated. The three columns left show 3D rendering (black) for volume fractions from 3 to 6 % of EVOH after the first injection and second injection at t = 15 s, 30 s, and 60 s for both patients. The last column shows 3D rendering for EVOH viscosity above 400 cP after the solidification of the first injection (red) and second injection (blue) for both patients.
(Figure from [8].)

1.2.3 Added Value of Computational Modeling

1.2.3.1 Importance of Personalized Medicine

Personalized medicine plays an important role in improving AVM treatments. As the AVM characteristics (e.g. size, location, etc.) are patient-specific by nature, using generalized protocols may lead to suboptimal treatment outcomes. By opting for a more personalized approach, treatment protocols can be tailored to the patient, considering the patient-specific vasculature, hemodynamics, and certain critical points sensitive to high stresses or rupture. Incorporation of patient-specific information enables clinicians to better anticipate potential complications and make more informed decisions, thereby improving the likelihood of a successful treatment outcome [123].

1.2.3.2 Relevant Outcomes of Computational AVM Models

Outcomes from CFD modeling of the cerebral blood flow (and embolic agent behavior) in patient-specific AVMs that are of interest include blood flow patterns, flow distributions, pressures, and shear stresses.

Typically, the clinician assesses the success of an embolization procedure by observing the flow of the contrast agent in the draining vein, since there is no more risk for hemorrhage when there is no longer blood flow through the AVM [8, 106, 107]. So, one of the major parameters of interest is the change in flow rates in the relevant vessels (e.g. feeding arteries and draining veins) after embolization, as this is an indicator of the degree of embolization. Typically, a flow rate reduction to 5 % or less of the preinterventional flow rate through the feeding artery is considered sufficient for successful treatment [8, 107].

Further, pressure gradients over the AVM can also be investigated. AVMs are low-resistance, high-flow shunts with abnormal hemodynamics [10, 11, 58]. In healthy situations, the pressure drop over the capillaries is around 70 mmHg [124]; but the pressure drop over AVMs is generally smaller (for example, around 10 mmHg [58], but depending on the case), causing venous hypertension [10,11,58]. The magnitude of the pressure drop can be indicative of the severity of the AVM case. Furthermore, when modeling AVM occlusion due to embolic agent solidification, the pressure drop could increase during the solidification process, as the resistance would increase and the flow would decrease [55–57].

Additionally, WSS is an interesting parameter to investigate, as both excessively high and low shear stresses can lead to serious complications [125]. When shear stresses exceed a certain upper limit (around 70 to 100 Pa), there is a risk for platelet activation and thrombus

formation following the coagulation cascade [125]. Conversely, extremely low shear stresses (around -0.4 to 0.4 Pa) may lead to atherosclerosis (i.e. hardening of vessel walls due to plaque build-up) or stasis, which can also lead to clotting and thrombus formation [125]. However, WSS is generally overestimated with CFD due to the assumption of rigid and stationary walls; therefore it is important to note that fluid-structure interaction (FSI, i.e. study of how fluid flow and solid structures influence each other, considering deformation of the wall due to forces exerted on it) would be necessary to get an accurate representation of the WSS distributions, but was out of the scope of this thesis [126, 127]. CFD simulations can be used to model embolization treatments and assess certain intervention-related risks, including insufficient embolization, reduced perfusion of healthy brain tissues, embolic agent leakage into draining veins, or harmful pressure or shear stress increases [7, 123].

1.2.3.3 Long-term Goal

In the long term, patient-specific simulations using computational modeling could enable clinicians to optimize treatments preoperatively. Simulations could facilitate virtual testing of different treatment scenarios and optimize, for instance, the catheter pathway, catheter type, type of embolic agents, injection location, injection rate, and tailor the overall embolization protocol to anticipate potential complications. The simulations could provide the clinician insight into the degree of embolization and the ability to assess risks such as reduced perfusion of healthy brain parenchyma, leakage of embolic agents, or dangerous pressure increases or shear stresses in the vessels [7]. The availability of such simulations can enhance the clinician's understanding of various treatment options and increase confidence in the selected treatment plan. Furthermore, CFD simulations, when well visualized, can serve as a valuable tool for patient education, helping patients understand their condition and potential interventions. By providing a clear, visual representation of blood flow dynamics and treatment outcomes, communication between clinicians and patients and informed decision-making can be enhanced.

However, there are still significant challenges to overcome before such computational modeling can be integrated into routine clinical practice, as detailed further in the following Section 1.2.3.4 *Current Bottlenecks*. Investigation of a larger number of AVM cases is essential to validate the reliability and effectiveness of these simulations in clinical settings. Additionally, improved and faster strategies for segmentation would be needed to make CFD modeling of AVMs standard practice. It is important to note that this thesis represents only a very small initial step towards achieving the long-term goal, with the specific objective of

this thesis further detailed in Section 1.2.4 *Goal of the Thesis*.

1.2.3.4 Current Bottlenecks

Although CFD modeling of AVMs offers significant potential advantages, it has yet to be integrated into routine clinical practice, as there are still several major challenges to be addressed.

Patient-specific AVM modeling remains challenging due to intricate geometries, although advances in imaging, particularly DSA, enable more accurate segmentations [8,123]. Further, simulating embolization procedures is challenging, as it requires multi-phase modeling to account for blood and embolic agent interactions, and modeling of embolic agent solidification [7, 8, 107, 120]. Additionally, simulations rely on certain assumptions for simplification (e.g. Newtonian behavior of blood, flow or pressure boundary conditions, and rigid vessel wall assumptions) [7, 8, 107, 120]. Improved, faster, and more standardized modeling methods are crucial for integrating computational AVM modeling into routine clinical practice [123]. Moreover, medical imaging data could provide valuable input for simulations, e.g. patient-specific blood velocities or flow distributions over the draining veins from DSA data [7,8,120, 123].

Another obstacle is the lack of clinical validation of computational models. Currently, there are no standard modeling approaches, no agreed boundary conditions or input parameters, and no established validation metrics, which of course limits the confidence of clinicians in these models for decision-making [8,123]. Larger clinical datasets with validation through retrospective studies could foster greater trust in these models [8,123].

Furthermore, the process of segmenting patient-specific AVMs and simulating embolization procedures remains computationally intensive. While most embolization procedures are preplanned, making this a less critical issue, faster simulations are key for future clinical use. In the long term, artificial intelligence (AI) is promising to speed up the segmentation, model generation, and CFD simulations. Additionally, segmentations that are currently generated during interventions in the hospital could be of high value.

Lastly, enhanced collaboration between clinicians and engineers is essential to overcome the current bottlenecks and develop validated, interpretable, and clinically useful computational models, to pave the way for the integration of patient-specific computational models into the clinical pretreatment planning routine.

1.2.4 Goal of the Thesis

This thesis is situated in the bigger context of an FWO (Fonds Wetenschappelijk Onderzoek) project concerning "Patient-specific planning of minimally invasive interventions in the brain based on mapping of the vasculature and hemodynamics". The overall goal of this project is the search for novel methodologies for pretreatment embolization planning and catheter navigation based on vascular mapping and cerebral blood flow modeling. This goal is separated into two objectives, being 1) cerebral vascular mapping based on 3D angiography data to quantify vascular accessibility for catheter navigation and support of catheter tracking, and 2) cerebral blood flow modeling using CFD and, potentially, AI to support pretreatment planning. This thesis is situated within the second objective concerning CFD modeling.

The workflow for cerebral blood flow modeling would generally consist of the following steps:

- High-quality mesh generation
- Baseline CFD modeling approach
- Modeling of embolization scenarios for pretreatment planning
- Validation using a cerebrovascular phantom

This thesis is focuses on CFD-based cerebral blood flow modeling of a patient-specific case, based on patient-specific imaging data. The central research question is how the Onyx injection rate influences the hemodynamic environment during embolization. Specifically, the study examines Onyx progression, its distribution over downstream branches, and resulting local pressure differences. To this end, three injection rates—0.08, 0.16, and 0.32 ml/min—are simulated in a patient-specific AVM model.

Currently, injection of Onyx during embolization procedures is performed manually by clinicians with a syringe, without a predetermined injection velocity. As a result, the exact injection velocity is not precisely known. We hypothesize that this velocity of injection will likely affect the distribution of Onyx and, consequently, the outcome of the embolization procedure. Therefore, investigating the effects of modifying this parameter could provide valuable insights. In the clinic, Onyx injection velocities could potentially be controlled using syringe pumps [128].

1.2.4.1 Case Description

The patient-specific AVM selected for this study was identified in a patient presenting with severe and recurrent headaches. The AVM was nodular (i.e. rounded, lump-like shape), measuring approximately 1.5 to 2 cm in size, and located in the occipital-parietal region near

the cortex in the left hemisphere. Following the SM grading system, the AVM was classified as a grade III by interventional radiologists, rendering it a suitable case for endovascular embolization treatment. Figure 1.11 shows the AVM under investigation for this thesis on a sagittal angiography image and a coronal DSA image. The arterial feeders are (i) the pericallosal artery, a branch of the left anterior cerebral artery (ACA), and (ii) a branch of the left middle cerebral artery (MCA). Venous drainage occurred mainly through (iii) a cortical vein towards the superior sagittal sinus, with (iv) additional deep venous drainage towards the great cerebral vein.

The treatment process consisted of a single embolization procedure following the transarterial route, resulting in complete occlusion of the nidus. During the procedure, two Apollo microcatheters with a 15 mm detachable tip (as depicted in Figure 1.8) were guided to the nidus through both arterial feeders. Onyx-18 was injected in eight different injection steps, with a total amount of 1.63 cc (or ml) Onyx-18 delivered over 46 minutes.

Imaging data was obtained in multiple stages to guide and evaluate treatment. Pretreatment imaging included CT and MRI scans to evaluate the AVM's structure and surrounding anatomy. During embolization, a superselective angiography was performed to guide catheterization and track Onyx progression. Posttreatment, an angiography confirmed full AVM occlusion, and a follow-up MRI performed six months after the procedure confirmed the durability of the treatment outcome.

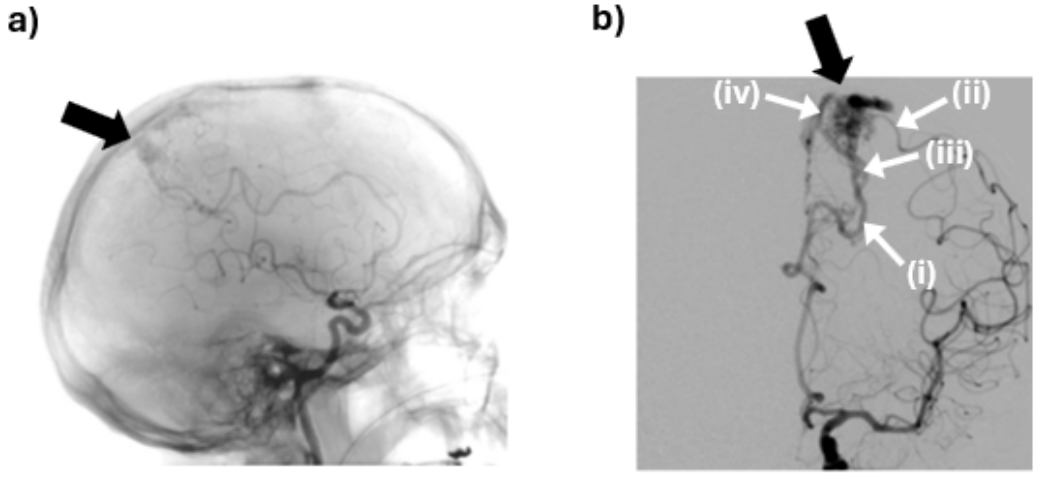

Figure 1.11: The patient-specific AVM under investigation for this thesis. **a)** Sagittal angiography image with black arrow indicating the nidus. **b)** Coronal DSA image with black arrow indicating the nidus and white arrows indicating the feeding arteries and draining veins: (i) feeding pericallosal artery, branch of the left ACA, (ii) feeding branch of the left MCA, (iii) deep venous drainage towards the great cerebral vein, and (iv) superficial venous drainage via a cortical vein towards the superior sagittal sinus.

Chapter 2

Methods

2.1 Mesh Generation

This section outlines the general workflow for segmentation and mesh generation based on provided medical images. The segmentation and meshing processes utilized software from Mimics and 3-Matic (Materialise NV, Leuven, Belgium), Fluent Meshing (ANSYS Inc., Canonsburg, PA, USA), and ANSYS Discovery 2024 (ANSYS Inc., Canonsburg, PA, USA). Additional details on the employed tools and settings in these programs can be found in Appendix A: *Additional Information on Tools and Settings in Mimics, 3-Matic, ANSYS Discovery, and Fluent Meshing.*

2.1.1 Data Acquisition

Accurate computational models rely on high-quality imaging data, as segmentation and meshing quality directly impact model reliability. Precise delineation of the vasculature ensures the model accurately reflects the AVM's geometry, essential for realistic simulations. 3DRA images were utilized for segmentation due to their superior spatial resolution (here 0.44 mm).

For the AVM under investigation, the provided 3DRA imaging dataset consisted of 253 slices with a slice thickness of 0.44 mm. The images were acquired with dimensions of 256 $\times$ 256 pixels, covering a field of view of 111 $\times$ 111 mm. A representative slice, shown in Figure 2.1, clearly illustrates the contrast between the vascular structures (white, due to contrast agent) and the surrounding tissues (black), facilitating detailed delineation of the vasculature.

The resolution of 0.44 mm of the patient's medical images allowed extraction of feeding arteries, draining veins, and an approximate representation of the nidus morphology,

but failed to capture finer details of small nidal vessels (as these vessel diameters were too small compared to the resolution). For this resolution, porous media might be suitable to approximate flow distributions in the nidus, but this was beyond the scope of this thesis.

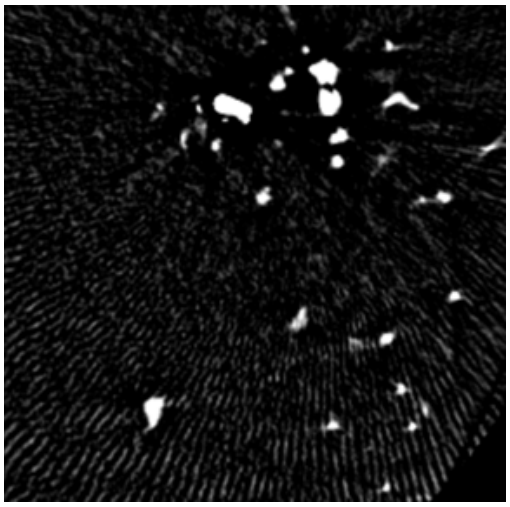

Figure 2.1: One slice of the 3DRA imaging dataset with 256 × 256 pixels and slice thickness of 0.44 mm. The vasculature is visualized in white, while the surrounding tissue is visualized in black.

2.1.2 Geometry Segmentation

Segmentation was performed using Mimics and 3-Matic. An initial threshold-based segmentation (selecting gray values from 1250 to 14084) was generated from 3DRA images (Figure 2.2), from which only the most relevant vasculature—nidus, feeding arteries, and draining veins—was retained to minimize computational costs. Relevant vessels were identified using angiography and DSA data, and manually segmented using various tools in Mimics. Manual corrections were performed to preserve fine vessels and very close-passing vessels.

The resulting 3D model was smoothed to reduce surface irregularities and segmentation artifacts, improving anatomical representation and mesh quality for simulations (Figure 2.3.a). Next, the inlets of the feeding arteries and outlets of the draining veins were cut perpendicular to the flow direction (Figure 2.3.b). Then, both outlets were extruded in 3-Matic over a length equal to five times their circular equivalent diameter (Figure 2.3.c). The rule of thumb in computational modeling is to extrude outlets over a length of around five times their diameter to allow flow profiles to fully establish (i.e. when velocity profiles no longer change in the axial direction; for laminar flow this profile is parabolic) [129, 130]. Otherwise, non-physiological results for pressures, velocities, etc. would be observed near

those boundaries.

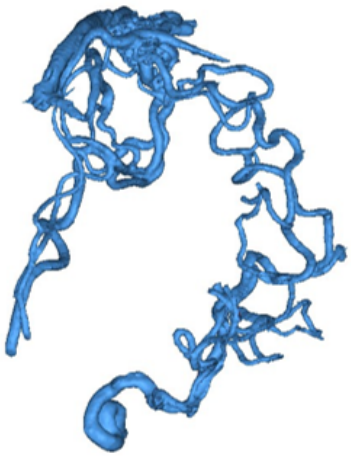

Figure 2.2: Initial threshold-based segmentation of the vasculature after using the 'Threshold' tool with a range of gray values from 1250 to 14084 on the provided 3DRA images of the patient.

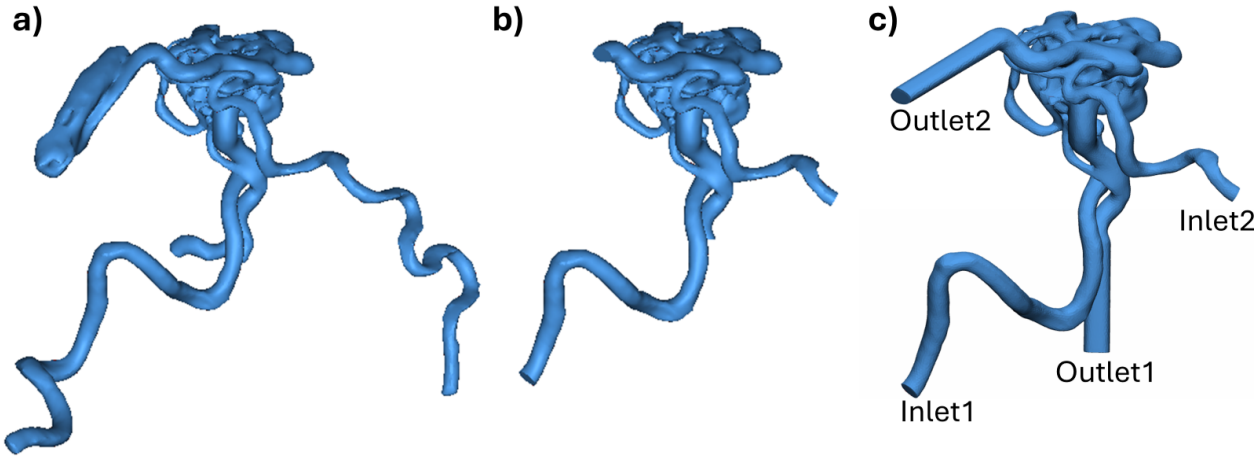

Figure 2.3: **a)** Segmentation after removing vessels that are not of interest and smoothing. **b)** Segmentation after cutting in- and outlets. **c)** Segmentation after extruding the outlets. Outlet 1 (circular equivalent diameter of 2.99 mm) was extruded 14.95 mm, and outlet 2 (circular equivalent diameter of 3.31 mm) was extruded 16.55 mm. Inlet 1 corresponds to the feeder from the left ACA, inlet 2 to the feeder from the left MCA, outlet 1 to the deep draining vein towards the great cerebral vein, and outlet 2 to the superficial cortical draining vein.

2.1.3 Mesh Generation

The meshing process was carried out using 3-Matic and Fluent Meshing. An adaptive remesh ensured a minimal element skewness measure of 0.4, while a uniform remesh standardized triangle shapes and sizes across the mesh for improved quality. Diagnostic options in the 'Fix Wizard' panel were updated as needed, resulting in a high-quality mesh, where one shell existed (Figure 2.4). The final mesh after optimization in 3-Matic is depicted in Figure 2.5.

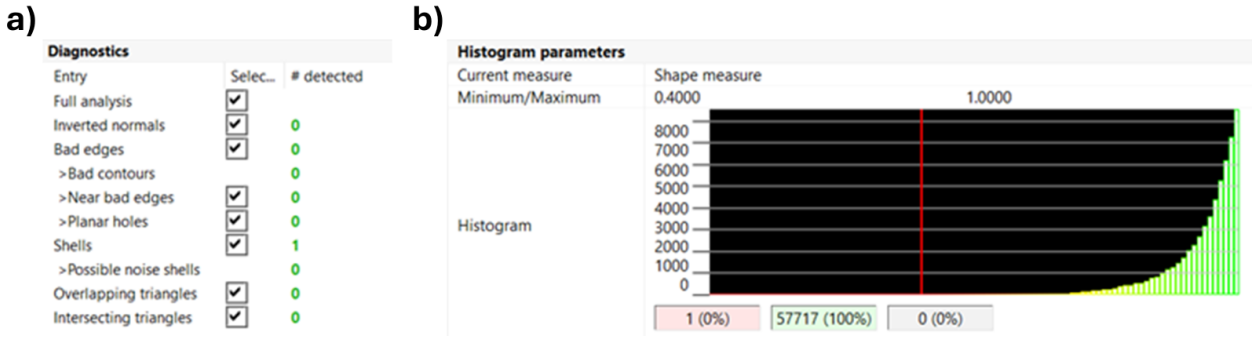

Figure 2.4: **a)** 'Fix Wizard' panel for the final mesh in 3-Matic after the diagnostic options were reviewed and updated as needed. **b)** 'Histogram parameters' for the final mesh in 3-Matic, with the shape measure being 'Skewness'.

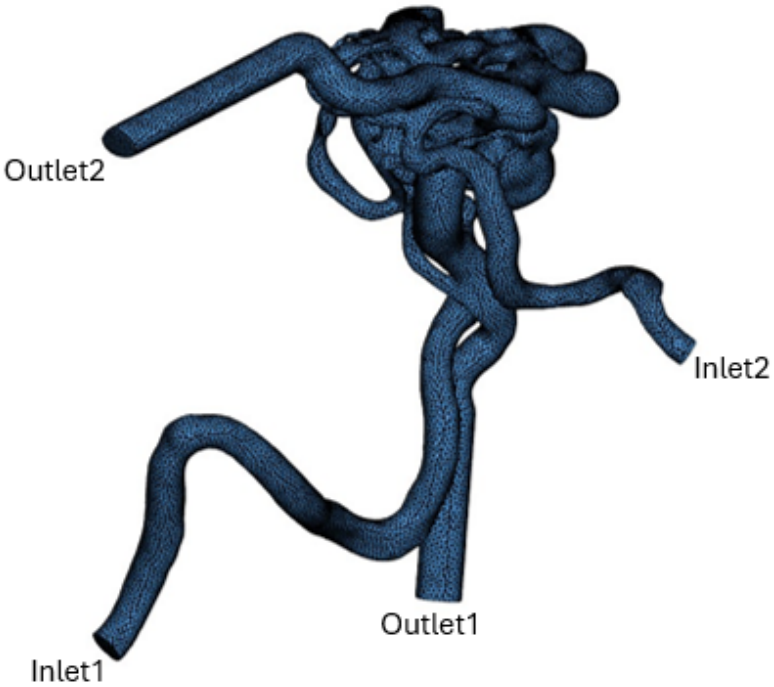

Figure 2.5: The final mesh after optimization in 3-Matic. The inlets and outlets are indicated.

Further meshing was performed in Fluent Meshing using the 'Fault tolerant meshing' workflow (due to its robustness to imperfections in complex geometries) [131]. While standard workflow steps were followed, key settings are outlined in this paragraph. Local surface mesh refinements were applied to preserve small vessels and catheter geometry. The fluid region was filled with tetrahedral volume elements, chosen for their ability to accurately capture complex geometries [132]. The boundary conditions were updated to 'Velocity-inlet' and 'Pressure-outlet'. Finally, a volume mesh was created with three boundary layers (with the aspect-ratio offset type and growth rate of 1.2) to capture high gradients of physical properties (e.g. velocity) near the walls, ensuring finer sampling in the direction perpendicular to the wall while balancing computational efficiency and accuracy [133,134]. Section 2.1.5 *Mesh Sensitivity Analysis* evaluates different mesh densities to determine optimal settings for refinements and mesh parameters (listed in Table 2.2).

2.1.4 Introducing Catheters into the Model

To prepare the mesh for multi-phase simulations, catheters were added using ANSYS Discovery 2024. In each arterial feeder, a catheter was inserted (as was the case during the actual procedure, determined by visual inspection of the 2D DSA images) and aligned with the centerlines of flow in the feeders. Their diameter was set to 0.3302 mm (remark that ideally also a thickness would be assigned to the catheter), matching the inner diameter of the Apollo microcatheter [117], and the catheter tip locations were estimated from angiography images (Figure 2.6). Onyx flow through the catheters will not be explicitly modeled, but the end of catheter 1 will serve as the Onyx inlet, whereas the end of catheter 2 will be part of the wall of the model, to focus on injection from one catheter at a time, as would be the case in reality. Figure 2.7 displays the final model. A more detailed workflow can be found in Appendix B: *Workflow for Implementation of Catheters in ANSYS Discovery.*

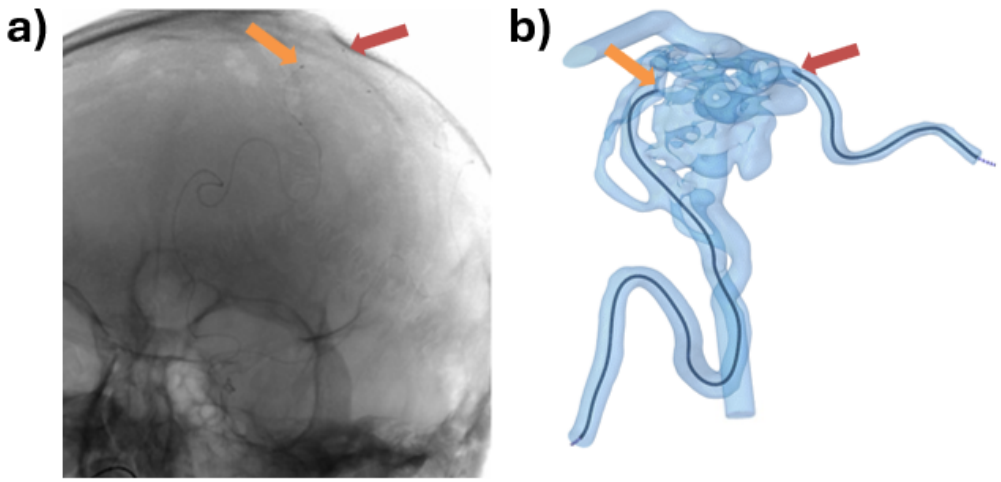

Figure 2.6: **a)** An angiography image during embolization showing black dots corresponding to the locations of the beginnings and ends of the 15 mm detachable tips of the Apollo microcatheters. **b)** Model in ANSYS Discovery with catheters. The tip of the catheter in blood inlet 1, or the arterial feeder from the ACA, is indicated by the orange arrow; and the tip of the catheter in blood inlet 2, or the arterial feeder from the MCA, is indicated by the red arrow.

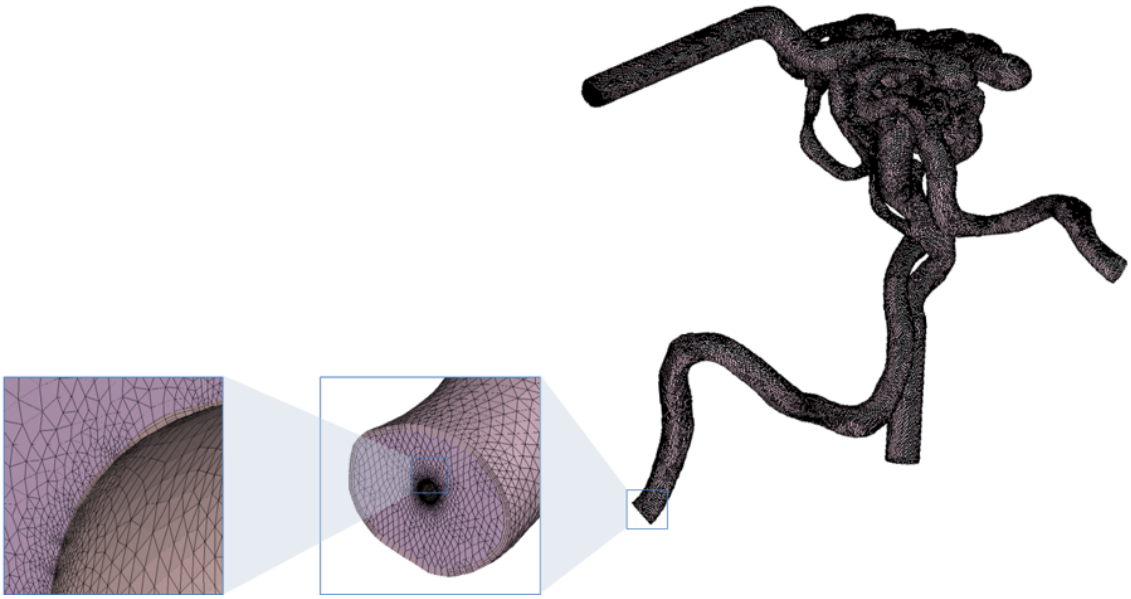

Figure 2.7: The final mesh from Fluent Meshing for the AVM geometry with the implemented catheters. The three boundary layers and mesh refinement around the catheters are apparent on the zoomed-in panels.

2.1.5 Mesh Sensitivity Analysis

In numerical simulations, accuracy depends on domain discretization, i.e. the mesh. Finer meshes improve accuracy at the cost of increased computational expense, while coarser meshes may lead to results that are strongly dependent on the chosen discretization. This section presents a mesh sensitivity analysis (MSA) to identify a mesh that balances accuracy and efficiency. For this study, the optimal mesh is defined as the one where all parameters of interest differ less than 5 % from those of the finest mesh (Equation 2.1), as this allows for a solution that is not overly dependent on mesh refinement while also ensuring practical efficiency in terms of computational time and resources.

Formula for percentual differences:

$$\mathrm{PD}_{\text{current mesh}}[\%] = \frac{\mathrm{Parameter}_{\text{current mesh}} - \mathrm{Parameter}_{\text{finest mesh}}}{|\mathrm{Parameter}_{\text{finest mesh}}|} \cdot 100\% \tag{2.1}$$

With $\mathrm{PD}_{\text{current mesh}}$ the percentual difference w.r.t. the finest mesh [%], and *Parameter* a certain parameter of interest (e.g. velocity, pressure, etc.) in the appropriate units.

As explained later in Section 2.2.3 *Boundary Conditions*, flow distributions across the two outlets were derived from DSA images, but the VOF model used for the multi-phase flow is not compatible with outflow boundary conditions (see Section 2.2.1 *Multi-phase flow: Volume-of-Fluid method*). Therefore, an initial single-phase simulation with outflow boundary conditions was performed to determine appropriate pressure outlet boundary conditions for the multi-phase case. For both of these models, a MSA was conducted (with steady-state simulations for the single-phase case and transient with constant values for the multi-phase case).

2.1.5.1 Mesh Sensitivity Analysis for Single-phase Case

Mesh refinements from around 1 to 11 million elements were considered (Table 2.1). A refinement factor of at least 8 was ensured so the mesh was approximately refined by a factor of 2 in each spatial direction in 3D (thus $2^3 \cdot$ number of elements in coarsest mesh $<$ number of elements in densest mesh). For this case, the facet-averaged local static pressures at both inlets and both outlets planes were the parameters of interest, for which Figure 2.8 shows the percentual differences (Equation 2.1). From this analysis, the mesh with 9 254 473 elements was considered optimal.

Table 2.1: Mesh parameters and cell counts of meshes for the single-phase flow case. (Curvature 1 refers to the outer surface of the model, curvature 2 refers to the in- and outlets, and curvature 3 refers to the catheters.)

Mesh	Curvature 1		Curvature 2		Curvature 3		Max cell length [mm]	Number of cells
	Min [mm]	Max [mm]	Min [mm]	Max [mm]	Min [mm]	Max [mm]		
1	0.2	3	0.1	2	0.2	1	1	1 107 326
2	0.16	2.6	0.07	1.8	0.06	0.8	0.7	3 056 111
3	0.013	0.505	0.006	0.205	0.0045	0.045	0.55	5 007 510
4	0.007	0.308	0.003	0.169	0.002	0.0345	0.45	7 125 615
5	0.0054	0.27	0.0019	0.145	0.0011	0.029	0.255	9 254 473
6	0.005	0.25	0.0015	0.13	0.001	0.025	0.25	11 509 043

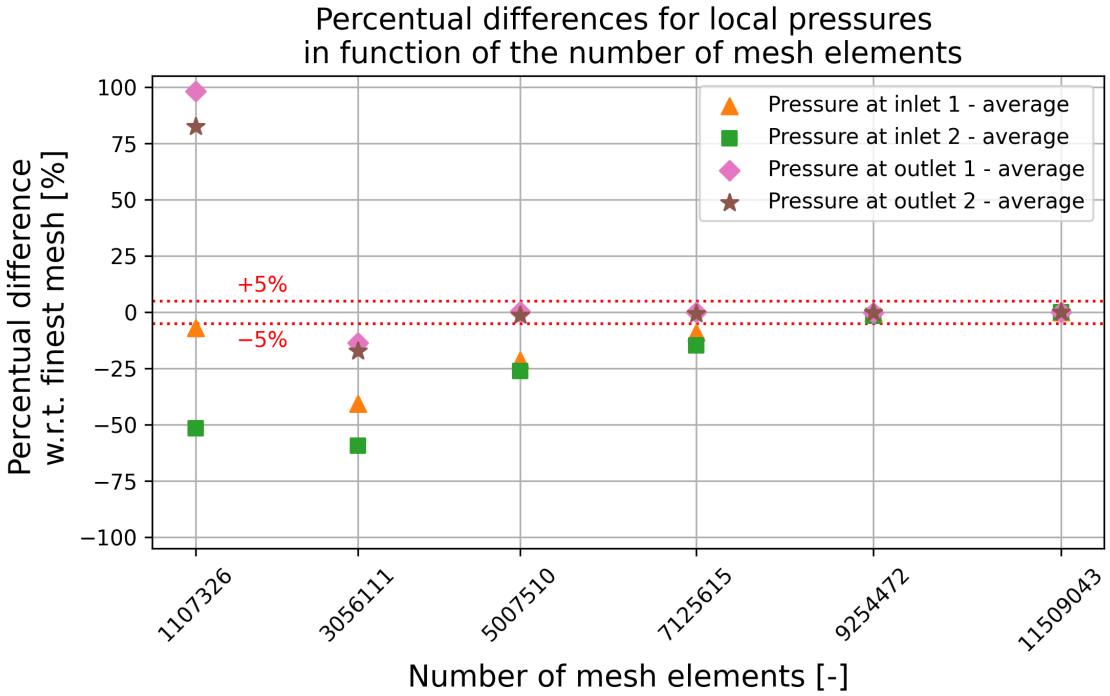

Figure 2.8: Percentual differences for local facet-averaged static pressures at in- and outlets for each mesh compared with the finest mesh in function of the number of mesh elements. The red dotted lines indicate +5 and -5 %.

2.1.5.2 Mesh Sensitivity Analysis for Multi-phase Case

For the final model (AVM with catheters), mesh densities were investigated from around 1 to 13 million elements (Table 2.2). Figures 2.9, 2.10, 2.11, and 2.12 show the percentual differences for various parameters of interest, i.e. global and local velocities, global and local static pressures, and global and local blood and Onyx phase volume fractions. For

all parameters of interest, averages and 95th percentiles were assessed. The results suggest the mesh with 11 510 615 elements as the optimal choice, which will be used for all further multi-phase flow simulations.

Table 2.2: Mesh parameters and cell counts of meshes for the multi-phase flow case. (Curvature 1 refers to the outer surface of the model, curvature 2 refers to the in- and outlets, and curvature 3 refers to the catheters.)

Mesh	Curvature 1		Curvature 2		Curvature 3		Max cell length [mm]	Number of cells
	Min [mm]	Max [mm]	Min [mm]	Max [mm]	Min [mm]	Max [mm]		
1	0.18	3	0.1	2	0.172	0.9	1	1 286 791
2	0.16	2.6	0.07	1.8	0.06	0.8	0.7	3 055 725
3	0.013	0.505	0.006	0.205	0.0045	0.045	0.55	5 005 853
4	0.007	0.308	0.003	0.169	0.002	0.0345	0.45	7 123 865
5	0.0054	0.27	0.0019	0.145	0.0011	0.029	0.255	9 258 898
6	0.005	0.25	0.0015	0.13	0.001	0.025	0.25	11 510 615
7	0.0049	0.23	0.0014	0.12	0.0009	0.023	0.23	13 289 819

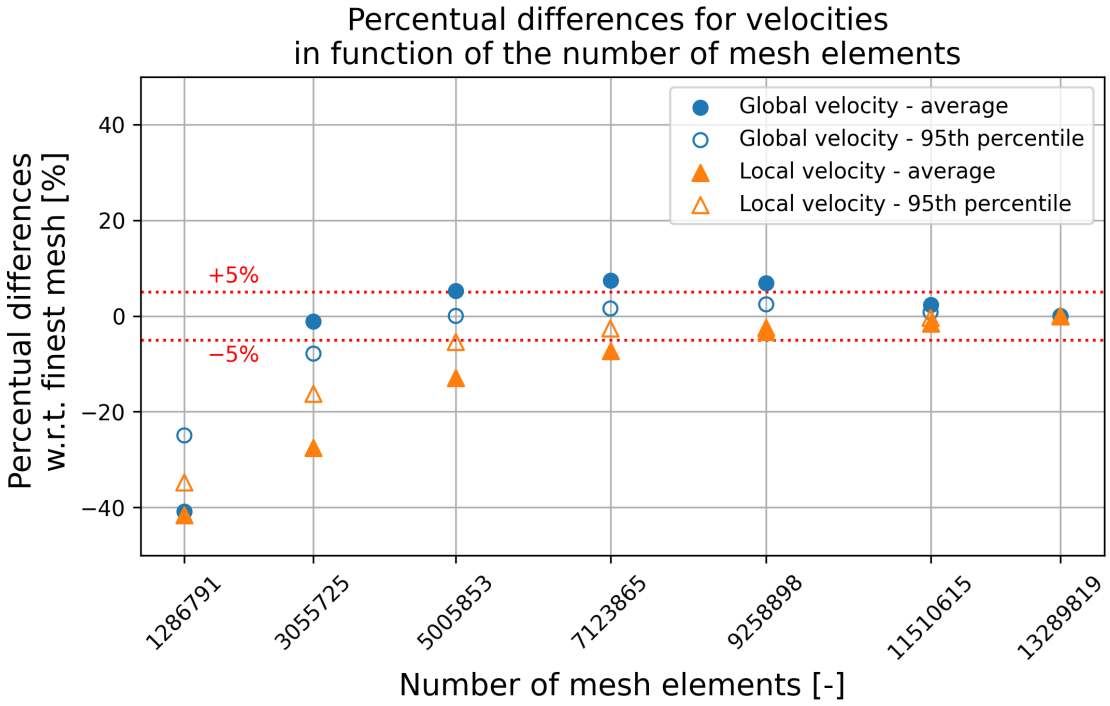

Figure 2.9: Percentual differences for averages and 95th percentiles of global and local (in plane approximately through the middle of the nidus) velocities for each mesh compared with the finest mesh in function of the number of mesh elements. The red dotted lines indicate +5 and -5 %.

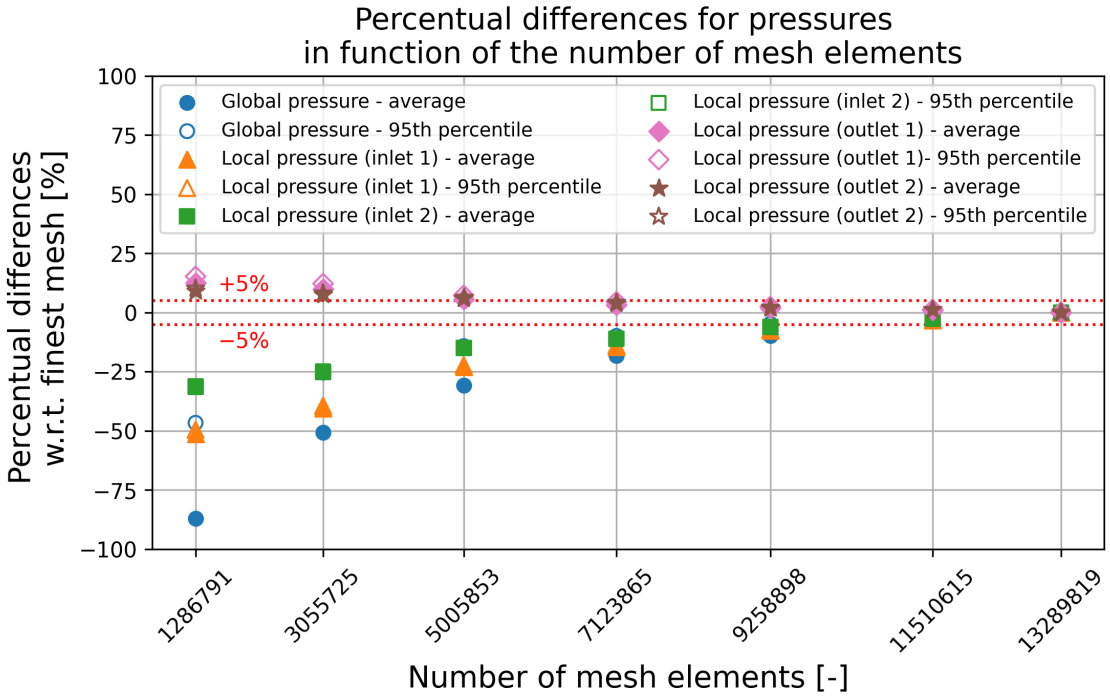

Figure 2.10: Percentual differences for averages and 95th percentiles of global and local (in planes in each of the in- and outlet vessels positioned close to the nidus) pressures for each mesh compared with the finest mesh in function of the number of mesh elements. The red dotted lines indicate +5 and -5 %.

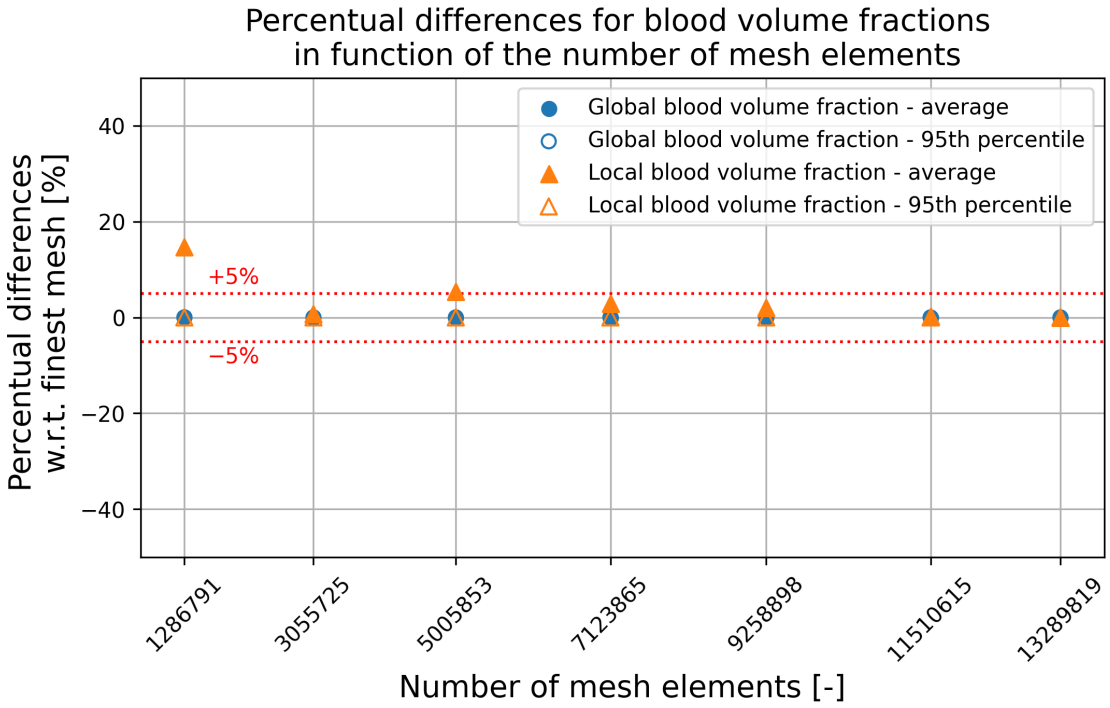

Figure 2.11: Percentual differences for averages and 95th percentiles of global and local (in plane after the Onyx inlet from catheter 1) volume fractions of the blood phase for each mesh compared with the finest mesh in function of the number of mesh elements. The red dotted lines indicate +5 and -5 %.

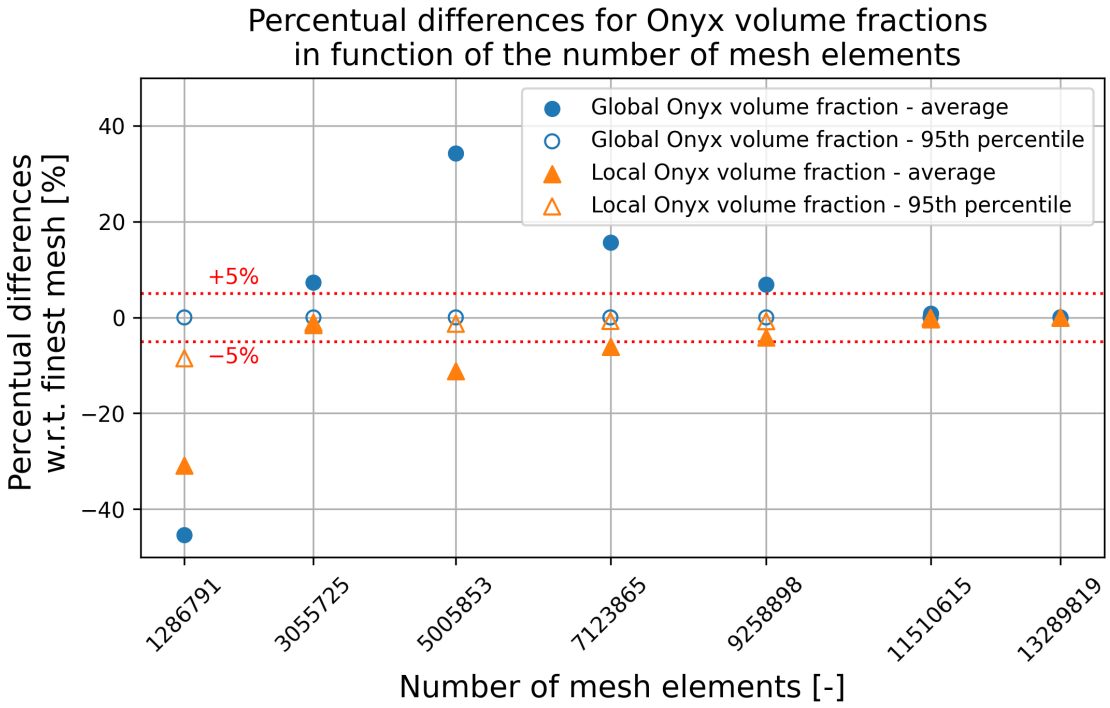

Figure 2.12: Percentual differences for averages and 95th percentiles of global and local (in plane after the Onyx inlet from catheter 1) volume fractions of the Onyx phase for each mesh compared with the finest mesh in function of the number of mesh elements. The red dotted lines indicate +5 and -5 %.

2.2 Computer Simulations

2.2.1 Multi-phase flow: Volume-of-Fluid method

When modeling Onyx flow into the bloodstream (a liquid-liquid multi-phase scenario), a multi-phase model is required to consider the interaction of these immiscible fluids [8, 107, 123, 135]. Specifically, the VOF model, with blood as the primary and Onyx as the secondary phase, was selected to model these two immiscible fluids by solving a single set of momentum equations while tracking the volume fraction of each fluid throughout the domain [135]. This model tracks the free surface of the secondary phase (with the possibility for sharp interfacing) and not just the phases, so that each cell along the blood-Onyx interface has a blood volume fraction between 0 and 1 [135]. In ANSYS Fluent, the Eulerian and Mixture models are also available; however, these are more used for miscible flows without a sharp interface and are therefore less suitable for capturing the immiscible behavior of Onyx in blood [135].

Conservation of mass: By solving the continuity equation for the volume fraction of the Onyx and blood phases, the blood-Onyx interface can be tracked. Equation 2.2 shows the continuity equation for the Onyx phase (secondary phase) [135].

$$\frac{1}{\rho_o}\left[\frac{\partial}{\partial t}\left(\alpha_o \rho_o\right) + \nabla \cdot \left(\alpha_o \rho_o \bar{v}_o\right)\right] = S_{\alpha_o} + \sum_{b=1}^{n}\left(\dot{m}_{bo} - \dot{m}_{ob}\right) \tag{2.2}$$

With ρ_o density of Onyx [kg/m^3], $\bar{v}_o$ velocity vector [m/s], $\dot{m}_{ob}$ mass transfer from Onyx phase to blood phase [kg/s], $\dot{m}_{bo}$ mass transfer from blood phase to Onyx phase [kg/s], S_{α_o} a source term which is taken to be zero, and α_o volume fraction of Onyx phase in a cell [-].

Condition for volume fractions: The blood phase (primary phase) volume fraction will then be computed based on Equation 2.3 [135].

$$\sum_{k=b,o} \alpha_k = 1 \tag{2.3}$$

With α_k the volume fraction of phase k in a cell [-] (with $k = b$ for blood or o for Onyx).

Conservation of momentum: One momentum equation (Equation 2.4 [135])—dependent on volume fractions of both phases through the material parameters—is solved throughout the domain, and the velocity determined from this is shared between the phases.

$$\frac{\partial}{\partial t}(\rho\vec{v}) + \nabla \cdot (\rho\vec{v}\vec{v}) = -\nabla p + \nabla \cdot \left[\mu\left(\nabla\vec{v} + \nabla\vec{v}^{T}\right)\right] + \rho\vec{g} + \vec{F} \tag{2.4}$$

With ρ the fluid density [kg/m^3], $\vec{v}$ the velocity vector [m/s], p the pressure [Pa], μ the dynamic viscosity [kg/(m·s)], $\vec{g}$ the gravitational acceleration vector [m/s^2], and $\vec{F}$ the external body forces [N/m^3].

Material properties: The material properties in these equations are determined based on the volume fractions of each phase in all cells. Equation 2.5 shows the calculation for properties in a cell on the interface with x being a random material parameter (e.g. viscosity or density), and x_b and x_o the material parameters for blood and Onyx, respectively [135].

$$x = x_b \cdot \alpha_b + x_o \cdot \alpha_o \tag{2.5}$$

Explicit approach: The explicit approach was chosen, as combined with the Geometric reconstruction scheme (see Section 2.2.4 *Solution Methods for CFD Simulations*), this is a more accurate and effective method for modeling two immiscible phases with a sharp interface compared to the implicit approach [135]. Using this approach, finite-difference interpolation schemes are applied to the volume fraction values from the previous time step (Equation 2.6 [135]).

$$\frac{\alpha_o^{n+1} \cdot \rho_o^{n+1} - \alpha_o^n \cdot \rho_o^n}{\Delta t} \cdot V + \sum_f (\rho_o \cdot U_f^n \cdot \alpha_{o,f}^n) = [\sum_{p=1}^{n} (\dot{m}_{bo} - \dot{m}_{ob}) + S_{\alpha_o}] \cdot V \tag{2.6}$$

With $(n+1)$ index for current time step [-], n index for previous time step [-], $\alpha_{o,f}$ face value of the Onyx volume fraction [-], $\rho_{o,f}$ face value of the Onyx density [kg/m^3], V volume of cell [m^3], U_f volume flux through the face [m^3/s] based on normal velocity, $\dot{m}_{ob}$ mass transfer from Onyx phase to blood phase [kg/s], $\dot{m}_{bo}$ mass transfer from blood phase to Onyx phase [kg/s], and α_o volume fraction of Onyx phase in a cell [-].

2.2.2 Simulation Setup

Simulations were conducted in ANSYS Fluent Solution (ANSYS Inc., Canonsburg, PA, USA). Transient simulations were conducted with the pressure-based solver, which is applicable since the Mach number is lower than 0.3 in this case (as the representative velocity is well below 471 m/s (Equation 2.7)), indicating incompressible flow [136, 137].

Mach number definition:

$$\mathrm{Ma} = \frac{V}{c} < 0.3 \Leftrightarrow V < 0.3 \cdot c = 0.3 \cdot 1570 \text{ m/s} = 471 \text{ m/s} \tag{2.7}$$

With V representative flow velocity $[m/s]$, and c speed of sound in the medium (here 1570 m/s for blood [137–139]).

The viscous laminar model was chosen, along with the VOF model considering a blood and Onyx phase. An explicit formulation for the volume fraction parameters and sharp interface modeling were employed. The material parameters are listed in Table 2.3. For simplicity, Onyx was considered a homogeneous suspension with mass-averaged properties instead of considering the EVOH and DMSO phases separately.

Table 2.3: Material parameters of blood and Onyx phase.

Material	**Density [kg/m^3]**	**Viscosity [kg/(m·s)]**
Onyx-18	1103.9	0.018
Blood	1063	0.004

2.2.3 Boundary Conditions

2.2.3.1 Velocity Inlet Boundary Conditions for Blood

Blood velocity profiles were applied at both inlets. The feeding arteries in this case were branches of the ACA and MCA (Figure 1.11 in Section 1.2.4.1 *Case Description*). Flow profiles in the ACA and MCA were obtained from the 1D cardiovascular Stergiopulos/Reymond model [9]. While patient-specific profiles would be ideal, they were unavailable; thus, ACA and MCA profiles were used and later scaled as described in this section. The model provides flow data over time at five nodes per arterial segment of a simplified arterial tree (Figure 2.13). Profiles were extracted from the middle nodes of segments 78 (ACA segment 2) and 73 (MCA segment 1), respectively, as the exact location was unknown and these profiles best matched

Doppler sonography and real-time DSA data from literature [9, 140, 141].

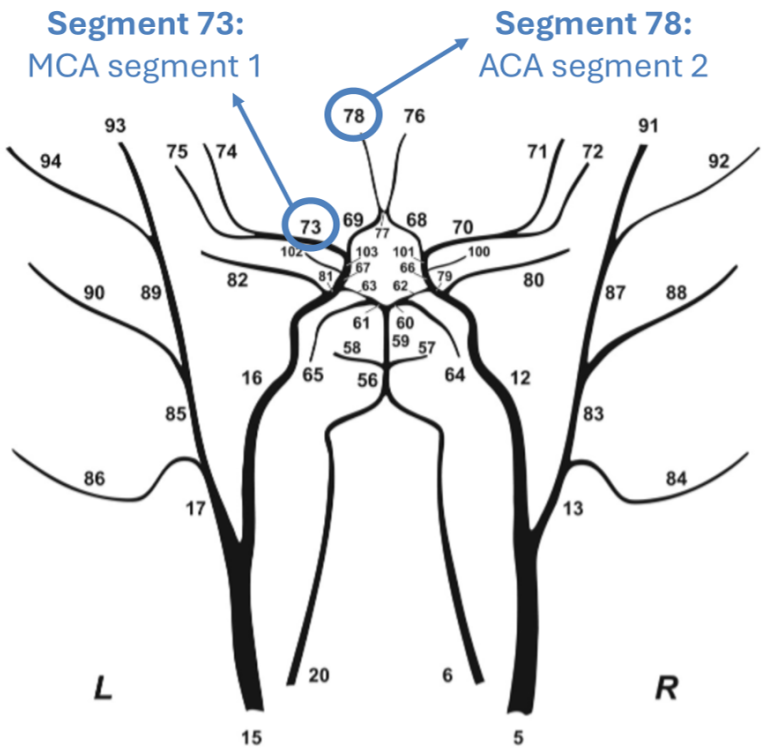

Figure 2.13: A schematic representation of the simplified cerebral arterial tree and corresponding segment numbering from the Stergiopulos/Reymond model. Data for segments 78 and 73 are extracted, representing segment 2 of the ACA and segment 1 of the MCA, respectively.
(Figure from [9])

The flow profiles were converted to velocity profiles using the cross-sectional inlet areas of the feeding arteries measured in Fluent. A Butterworth filter (4th order, 12 Hz cut-off frequency, 75 Hz sampling rate, without introducing time-latency) was applied for slight smoothing. Furthermore, the profiles were scaled to match typical mean velocities reported in literature. Specifically, a mean velocity of 0.0920 m/s for inlet 1 (ACA branch) and 0.1325 m/s for inlet 2 (MCA branch) were applied, based on phase contrast MRI flow measurements in distal ACA and MCA branches in healthy individuals [142]. The final input velocity profiles are shown in Figure 2.14.

Ideally, patient-specific velocity profiles and magnitudes from the feeding arteries would be used to reflect patient-specific flow, as velocities in AVMs can increase up to 160 % compared to normal [143]. However, this was not possible due to the absence of image frame rate data for this patient, a study limitation that should be addressed in future research.

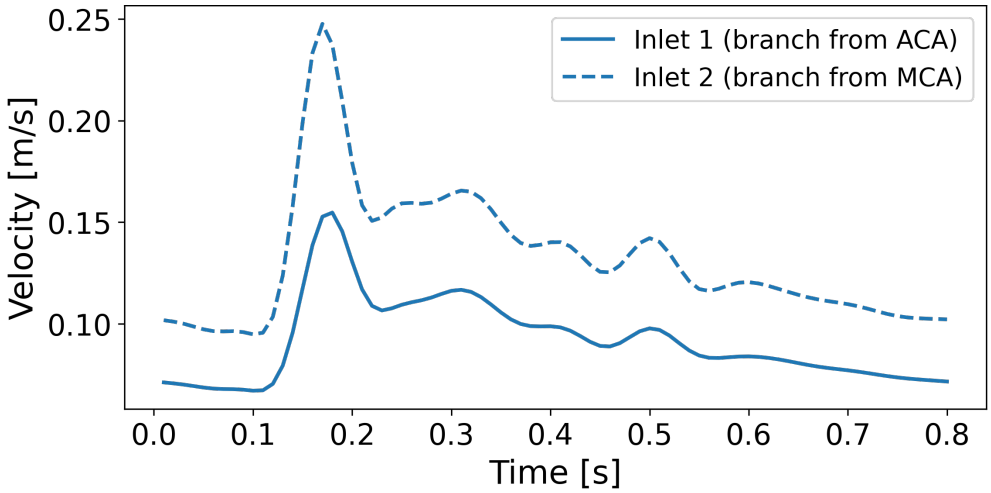

Figure 2.14: Input velocity profiles over time implemented as boundary conditions for blood in inlet 1 from the ACA (continuous line) and in inlet 2 from the MCA (dashed line).

2.2.3.2 Velocity Inlet Boundary Conditions for Onyx

Onyx was injected with a constant velocity from catheter 1, introduced in a branch of the ACA. Due to the unknown image frame rate for the patient's dataset, the actual Onyx injection velocity during the procedure could not be determined. Therefore, the FDA-recommended Onyx injection rate of 0.16 ml/min was used initially [114]. For the catheter in this model (with a diameter of 0.3302 mm), 0.16 ml/min corresponded to an injection velocity of 0.03114 m/s (Equation 2.8). To examine the influence of various injection velocities, simulations with double and half of the recommended rate were also conducted, corresponding to 0.08 ml/min (or 0.01557 m/s) and 0.32 ml/min (or 0.06228 m/s).

$$v = \frac{Q}{A} = \frac{0.16 \text{ ml/min}}{0.0856587 \times 10^{-6} \text{ m}^2} = \frac{0.002667 \times 10^{-6} \text{ m}^3/\text{s}}{0.0856587 \times 10^{-6} \text{ m}^2} \approx 0.03114 \text{ m/s} \tag{2.8}$$

With v Onyx injection velocity [m/s], Q recommended Onyx flow by FDA [m^3/s], and A the cross-sectional area of Onyx inlet surface from catheter 1 [m^2].

2.2.3.3 Vessel Wall Boundary Conditions

Vessel walls were assumed to be stationary with a no-slip boundary condition – a typical assumption in CFD to facilitate computational analysis. In reality, they are deformable and respond to blood flow forces exerted on them, but incorporating such deformations using FSI was beyond the scope of this thesis [126, 127].

2.2.3.4 Pressure Boundary Conditions

From DSA images, flow distributions across the two outlets could be derived. However, the employed VOF model is not compatible with outflow boundary conditions [135]. Therefore, an initial single-phase flow simulation with outflow boundary conditions was performed to determine appropriate pressure boundary conditions for the multi-phase case.

Outflow boundary conditions for single-phase flow case: Blood flow velocities at each outlet were determined as the distance traveled by the contrast agent between two successive images divided by the time interval between these images. The 3D distances along the centerlines were approximated in Mimics. Although the imaging frame rate and thus time between successive images were unknown for this dataset, this information was sufficient to determine the outflow distributions for the two outlets, as this quantity is independent of the time between two imaging frames. The calculations are shown in Equations 2.9 and 2.10, with x the unknown time between the successive image frames in Figure 2.15. 19.56 % of the flow was directed to outlet 1, corresponding to deep venous drainage, while 80.44 % of the flow was directed to outlet 2, corresponding to superficial venous drainage. A transient single-phase flow simulation was conducted with these outflow fractions assigned to the outlets, a constant blood velocity of 0.0920 m/s at inlet 1 and 0.1325 m/s at inlet 2, using 50 time steps of 0.001 ms reaching convergence (i.e. 10^{-3} residual drops) in each time step. The resulting pressures were 394.7783 Pa at inlet 1, 1039.2560 Pa at inlet 2, -16.3037 Pa at outlet 1, -70.9128 Pa at outlet 2, and 0.4950 Pa at the inlet for Onyx from catheter 1.

Outlet 1: For deep venous drainage

$$\text{Velocity}_{\text{outlet1}} = \frac{\text{distance}_{\text{outlet1}}}{\Delta t} = \frac{0.0252620\,\text{m}}{x\,\text{s}}$$

$$\Rightarrow \text{Outflow}_{\text{outlet1}} = \text{Velocity}_{\text{outlet1}} \cdot \text{Area}_{\text{outlet1}} = \frac{0.0252620}{x} \cdot 7.0087267 \cdot 10^{-6}\,\text{m}^3/s$$

Outlet 2: For superficial venous drainage

$$\text{Velocity}_{\text{outlet2}} = \frac{\text{distance}_{\text{outlet2}}}{\Delta t} = \frac{0.0848691\,\text{m}}{x\,\text{s}}$$

$$\Rightarrow \text{Outflow}_{\text{outlet2}} = \text{Velocity}_{\text{outlet2}} \cdot \text{Area}_{\text{outlet2}} = \frac{0.0848691}{x} \cdot 8.580108 \cdot 10^{-6}\,\text{m}^3/s$$

Flow distributions over outlets 1 and 2:

$$\begin{aligned}\text{Outflow}_{\text{total}} &= \text{Outflow}_{\text{outlet1}} + \text{Outflow}_{\text{outlet2}} \\ &= \left(\frac{0.0252620}{x} \cdot 7.0087267 \cdot 10^{-6}\,\text{m}^3/\text{s}\right) \\ &+ \left(\frac{0.0848691}{x} \cdot 8.580108 \cdot 10^{-6}\,\text{m}^3/\text{s}\right)\end{aligned}$$

$$\Rightarrow \text{Flow Percentage}_{\text{outlet1}} = \frac{\text{Outflow}_{\text{outlet1}}}{\text{Outflow}_{\text{total}}} \cdot 100\% = 19.56\% \tag{2.9}$$

$$\Rightarrow \text{Flow Percentage}_{\text{outlet2}} = \frac{\text{Outflow}_{\text{outlet2}}}{\text{Outflow}_{\text{total}}} \cdot 100\% = 80.44\% \tag{2.10}$$

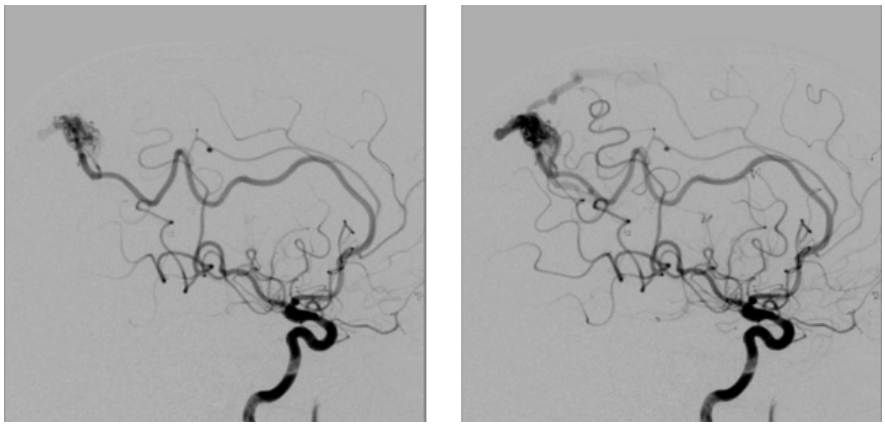

Figure 2.15: Two successive DSA images used to estimate the percentages of outflow in both of the outlets.

Pressure boundary conditions for multi-phase flow case: Results for pressures were obtained from the single-phase flow simulation discussed above. The resulting 394.7783 Pa at inlet 1, 1039.2560 Pa at inlet 2, and 0.4950 Pa at the Onyx inlet were applied as initial pressures (only at the start point of the simulation) at the respective planes; while -16.3037 Pa at outlet 1 and -70.9128 Pa at outlet 2 were applied at the outlets throughout the whole time of the multi-phase flow simulations. Note that, ideally, a time-varying profile should be applied at the outlets, which could be considered as part of future work.

2.2.4 Solution Methods for CFD Simulations

For the solution methods, the SIMPLE scheme was used for pressure-velocity coupling. For spatial discretization: Least Squares Cell Based was used for the gradient, PRESTO! for pressure, and Second Order Upwind for momentum. For the volume fraction, Geo-Reconstruct

was applied. Under-relaxation factors were set to 0.3, 1, 1, and 0.7 for pressure, density, body forces, and momentum, respectively. Monitored residuals were normalized and scaled, with a relative convergence criterion of 10^{-4}, to ensure a relative 10^{-3} drop of all residuals in each time step. Standard initialization was used for the single-phase simulations with only blood, whereas for the multi-phase simulations, first, two cycles with only blood were simulated before the injection of Onyx. For all cases, with only blood or for the different Onyx injection rates, three blood flow cycles were simulated, covering a 2.40 s period.

Geometric reconstruction scheme: When employing the geometric reconstruction scheme (suitable for unstructured meshes), standard interpolation is used to obtain face fluxes in cells fully filled with one phase, while interface cells use geometric reconstruction. This scheme assumes a linear interface within each cell [135]. Firstly, the interface position is determined based on volume fractions and their derivatives. Secondly, fluid advection through each face is determined using this interface and velocity distributions. Thirdly, volume fractions are updated using the flux balance from the previous step [135].

2.2.5 Convergence assessment

For this study, a time step was considered converged when the continuity, x-velocity, y-velocity, and z-velocity residuals all decreased relatively by at least three orders of magnitude (a popular convention [144]). Table 2.4 shows the number of converged time steps for each simulation. It is important to note that the lack of convergence in some time steps was primarily due to limited time and computational resources. Given more time and resources, convergence would likely be achieved for all time steps, and no fundamental numerical issues are expected. Appendix C: *Convergence Evaluation of CFD Simulations* includes further explanation on convergence and a visual representation of convergence for each simulation.

Table 2.4: Amount of converged time steps per conducted simulation. The convergence criterion was defined as a relative drop of at least three orders of magnitude for all residuals.

	Number of converged time steps	**Percentage of converged time steps**
Simulation without Onyx (only blood)	220/240	91.67 %
Simulation with Onyx injection at 0.08 ml/min	204/240	85.00 %
Simulation with Onyx injection at 0.16 ml/min	199/240	82.92 %
Simulation with Onyx injection at 0.32 ml/min	202/240	84.17 %

2.3 Methods for Quantification of Onyx Distribution

To quantify the distribution of Onyx through two downstream branches for the analysis in Section 3.1.2 *Onyx Progression over Time for Various Injection Rates*, the mass flow rate of the Onyx phase was calculated through two cross-sectional planes, each located at the start of one of the branches (visualized in Figure 2.16). The goal was to measure how much Onyx mass entered each branch over time and how this distribution changed for different injection rates. This section presents the mathematical formulation used, while the calculations were performed in ANSYS Fluent (with the detailed Fluent workflow provided in Appendix D: *Workflow in Fluent for Mass Flow Rate Calculations*).

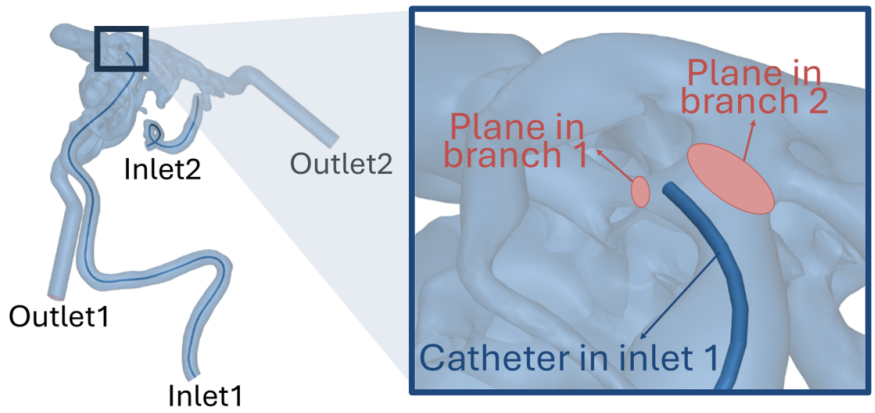

Figure 2.16: Indication of the two branches after the injection site and the location of the planes in each branch over which the mass flow rates were calculated.

The mass flow rate of Onyx through each plane at a certain time point was calculated using Equation 2.11. This equation sums the local contributions over all faces of the selected surface, yielding the instantaneous mass flow rate of Onyx through a plane $\dot{m}_{\text{o, through plane}}$.

Mass flow rate of Onyx through a plane:

$$\dot{m}_{\text{o, through plane}} = \sum_{\text{all faces i of plane}} \rho_o \cdot v_i \cdot \alpha_{o,i} \cdot A_i \tag{2.11}$$

With $\dot{m}_{\text{o, through plane}}$ mass flow rate of Onyx through a plane [kg/s], ρ_o density of Onyx [kg/m^3], v_i velocity in face i [m/s], $\alpha_{o,i}$ volume fraction of Onyx in face i [-], and A_i area of face i [m^2].

To obtain the total mass of Onyx that passed through each plane over a given time period T, the mass flow rates were integrated across all time points in period T using Equation 2.12.

In this equation, the instantaneous mass flow rate at each saved time point t_i is multiplied by the corresponding time interval Δt (0.10 s in this study, equal to 10 time steps of 0.01 s), and the results are summed over time. This provides the cumulative mass $m_{\text{o, through plane, T}}$ of Onyx through the plane over time T.

Mass of Onyx through a plane over certain time period:

$$m_{\text{o, through plane, T}} = \sum_{\substack{t_i \in [0,T] \\ \Delta t \text{ intervals}}} \dot{m}_{\text{o, through plane}}(t_i) \cdot \Delta t \tag{2.12}$$

With $m_{\text{o, through plane, T}}$ mass of Onyx through plane over time T [kg], $\dot{m}_{\text{o, through plane}}(t_i)$ mass flow rate of Onyx through a plane at time t_i [kg/s], and Δt the length of the time interval [s] (in this thesis always 0.10 s).

To obtain the percentage of mass going through branch 1 or 2, assuming all Onyx goes either through branch 1 or branch 2, is given by Equation 2.13. In Section 3.1.2 *Onyx Progression over Time for Various Injection Rates* this will be evaluated for T being one or multiples of the cardiac cycle duration of 0.8 s.

Percentage of mass going through a certain branch over a certain time period:

$$\begin{aligned} m_{\text{o, percentage through branch 1, T}} &= \frac{m_{\text{o, through plane in branch 1, T}}}{m_{\text{o, through plane in branch 1, T}} + m_{\text{o, through plane in branch 2, T}}} \cdot 100\% \\ m_{\text{o, percentage through branch 2, T}} &= \frac{m_{\text{o, through plane in branch 2, T}}}{m_{\text{o, through plane in branch 1, T}} + m_{\text{o, through plane in branch 2, T}}} \cdot 100\% \end{aligned} \tag{2.13}$$

With $m_{\text{o, percentage through branch 1, T}}$ the percentage of the total mass of Onyx injected over time T going through branch 1 [%], $m_{\text{o, percentage through branch 2, T}}$ the percentage of the total mass of Onyx injected over time T going through branch 2 [%], $m_{\text{o, through plane in branch 1, T}}$ the mass of Onyx going through the plane in branch 1 over time T [kg], and $m_{\text{o, through plane in branch 2, T}}$ the mass of Onyx going through the plane in branch 2 over time T [kg].

Chapter 3

Results and Discussion

3.1 Results and Interpretation

3.1.1 Baseline AVM Hemodynamics Prior to Onyx Injection

Before investigating the impact of the Onyx injection rate on embolic agent distribution and local hemodynamics, the baseline case—prior to any embolization—is examined. This baseline case involved simulating blood flow within the AVM, with no Onyx injection yet included. This analysis focuses on visualizing flow path lines and pressure distributions to gain insights into the hemodynamic behavior of this AVM model. Additionally, the distribution of outflow between outlet 1 (deep venous drainer) versus outlet 2 (superficial cortical venous drainer) over time was analyzed to validate the implemented outlet boundary conditions.

3.1.1.1 Pressure contours at a Selected Time Point

Figure 3.1 presents simulation results for pressure contours at 0.40 s into the second simulated blood flow cycle—a moment where inlet velocities are close to their average values, as shown in Figure 3.1.a. The corresponding static pressure distribution over the vessel wall is shown in Figure 3.1.b and also facet-averaged static pressures in selected cross-sectional planes near the nidus and at main inlets and outlets are included (so these values were calculated over the whole cross-section, not only the wall). Given the use of pressure outlet boundary conditions, examining absolute pressure values in the model is of importance [135].

Near the nidus, the pressure values are 30.70 Pa at the plane in inlet 1, 181.20 Pa at the plane in inlet 2, -15.11 Pa at the plane in outlet 1, and -39.87 Pa at the plane in outlet 2. Further upstream at the main inlets, the facet-averaged static pressures reach 233.45 Pa in

inlet 1 and 652.40 Pa in inlet 2. On the other hand, the pressures at the main outlets were -16.30 Pa in outlet 1 and -70.91 Pa in outlet 2. As visualized in Figure 3.1.b, the highest static pressure magnitudes are observed at the most upstream parts of the feeding arteries (inlets 1 and 2), with a gradual decrease towards the draining veins (outlets 1 and 2).

The obtained results for static pressures in the single-phase flow CFD simulations provide insight into the hemodynamic situation within the AVM of this specific patient. The calculated pressure drop from the conducted simulations is 277.06 Pa between inlet 1 and the average of the two outlets, and 696.01 Pa between inlet 2 and the average of the two outlets. These calculated pressure differences between the inlets and outlets are lower than the typical drop across healthy cerebral capillaries (around 70 mmHg (= 9333 Pa) [124]) due to the characteristic low-resistance arteriovenous shunting in AVMs. Overall, these pressure differences are slightly lower but still of the same order of magnitude as the 10 mmHg (= 1333 Pa) reported in literature for AVMs [8]. It is important to note that these pressure drops are significantly dependent on the specific AVM geometry and flow conditions [61]. However, this relatively lower pressure difference could be attributed to the applied blood inlet velocity profiles that were based on data from healthy subjects (see Section 2.2.3.1 *Velocity Inlet Boundary Conditions for Blood* [142]), which are likely lower than velocities in the typically enlarged arterial feeders of AVMs [143]. The hemodynamic analog of Ohm's law (Equation 1.1) explains that lower flow rates – for example, resulting from underestimated inlet velocities – are associated with smaller pressure drops for a given vascular resistance, so underestimated inlet velocities could lead to an underestimated pressure gradient over the AVM.

Furthermore, the higher pressure difference observed for inlet 2 (branch from MCA) compared to inlet 1 (branch from ACA) can likely be explained by the applied velocity inlet boundary conditions (see Section 2.2.3.1 *Velocity Inlet Boundary Conditions for Blood*) and the vascular resistance of the inlets. The pressure difference over an inlet is proportional to the product of the vascular resistance and the flow according to the hemodynamic analog of Ohm's law (Equation 1.1). In this model, inlet 1 has a larger cross-sectional area ($5.434 \cdot 10^{-6}\,\mathrm{m}^2$) and a lower assigned average velocity (0.0920 m/s), resulting in an average flow rate of $4.999 \cdot 10^{-7}\,\mathrm{m}^3/\mathrm{s}$. Conversely, inlet 2 has a smaller cross-sectional area ($3.034 \cdot 10^{-6}\,\mathrm{m}^2$) and a higher assigned average velocity (0.1325 m/s), leading to a slightly lower average flow rate of $4.021 \cdot 10^{-7}\,\mathrm{m}^3/\mathrm{s}$. However, the vascular resistance is also highly sensitive to the vessel radius. According to Hagen-Poiseuille's law, resistance is inversely proportional to the fourth power of the vessel radius ($R \propto \frac{1}{r^4}$), as seen in Equation 1.3 (although the theoretical assumptions of this law are not strictly satisfied in this complex case, it still offers intuitive insights into

the these relations). Given that inlet 2 has a smaller circular equivalent diameter (1.97 mm) compared to inlet 1 (2.63 mm), the resistance in inlet 2 is remarkably higher. When considering the dependence of the pressure difference on both flow and vascular resistance, this explains the greater pressure drop across inlet 2 observed in Figure 3.1.b.

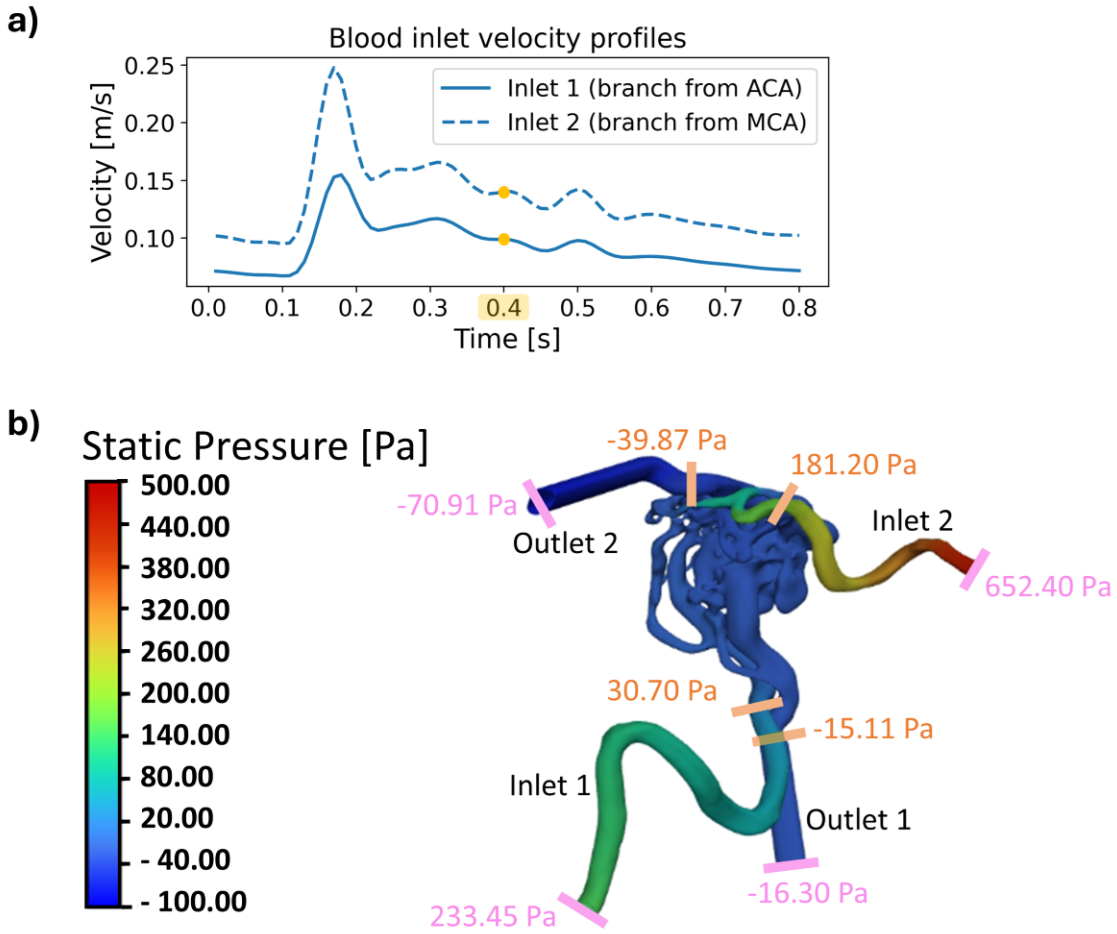

Figure 3.1: a) The chosen time point for figure in panel b) is shown on the inlet velocity profiles: 0.40 s into the second blood flow cycle with inlet velocities near average values. **b)** Static pressure contours on the AVM vessel walls, with a color scale from -100 Pa (deep blue) to 500 Pa (dark red). Orange lines indicate planes in all in-and outlets close to the nidus, while pink lines indicate the in-and outlets, for which the facet-averaged static pressures are indicated (these values were calculated over the whole cross-section, not only the outer vessel wall).

3.1.1.2 Velocity Path Lines at a Selected Time Point

Figure 3.2 presents simulation results again at 0.40 s into the second simulated blood flow cycle—when inlet velocities are close to their average values (see Figure 3.2.a). The corresponding flow path lines colored by their velocity magnitudes are displayed in Figure 3.2.b.

In Figure 3.2.b, the velocity magnitudes in inlet 2 (branch from MCA) are visibly higher than in inlet 1 (branch from ACA). Within the nidus itself, a range of velocity magnitudes between 0 and 0.1699 m/s is observed, although the spatial resolution is limited in this region (as discussed in Section 2.1.1 *Data Acquisition*).

The simulated velocity fields reflect the applied inlet velocity boundary conditions, with higher velocities in inlet 2 (MCA branch), consistent with the literature values used for scaling. As detailed in Section 2.2.3.1 *Velocity Inlet Boundary Conditions for Blood*, the average inlet velocities were 0.0920 m/s for inlet 1 (branch from ACA) and 0.1325 m/s for inlet 2 (branch from MCA) [142]. In CFD simulations, inlet velocity boundary conditions significantly influence the further development of velocity profiles downstream and are critical determinants of the resulting flow fields [145, 146]. In reality, arterial feeders are typically enlarged, and patient-specific velocities in these feeders can be significantly higher (up to 160 % higher) than normal [143]. This highlights a limitation of using literature values and the importance of using patient-specific inlet boundary conditions in future work (further discussed in Section 3.3.1 *Personalized Boundary Conditions*).

It should also be noted that the vessels in the center of the nidus are not fully resolved in the model due to the limited imaging resolution (as discussed in Section 2.1.1 *Data Acquisition*), which results in an under-representation of the microvasculature within the nidus. So, what in reality are multiple small vessels, is represented in this model as one big zone, artificially increasing the cross-sectional area and thus underestimating the flow velocities in that region, since—according to the conservation of flow (Equation 3.1)—an increase in area corresponds to a decrease in velocity for an incompressible fluid. Consequently, the true hemodynamic behavior in the nidus core is likely to involve more complex and higher-velocity flow patterns than captured in the current model.

Conservation of flow:

$$\text{Starting from the conservation of mass: } \dot{m}_1 = \dot{m}_2$$
$$\text{Expressing mass flow rate as } \dot{m} = \rho \cdot A \cdot v : \rho_1 \cdot A_1 \cdot v_1 = \rho_2 \cdot A_2 \cdot v_2$$
$$\text{For incompressible flow, where } \rho_1 = \rho_2 = \text{constant},$$
$$\text{this simplifies to: } Q_1 = A_1 \cdot v_1 = A_2 \cdot v_2 = Q_2 \tag{3.1}$$

With $\dot{m}$ the mass flow rate [kg/s], ρ the fluid density [kg/m^3], A the cross-sectional area [m^2], v the average velocity [m/s], and Q the volumetric flow rate [m^3/s].

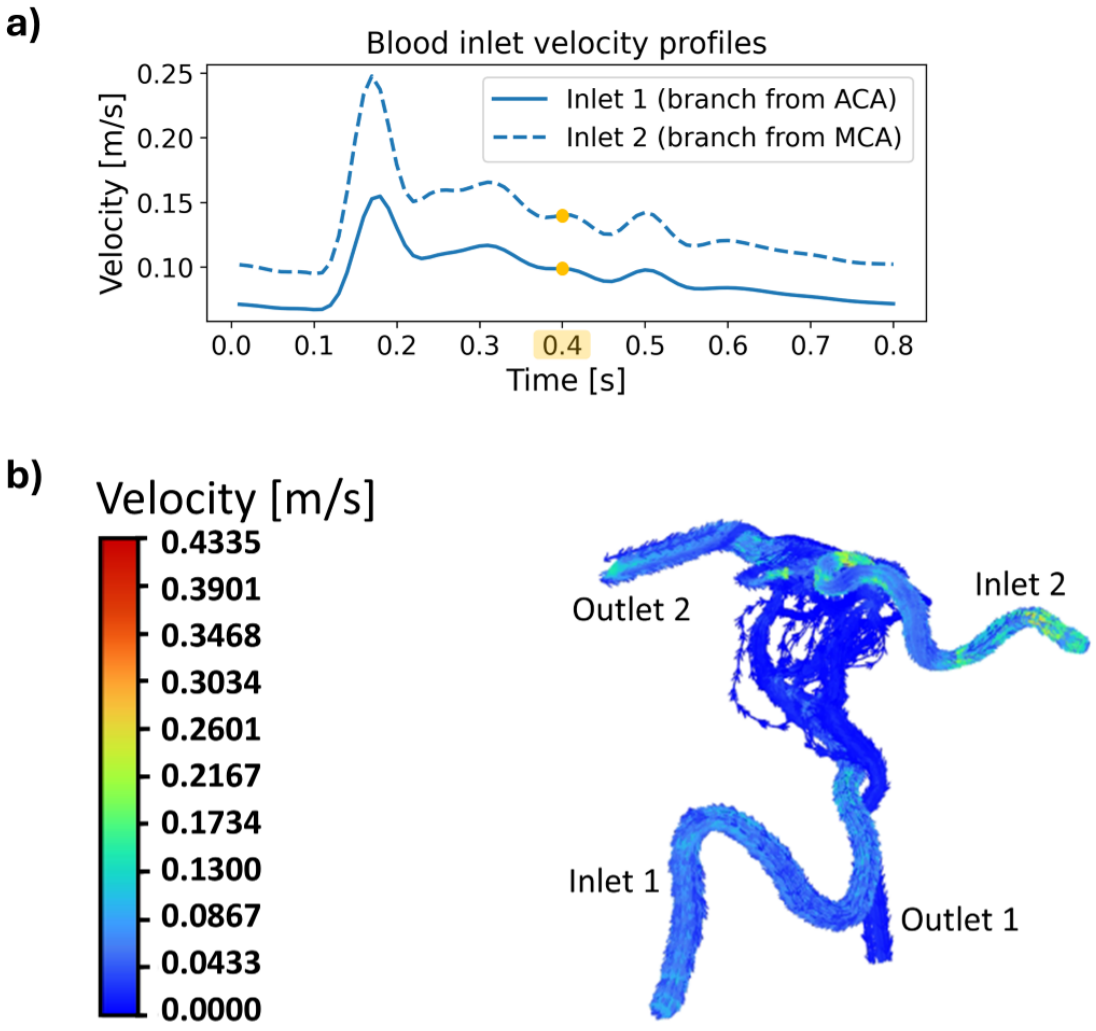

Figure 3.2: a) The chosen time point for figure in panel b) is shown on the inlet velocity profiles: 0.40 s into the second blood flow cycle with inlet velocities near average values. **b)** Path lines through the AVM geometry, with color indicating velocity magnitudes from 0 m/s (deep blue) to 0.4335 m/s (dark red) and arrows indicating flow directions.

3.1.1.3 Outflow Fractions over Time

Figure 3.3 shows the outflow fractions over outlet 1 versus outlet 2 over time for two blood flow cycles, with the inlet velocity profiles plotted in the same figure to provide context for the timeline. Outlet 1 of the model corresponds to the deep venous drainer towards the great cerebral vein, while outlet 2 refers to the superficial venous drainer being a cortical vein going towards the superior sagittal sinus. As detailed in Section 2.2.3.4 *Pressure Boundary Conditions*, the patient-specific outflow distribution was estimated as 19.56 % over outlet 1 and 80.44 % over outlet 2, but pressure outlet boundary conditions were applied to be compatible with the VOF model. In Figure 3.3, over a time period of 1.60 s, the outflow fraction through outlet 1 ranges over time from minimally 0.39 to maximally 39.53 % with a mean value of 10.86 %, while the outflow fraction through outlet 2 ranges from 60.47 to 99.61 % with a mean value of 89.14 %.

Over the 1.60 s period indicated in Figure 3.3, the outflow fractions towards outlet 1 and outlet 2 seem to fluctuate approximately around the calculated 19.56 % and 80.44 %, with the vast majority of outflow consistently going towards outlet 2. This suggests that the boundary condition implementation effectively reflects the patient-specific outflow fractions derived from DSA data. However, ideally, a time-varying profile would be applied at the outlets as a boundary condition instead of one fixed value (see further in 3.3.1 *Personalized Boundary Conditions*).

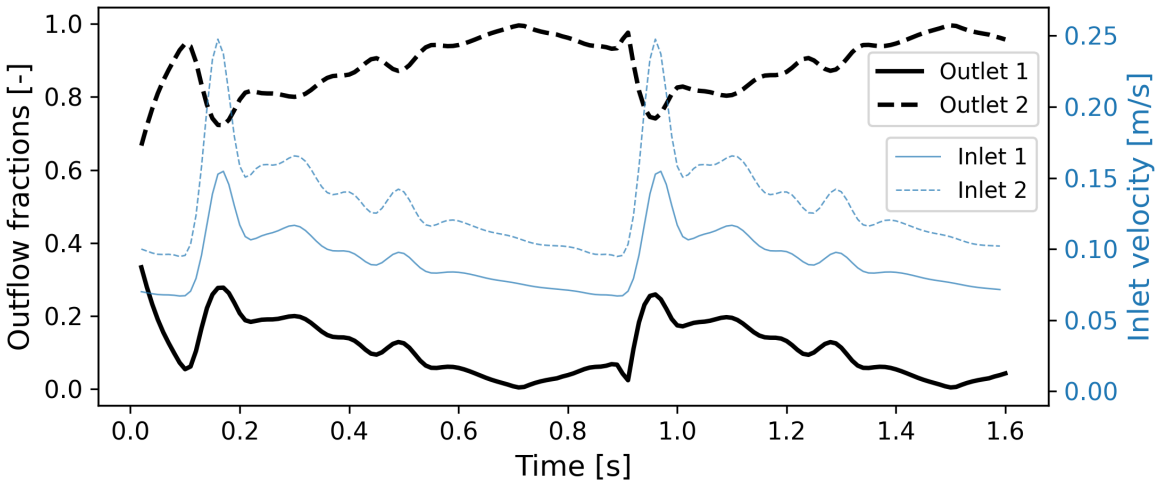

Figure 3.3: Outflow fractions to outlets 1 and 2 over time for two blood flow cycles, indicated in full and dashed black lines, respectively. The inlet velocity profiles at inlets 1 and 2 are also added in this figure (full and dashed light blue lines, respectively) to provide some context on the timeline. Outlet 1 is the deep venous drainer towards the great cerebral vein, outlet 2 the superficial cortical venous drainer going towards the superior sagittal sinus, inlet 1 the branch from the ACA, and inlet 2 the branch from the MCA.

A remarkable observation from Figure 3.3 is that the outflow fraction through outlet 1 in this model increases relatively during periods of high inlet velocity, approximately following the same profile over time as the inlet velocities. This behavior can be explained by examining the origin of the flow path lines in the model. Figure 3.4 shows the flow path lines in the model (colored by velocity magnitude) originating from inlet 1 and 2 together but also separately, again at 0.40 s into the second blood flow cycle as in Figure 3.2, but similar trends could be observed at other time points.

In this model of the AVM, flow lines coming from inlet 1 distribute over both outlet 1 and outlet 2, whereas flow lines from inlet 2 exit exclusively through outlet 2 (Figure 3.4). This means that outlet 1 receives flow only from inlet 1, while outlet 2 receives contributions from both inlets. As a result, the flow rate at outlet 1 is more directly controlled by the inlet velocity at inlet 1. During periods of high inlet 1 velocity, the outflow through outlet 1 increases proportionally, explaining the stronger correlation. In contrast, outlet 2 integrates flow from both inlets, leading to more complex interactions and less direct correspondence with a single inlet profile. This explains why its outflow fraction does not scale with the inlet velocity profiles but rather indicates the complement of the outlet 1 fraction. It is important to emphasize that this flow behavior is strongly influenced by the model of the AVM and the simulation setup, including boundary condition choices and the limited spatial resolution of the reconstructed nidus. As explained in the above Section 3.1.1.2 *Velocity Path Lines at a Selected Time Point*, the central part of the nidus is under-resolved due to limitations of the 0.44 mm imaging resolution. So, in reality, this zone likely exhibits more complex and higher-velocity flow patterns, which would affect the mixing and redistribution between outlets. Therefore, while the trends observed in Figure 3.4 explain the correlation between the outflow fraction towards outlet 1 and the inlet velocities seen in Figure 3.3, these trends may not fully reflect true physiological behavior due to modeling limitations, and further research using alternative boundary conditions and more anatomically accurate vascular geometries would be necessary to confirm these observations with more certainty.

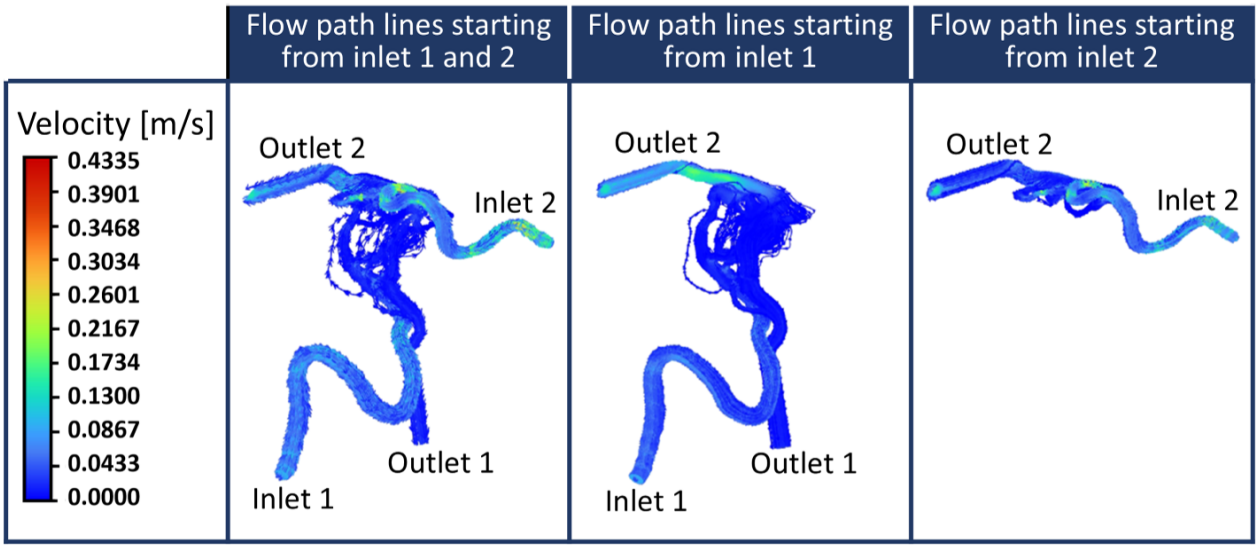

Figure 3.4: Flow path lines through the AVM geometry, colored by their velocity magnitudes from 0 m/s (deep blue) to 0.4335 m/s (dark red) and arrows indicating flow directions. The left panel indicates flow path lines coming from both inlets of the model. The middle panel selectively shows the flow path lines coming from inlet 1 (branch of the ACA). The right panel selectively shows the flow path lines coming from inlet 2 (branch of the MCA). Outlet 1 is the deep venous drainer towards the great cerebral vein, outlet 2 the superficial cortical venous drainer going towards the superior sagittal sinus, inlet 1 the branch from the ACA, and inlet 2 the branch from the MCA.

3.1.2 Onyx Progression over Time for Various Injection Rates

Visualization of Onyx progression over time for various injection rates is illustrated in Figures 3.5 and 3.6. Figure 3.5 shows the cells of the model where Onyx is present in a red color for various injection rates over time, while Figure 3.6 shows the volume fractions of the Onyx phase indicated by a color scale (from deep blue for 0 to dark red for 1) in certain planes that were defined near the injection site. Both figures depict the same zone of the AVM from the same point of view to allow consistent comparison.

From these figures, it can be seen that Onyx spreads over two downstream branches closely after the injection site. To also quantitatively assess the distribution of Onyx over these downstream branches, the mass flow rates through two planes (each at the start of one of these branches, see Figure 3.7.a) were computed as explained in Section 2.3 *Methods for Quantification of Onyx Distribution*. Figure 3.7.b shows the cumulative fraction of Onyx mass injected over a certain time period that passed through branch 1 (solid bars) versus branch 2 (dashed bars) for various injection rates (0.08, 0.16, and 0.32 ml/min). The mass flow rates were calculated using Equation 2.11, the mass of Onyx through a plane over a certain time was calculated using Equation 2.12, and the percentages of mass through branch 1 versus branch 2 were calculated using Equation 2.13 (as explained in Section 2.3 *Methods for Quantification of Onyx Distribution*). On this plot, for example, the value at 0.30 s through branch 1 for injection rate 0.32 ml/min equals 0.8134 (height of the third solid orange bar); this means that over a period of 0.30 s, 81.34 % of the injected mass of Onyx (i.e. the mass of Onyx that is injected after injecting for 0.30 s at 0.32 ml/min) passed through branch 1, and thus 18.66 % must have passed through branch 2. Table 3.1 lists the values of these cumulative percentages of injected Onyx that passed through each branch over a time period of one, two, or three blood flow cycles for the various injection rates.

Figures 3.5 and 3.6 show Onyx progression over time for various injection rates. As expected, higher injection rates lead to further propagation of Onyx within the vasculature within a given time. This is logical, as injecting more volume per minute naturally pushes the Onyx further into the vessels, and if a substance is injected faster, it covers more distance within the same amount of time.

Furthermore, a consistent trend is observed across all three injection rate scenarios: initially, Onyx primarily flows to branch 1, while a smaller portion goes to branch 2 (Table 3.1: 93.66 %, 76.60 %, and 51.86 % towards branch 1 over one cycle for injection rates 0.08, 0.16, and 0.32 ml/min, respectively). However, as time progresses, a growing fraction of

the Onyx is going toward branch 2 compared to earlier (Table 3.1: after two cycles only 82.43 %, 57.78 %, and 42.07 % towards branch 1, and after three cycles, only 74.35 %, 51.02 %, and 39.06 % towards branch 1 for injection rates 0.08, 0.16, and 0.32 ml/min, respectively). The initial trend of more Onyx going towards branch 1 than branch 2 can likely be explained by the position and orientation of the catheter in the geometry, which is oriented more towards branch 1. CFD studies in other medical contexts also demonstrated the influence of the catheter location on the initial flow direction [147–150]. Over time, Onyx starts to go more towards branch 2, which can probably be explained by the accumulation of Onyx in branch 1, causing increased resistance to flow in that branch due to the higher viscosity of Onyx. Hagen-Poiseuille's law (Equation 1.3) can provide intuitive insight into this observation. Although the assumptions underlying this law (i.e. steady, laminar flow of incompressible, Newtonian fluid in a cylindrical tube) are not satisfied in this complex case, the law illustrates that increased viscosity relates to increased flow resistance, a trend that remains qualitatively applicable even outside the idealized conditions of the law. As fluid flow follows the path of least resistance [59], Onyx is now increasingly directed into branch 2, where flow is still less obstructed. This redistribution toward branch 2 is also consistent with theoretical models on flow through AVMs based on Darcy's law and Maag's formula [151]. According to Darcy's law, the flow rate through a branch depends on the material properties of the medium, i.e. less flow if a higher viscosity [151]. Maag's formula indicates that the diffusion radius (a measure for Onyx spread in the vasculature) is inversely proportional to the viscosity [151]. So, in regions where Onyx has already accumulated and viscosity is higher, further spread into that region is reduced. These conclusions are compatible with the findings in this thesis of Onyx redistribution towards branch 2 over time. While again not all theoretical assumptions of these laws are met, their general insights remain more broadly applicable. So, in summary, the interplay of catheter positioning and evolving hemodynamic resistance influences the distribution of Onyx in the vasculature.

Moreover, Figures 3.5 and 3.6 and Table 3.1 demonstrate that the injection rate affects the extent and timing of this Onyx redistribution over the downstream branches, which was explained in the above paragraph. At higher injection rates, a larger fraction of Onyx is directed toward branch 2 earlier in the injection process. For example, after two cycles for an injection rate of 0.32 ml/min, the majority (57.93 %) of injected Onyx went to branch 2. In contrast, at the lower rate of 0.08 ml/min, branch 1 still received the majority (82.43 %) of injected Onyx over two blood flow cycles (Table 3.1). This observation can probably be explained as follows: higher injection rates accelerate the Onyx accumulation in branch

1, which increases flow resistance there more rapidly. As a result, flow is redirected toward branch 2 sooner and more substantially. The observed differences in Onyx distribution across the branches at varying injection rates might be attributed to both the total volume or mass of Onyx delivered and the rate of its administration. Higher injection rates not only introduce a greater mass of Onyx that will accumulate over a given time but also deliver this mass with an increased velocity. To illustrate the effect of the injection rate parameter, the following comparisons from Table 3.1 can be considered:

- Comparison 1: Case for 0.16 ml/min after one cycle (76.60 % to branch 1, 23.40 % to branch 2) versus case for 0.08 ml/min after two cycles (82.43 % to branch 1, 17.57 % to branch 2)

- Comparison 2: Case for 0.32 ml/min after one cycle (51.86 % to branch 1, 48.14 % to branch 2) versus case for 0.16 ml/min after two cycles (57.78 % to branch 1, 40.22 % to branch 2)

For both these comparisons, despite the same total mass of Onyx being delivered in the two compared cases, the cases with the higher injection rate led to greater portions of Onyx being redirected towards branch 2. The rate of injection is thus a key parameter in determining the Onyx distribution after injection.

Figure 3.7.b enforces these discussed observations and explanations, but gives some additional information on the redistribution of Onyx over time compared to Table 3.1. Firstly, for the lowest injection rate (0.08 ml/min, in blue), more mass flows towards branch 1 compared to branch 2 at each time point over the whole 2.40 s period. Only from 0.50 s on, the contribution towards branch 2 becomes visible, although still relatively low (1.50 %). Over time, the fraction of injected mass going through branch 1 decreases gradually, but after 2.40 s still the majority (74.35 %) goes through branch 1. Secondly, for the recommended Onyx rate (0.16 ml/min, in green), the contribution of branch 2 becomes clear at an earlier time point, specifically at 0.20 s a fraction of 1.51 %. The redistribution of relatively more flow going toward branch 2 occurs more rapidly in this case compared to the lowest injection rate case, as indicated by the faster decline in the height of the solid green bars relative to the solid blue bars. After 2.40 s, the mass is nearly equally distributed between branches 1 and 2, with 51.02 % passing through branch 1. If the simulation were extended slightly beyond 2.40 s, potentially the majority of the injected mass would eventually shift toward branch 2, assuming the current trend continues. Lastly, for the highest injection rate (0.32 ml/min, in orange), the fraction toward branch 2 is visible from the start, 0.54 % after 0.10

s and already 10.28 % after 0.20 s. The redistribution towards branch 2 happens sooner for this higher injection rate than in the other two cases, as reflected by the faster decline in height of the solid orange bars relative to the solid blue and green bars. For this case, the fraction towards branch 2 becomes higher than towards branch 1 from 0.90 s on: at this time point the majority of 51.11 % of the injected mass has gone through branch 2. This shift in distribution is visually represented in Figure 3.7.b by the cross-over of the solid and dashed orange bars.

The findings discussed in this section suggest important clinical implications. The results highlight the importance of the Onyx injection rate as a key controllable parameter during embolization. Faster injection rates not only accelerate the progression of the embolic agent but also influence its distribution between downstream branches. This suggests that uncontrolled or excessively high injection rates could potentially increase the risk of non-target embolization. In addition, the role of catheter placement is also critical. As shown in this study, and supported by CFD research in other medical contexts [147–150], initial flow direction is significantly influenced by the catheter's orientation within the vessel. A catheter aimed more directly at one branch can initially favor Onyx entry into that branch, but evolving flow resistance due to Onyx accumulation can shift flow direction dynamically. In clinical practice, this means that to achieve desirable embolization results, clinicians must carefully plan both the injection rate protocol and catheter positioning. Moreover, these results also highlight the potential of pretreatment CFD modeling as a decision-making tool to simulate various injection strategies, potentially improving the safety and efficacy of endovascular embolization procedures in the long term.

Table 3.1: Mass distribution through branches indicated in Figure 3.7.a over one cycle (0.80 s), two cycles (1.60 s), and three cycles (2.40 s) for various Onyx injection rates.

	Onyx injected at 0.08 ml/min		**Onyx injected at 0.16 ml/min**		**Onyx injected at 0.32 ml/min**	
	Through branch 1	**Through branch 2**	**Through branch 1**	**Through branch 2**	**Through branch 1**	**Through branch 2**
After one cycle (0.80 s)	93.66 %	6.34 %	76.60 %	23.40 %	51.86 %	48.14 %
After two cycles (1.60 s)	82.43 %	17.57 %	57.78 %	40.22 %	42.07 %	57.93 %
After three cycles (2.40 s)	74.35 %	25.65 %	51.02 %	48.98 %	39.06 %	60.94 %

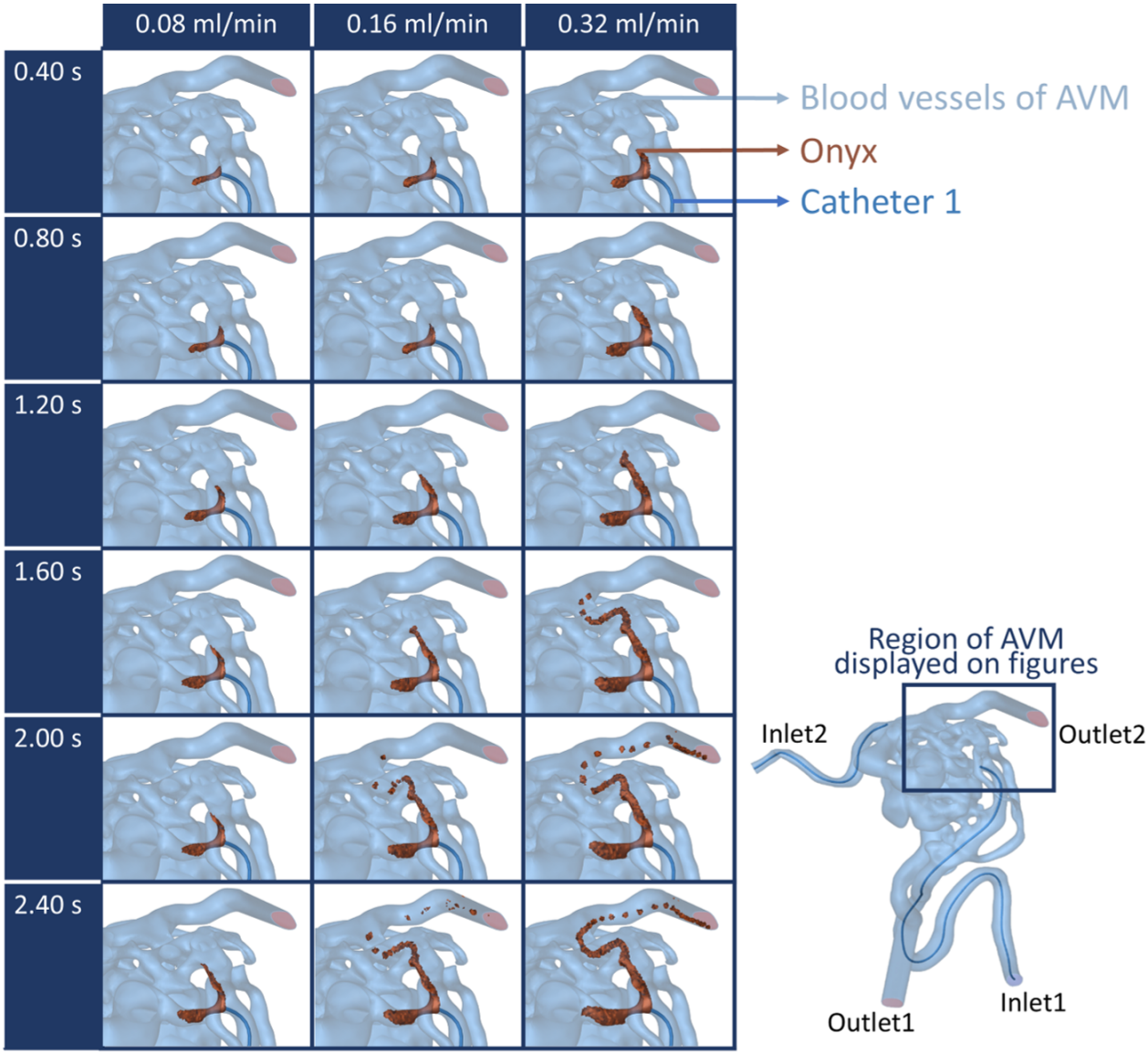

Figure 3.5: Progression of Onyx over time for various injection rates (0.08, 0.16, and 0.32 ml/min). The vessels of the AVM are seen in light blue and are made transparent to visualize Onyx in dark red and catheter 1 (from where Onyx is injected) in dark blue. The red color indicates cells that contain Onyx, but are not necessarily fully filled with Onyx: the criterion to indicate the cells red was a volume fraction for the Onyx phase greater than 10^{-6}. On the bottom right, the zone of the AVM depicted in the pictures in the table is indicated (same zone as in Figure 3.6).

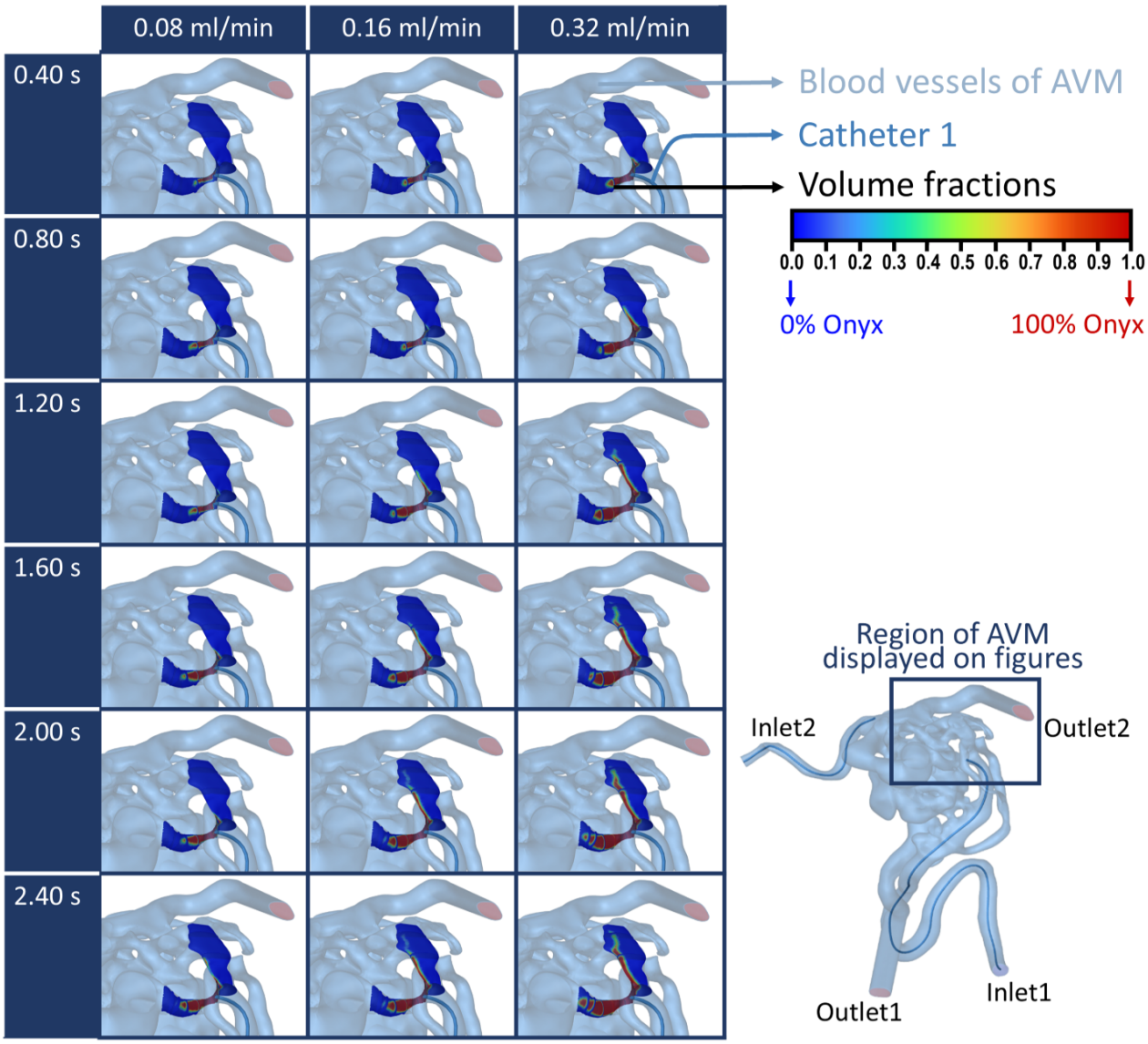

Figure 3.6: Spread of Onyx over time visualized in various planes around the injection site for various injection rates (0.08, 0.16, and 0.32 ml/min). The vessels of the AVM are seen in light blue and are made transparent to visualize catheter 1 (from where Onyx is injected) in dark blue and the volume fraction of Onyx in the defined planes. For the volume fractions, a deep blue color indicates 0 % Onyx in the cell (i.e. fully filled with blood) and a dark red color indicates 100 % Onyx in the cell. On the bottom right, the zone of the AVM depicted in the pictures in the table is shown (same zone as in Figure 3.5).

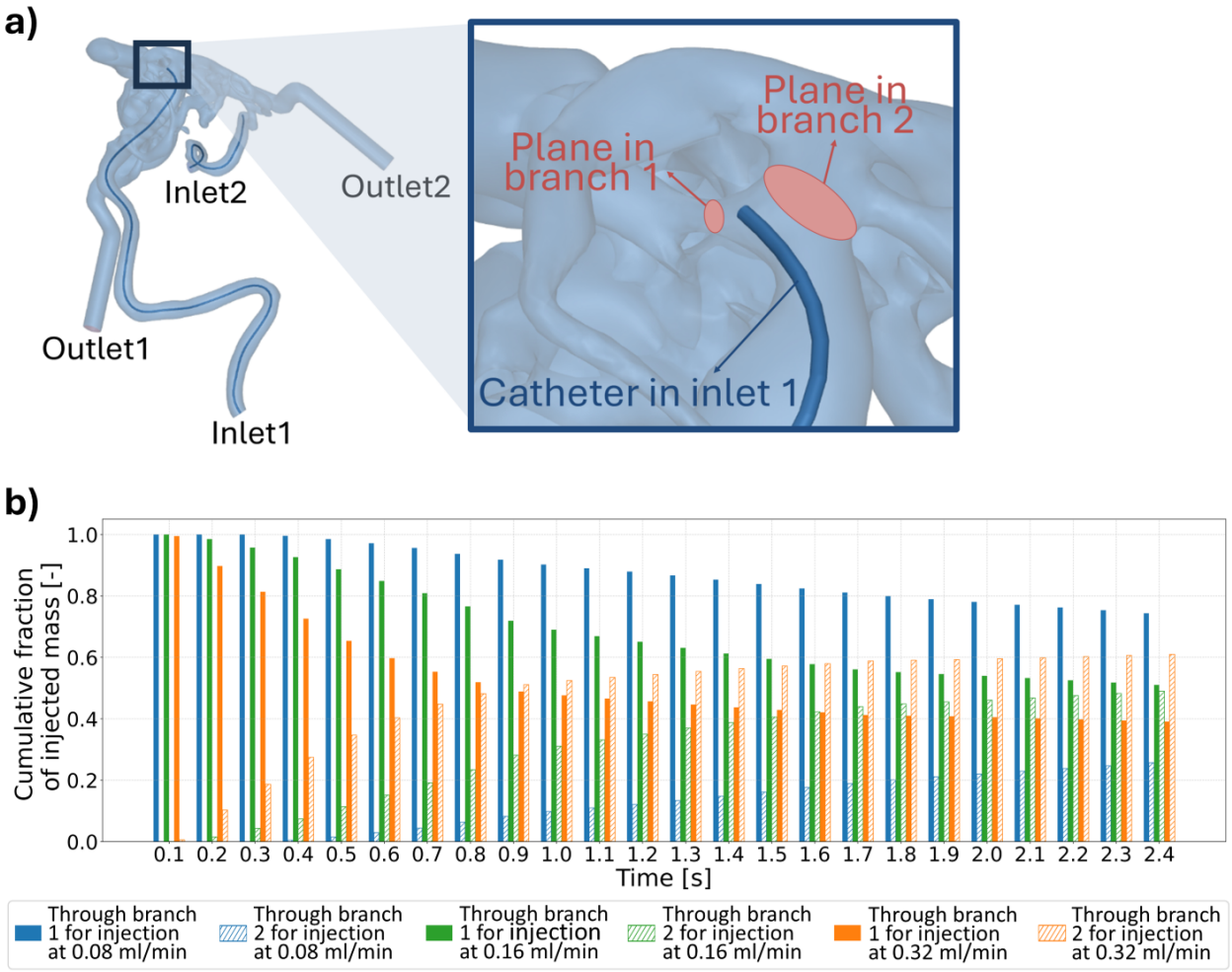

Figure 3.7: a) Indication of the two branches after the injection site and the location of the planes in each branch over which the mass flow rates are calculated. **b)** Cumulative fractions of injected Onyx mass through branches 1 (solid bars) versus 2 (dashed bars) over time for three blood flow cycles (2.40 s in total) for various Onyx injection rates (0.08, 0.16, and 0.32 ml/min in blue, green, and orange, respectively). At each time point, the height of the bar for a specific branch and a specific injection rate represents the fraction of the total injected mass (up to that time and for that injection rate) that has passed through that specific branch.

3.1.3 Local Pressure Differences for Various Injection Rates

Pressure differences over a local zone just downstream of the injection site are investigated for various injection rates. The small zone of approximately 4 mm in length (indicated in Figure 3.8.a), was selected due to the limited simulation time of 2.40 s (covering only three 0.80 s cardiac cycles). A more extensive analysis downstream would ideally require extensively longer simulations, the implementation of Onyx solidification, and improved representation of central nidal vessels (now limited by the imaging resolution) for increased realism. However, it is interesting to look at the initial hemodynamic effects after Onyx injection with various injection rates.

The pressure difference is calculated as the facet-averaged static pressure over plane 1A minus the facet-averaged static pressure over plane 1B (planes depicted in Figure 3.8.a). Figure 3.8.b presents this pressure difference over time for the case before Onyx injection (black) and the cases for various injection rates (0.08, 0.16, and 0.32 ml/min in blue, green, and orange, respectively). Figure 3.8.c shows boxplots for the ratios of the pressure differences for the 0.08 (blue) and 0.16 ml/min (orange) injection rates relative to the pressure difference for the recommended injection rate of 0.16 ml/min (Equation 3.2) over the same zone over 0.80 s time intervals corresponding to either cycle 1, 2, or 3. Also, minimum, mean, and maximum values for each boxplot are indicated, as well as a horizontal dashed green line at the reference ratio of 1.

$$\text{Ratio}_{\text{injection rate x ml/min}} = \frac{\Delta P_{\text{injection rate x ml/min}}}{\Delta P_{\text{injection rate 0.16 ml/min}}} \tag{3.2}$$

With $\text{Ratio}_{\text{injection rate x ml/min}}$ the ratio for the case of injection rate of x ml/min (with x either 0.08 or 0.32 ml/min), $\Delta P_{\text{injection rate x ml/min}}$ the pressure difference over time for x ml/min injection rate (as seen in Figure 3.8.b), and $\Delta P_{\text{injection rate 0.16 ml/min}}$ the pressure difference over time for the recommended 0.16 ml/min injection rate (as seen in green on Figure 3.8.b).

Figure 3.8.b demonstrates that for all Onyx injection cases, the local pressure difference across the zone downstream of the injection site (depicted in Figure 3.8.a) is consistently greater than in the baseline case before Onyx injection. These increased pressure differences can be attributed to the viscous Onyx occupying space in the vessel, which increases blood flow resistance, and thus pressure differences. This can be intuitively understood by Hagen–Poiseuille's law (Equation 1.3) and the hemodynamic analog of Ohm's law (Equation 1.1): as more vis-

cous Onyx is injected into the blood, it raises the local effective viscosity and thus the flow resistance (Equation 1.3); which in turn leads to an increase in pressure difference across the zone (Equation 1.1). While the assumptions of Hagen–Poiseuille's law (i.e. steady, laminar flow of incompressible, Newtonian fluid in a cylindrical tube) are not satisfied in this complex case, the law again offers useful intuitive insight into the observed trends.

Moreover, the pressure difference correlates with the Onyx injection rate: higher injection rates cause higher pressure differences (on Figure 3.8.b the orange curve is consistently above the green and blue ones, and the green curve is consistently above the blue one). This is logical following the reasoning explained earlier, as higher volumetric flow rates introduce more Onyx into the vasculature in a given time, and thus increase the flow resistance more in a given time, leading to even higher pressure differences. However, it is important to note that this observed increase in pressure difference may be attributed to the increased injection rate itself and/or to the greater volume of Onyx introduced over the same time interval. To illustrate the effect of the injection rate parameter, the following comparisons can again be considered:

- Comparison 1: Case for 0.16 ml/min after one cycle (ΔP of 2.57 Pa) versus case for 0.08 ml/min after two cycles (ΔP of 1.51 Pa)
- Comparison 2: Case for 0.32 ml/min after one cycle (ΔP of 5.94 Pa) versus case for 0.16 ml/min after two cycles (ΔP of 2.97 Pa)

For both these comparisons, despite the same total mass of Onyx being delivered in the two compared cases, the cases with the higher injection rate led to higher pressure differences. The injection rate is consequently a key parameter influencing local hemodynamics.

An interesting observation from Figure 3.8.b is that the peaks in the pressure profiles occur slightly earlier for all Onyx injection cases compared to the baseline case with only blood flow. This shift in peak timing is consistent across all injection rates, suggesting that the effect is not dependent on the injection rate, but rather on the presence of Onyx itself. Potentially, this is attributed to changes in local wave dynamics due to Onyx. As viscous Onyx is introduced, the local vascular impedance is altered, which can potentially affect the speed and reflection patterns of pressure waves within the vasculature. These changes in impedance may lead to the earlier arrival of reflected waves, thus shifting the overall pressure waveform slightly forward in time [152–154]. However, wave propagation and reflection phenomena in such complex vascular systems (especially under multi-phase flow conditions) can be very complex, making these dynamics difficult to further interpret.

Figure 3.8.b also shows a visibly damped and less pulsatile pressure waveform over time for the highest injection rate (0.32 ml/min), specifically in the first cardiac cycle, compared to the other cases. This damping is likely due to the growing obstruction imposed by the rapid Onyx injection, leading to a gradually increasing pressure difference, which progressively suppresses flow fluctuations and smooths the pressure difference profile. While a gradual increase in pressure difference over time compared to baseline is also observed for the two lower injection rates, the effect is most pronounced at the highest rate, thus the pulsatility diminishes more noticeably. The phenomenon is most noticeable in cycle 1, as the pressure difference is still building up as the Onyx is being introduced into the vasculature. Over time, the pressure waveforms appear to stabilize somewhat at their higher levels, likely because the rate of change in local resistance due to the injected viscous Onyx becomes less abrupt.

Figure 3.8.c further quantitatively supports the influence of injection rate on pressure differences by presenting the ratios as defined in Equation 3.2 over the three cardiac cycles. For all three cycles, the pressure difference ratio is consistently greater than 1 for the 0.32 ml/min injection rate and less than 1 for the 0.08 ml/min rate. This confirms the earlier observation from Figure 3.8.b that increasing injection rates lead to higher pressure differences due to increased flow resistance. For the 0.32 ml/min case (orange), the ratios over the different cycles seem to be overall slightly below 2, indicating that, for this localized zone and over this limited time period, the pressure differences scale almost proportionally with the Onyx injection rate. Cycle 1 exhibits relatively large variability, with pressure difference ratios ranging from 1.30 to 2.18. This spread can be attributed to the fact that the hemodynamic response is still developing during the initial injection period (the orange graph in Figure 3.8.b increases quite fast over time for the first cycle, as discussed before). Over the three cycles, the average pressure difference ratios slightly decrease from 1.92 in cycle 1 to 1.85 in cycle 2 and 1.78 in cycle 3. This trend reflects that the pressure difference in case of 0.32 ml/min continues to increase over time but less substantially (pressure difference stabilizes over time at an elevated level), and that the pressure difference in the reference 0.16 ml/min case also gradually increases, although less fast and less clearly than in the 0.32 ml/min case. Consequently, the ratio between them shows a mild decline over time for the different cardiac cycles. In contrast, the 0.08 ml/min case (blue) shows overall ratios slightly above 0.50, again indicating that the pressure difference scales almost proportionally with the injection rate. Also in this case, cycle 1 exhibits the largest variability (from 0.47 to 0.87), as the pressure differences are still building up here as the Onyx is just being introduced. The ratios also seem to stabilize over time, as the average ratio equals 0.58 in cycle 2 and 0.60 in

cycle 3, with in both cycles lower variability (0.46 to 0.72 in cycle 2 and 0.50 to 0.75 in cycle 3).

While the trends in pressure differences are clear, the absolute magnitudes for all cases remain relatively small (maximal value of 8.85 Pa for the 0.32 ml/min case). These values are small compared to the typical accuracy of intracranial pressure transducers (in the range of 0.7 to 2.3 mmHg, so 93.3 to 306.6 Pa [155, 156]). The small pressure differences likely stem from the limited length of the zone (around 4 mm) and short simulation time (2.40 s); longer simulations and examinations over larger regions could potentially reveal greater effects as embolization progresses. Incorporation of Onyx solidification would also impact results, especially over extended time scales.

These findings imply that higher Onyx injection rates may lead to more rapid and more substantial increases in local pressure. Consequently, higher injection rates might challenge procedural safety and embolic agent control, as elevated pressure differences in this clinical context can be associated with risks for hemorrhage [114, 157]. The results also show that these pressure differences increase most rapidly during the first cardiac cycle. However, in the simulations, a constant Onyx injection velocity was applied over the entire time period, whereas in the clinic, Onyx is injected manually with a syringe, meaning the injection rate does not instantly reach its maximum value. As a result, the initial increase in local pressure during the first cardiac cycle is likely less abrupt in reality than observed in the simulations. It is important to note that the absolute values of the pressure differences computed in this study remain small (well below the sensitivity thresholds of intracranial pressure transducers [155, 156]). This means that these results are unlikely to have immediate clinical impact; however, the differences between various injection rates are clear, underscoring the potential value of further investigation of the effect of injection rates, particularly in longer simulations that incorporate Onyx solidification for increased realism.

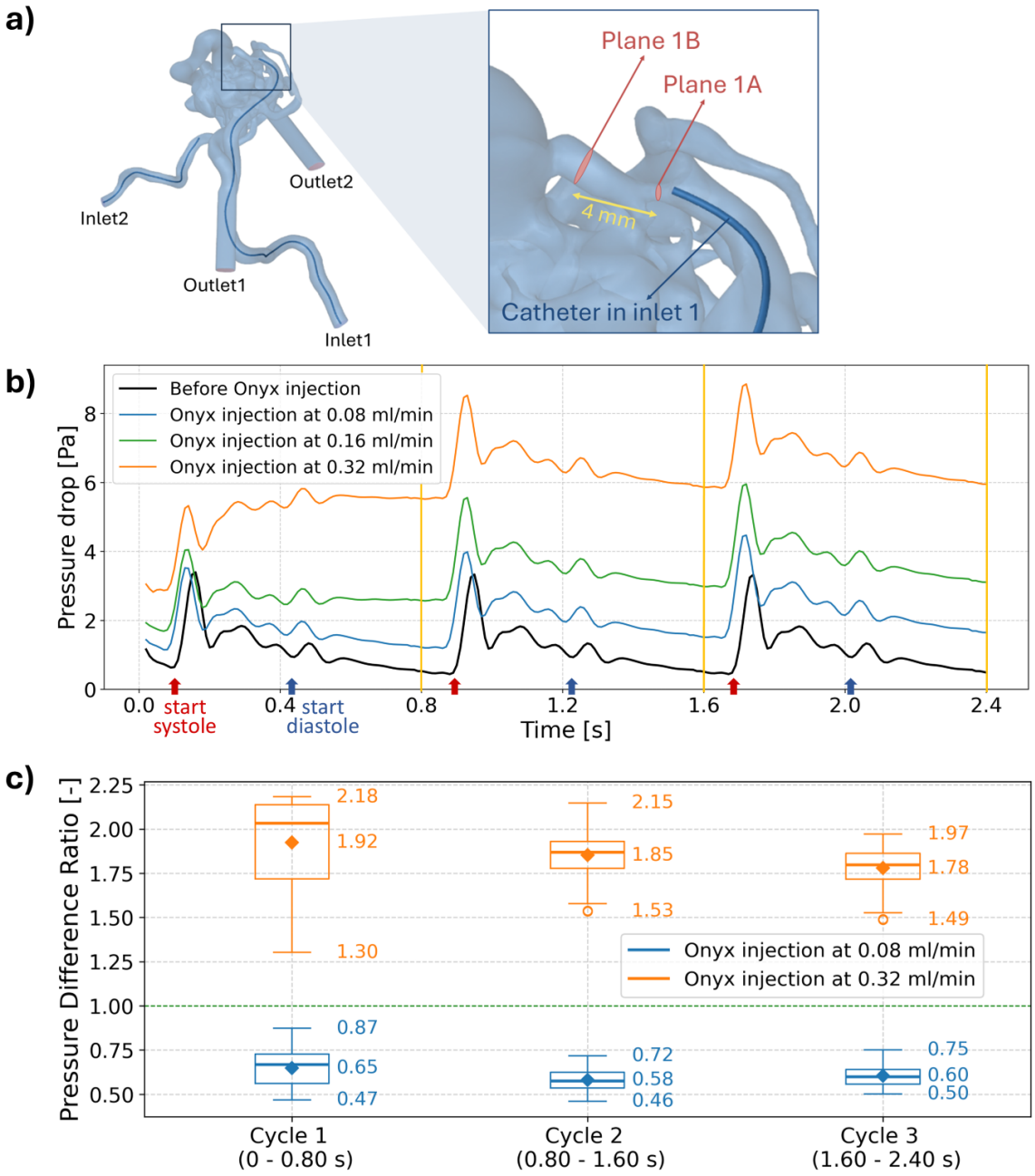

Figure 3.8: a) Two planes downstream of the injection site delimiting the zone over which pressure difference (i.e. facet-averaged static pressure in plane 1A minus plane 1B) is calculated. The yellow arrow indicates a distance of 4 mm. **b)** The pressure difference over zone in panel a) over time for the case before Onyx injection (black) and for various Onyx injection rates: 0.08, 0.16, and 0.32 ml/min (blue, green, and orange, respectively). Yellow vertical lines mark the end of each 0.80 s cardiac cycle, and red and blue arrows on the time-axis mark the start of systole and diastole, respectively. **c)** Boxplots of the pressure difference ratios for injection rates of 0.08 ml/min (blue) and 0.32 ml/min (orange), relative to the recommended rate of 0.16 ml/min (Equation 3.2). Each boxplot shows the distribution of this ratio for a specific injection rate over a 0.80 s interval corresponding to either cycle 1, 2, or 3. Values for the mean, minimum, and maximum are shown to the right of each boxplot. A horizontal dashed green line denotes the reference ratio of 1.

3.1.4 Implications for Clinical Practice

The findings of this study highlight the influence of Onyx injection rate on key hemodynamic parameters, such as spatial Onyx distribution and local pressure differences within the AVM vasculature. These preliminary results suggest that careful monitoring—and perhaps control—of Onyx injection velocity during embolization procedures may enhance both the efficacy and safety of treatment. Specifically, controlling injection rates more carefully may reduce the risk of adverse events such as non-target embolization, suboptimal Onyx distribution, or hemorrhagic complications.

Furthermore, the existence of FDA guidelines around the Onyx injection rate (i.e. recommended injection rate of 0.16 ml/min and upper limit of 0.30 ml/min due to risks for angionecrosis and/or vasospasm observed in animal studies [114]) underscores the clinical relevance of monitoring—and perhaps controlling—the injection velocity in clinical practice to maintain appropriate injection parameters throughout the procedure.

In addition, this study highlights the value of CFD modeling for quantification of embolization procedures and the long-term potential of incorporating CFD modeling into pretreatment planning. With thorough model validation and workflow standardization, CFD simulations could support clinicians in predicting procedural outcomes more reliably and tailoring strategies to patient-specific vascular geometries.

However, further research should explore a broader range of patient-specific geometries, optimized boundary conditions, and experimental validation of simulation results, as further discussed in Sections 3.2 *Limitations* and 3.3 *Future Perspectives*.

3.2 Limitations

While the conducted simulations for this thesis offer valuable insights into the impact of the Onyx injection rate on hemodynamics during endovascular embolization of an AVM, several assumptions and simplifications were necessary due to practical constraints and the complexity of the clinical scenario. Additionally, only one patient-specific AVM was modeled, which limits the generalizability of the results. This section summarizes the most important limitations of this work, some of which have already been touched upon throughout the thesis.

3.2.1 Limitations of Model Reconstruction

Several limitations related to the modeling process of the AVM geometry should be acknowledged. First, the spatial resolution of the 3DRA imaging data was limited by a slice thickness of 0.44 mm, which was insufficient to resolve all fine vascular structures within the AVM nidus (Section 2.1.1 *Data Acquisition*). Although representing the nidus with a porous media approach could provide a more accurate approximation [7, 8, 120], this was beyond the scope of this study. Furthermore, no catheter thickness was assigned in the model, which may have influenced local flow dynamics (Section 2.1.4 *Introducing Catheters into the Model*). Finally, the reconstructed geometry never perfectly reflects the in vivo anatomical conditions due to inevitable simplifications during segmentation and meshing (Section 2.1.1 *Data Acquisition*).

3.2.2 Assumptions of Boundary Conditions

Furthermore, boundary conditions (as described in Section 2.2.3 *Boundary Conditions*) inevitably simplify reality, despite efforts to approximate physiological realism.

First, the actual Onyx injection velocity during the intervention was unknown due to the absence of imaging frame rate data. Therefore, simulations relied on the FDA-recommended injection rate, along with values at half and double that rate (Section 2.2.3.2 *Velocity Inlet Boundary Conditions for Onyx*). Although it would be interesting to simulate with the actual injection rate, this approach provided a reasonable basis for comparison of various injection rates.

Secondly, patient-specific blood velocity profiles at the arterial feeders could not be determined, as no dynamic imaging modalities such as Doppler ultrasound or phase contrast MRI were performed [8]. Therefore, representative flow profiles from literature were used (Section 2.2.3.1 *Velocity Inlet Boundary Conditions for Blood*). Moreover, it was not possible

to scale these profiles to a patient-specific velocity value based on DSA data due to the lack of imaging frame rate data for this patient.

Thirdly, fixed pressure boundary conditions were applied at the outlets (Section 2.2.3.4 *Pressure Boundary Conditions*), although time-varying pressure profiles or flow distribution profiles would be more realistic. Remark that an alternative multi-phase modeling approach would need to be explored for flow distribution boundary conditions, as these are not compatible with the VOF model [135].

Lastly, the vessel walls were modeled as rigid (Section 2.2.3.3 *Vessel Wall Boundary Conditions*). Although this is a common simplification in CFD modeling, incorporating FSI would lead to more accurate results (mainly for the WSS), and would be an interesting direction for future work [126, 127] (see some preliminary results in Section 3.3.2 *Wall Shear Stress Analysis: Preliminary Observations and Future Work*.

Some ideas to further improve boundary conditions in future work are stated in Section 3.3.1 *Personalized Boundary Conditions*.

3.2.3 Assumptions in the Simulation Setup

In addition to the boundary conditions, several other assumptions were made in the simulation setup. The effect of gravity was neglected, and blood was assumed to have a constant viscosity of 0.004 kg/(m·s), although non-Newtonian behavior may be relevant in small vessels (with diameters around 0.05 to 0.15 mm), like in the nidus [120, 121]. Furthermore, laminar flow was assumed, which was deemed reasonable due to sufficiently low Reynolds numbers and based on literature [8, 107]. Incompressibility was assumed and deemed acceptable given the relatively low velocities (Section 2.2.2 *Simulation Setup*) [136, 137].

The VOF model was used to simulate blood and Onyx as immiscible phases (detailed in Section 2.2.1 *Multi-phase flow: Volume-of-Fluid method*). However, the model comes with several assumptions and limitations. The VOF approach assumes a single shared velocity field across all phases, which makes extracting phase-specific velocities infeasible and thus limits post-processing analysis of individual fluid behavior [135]. Additionally, the model does not support outflow fraction boundary conditions, so pressure outlets (based on a single-flow simulation with the patient-specific outflow fractions) were used. However, it would be interesting to apply outflow fractions, as these can be derived from DSA imaging, and using these directly (without transforming these to pressure outlets) would keep the boundary conditions as close to reality as possible. In future work, it could be interesting to explore other settings to determine the most optimal ones through experimental validation (see also

Section 3.3.5 *Validation Through Experimental and Clinical Studies*).

3.2.4 Scope Limited to a Single Case

The current results are based on a single patient-specific geometry, which limits the ability to draw general conclusions about the influence of the injection rate on Onyx behavior. To generalize the findings of this thesis, it is essential to investigate a larger number of AVM cases (see Section 3.3.3 *Expansion of patient cohort*).

3.2.5 Simplifications in Onyx Modeling

The modeling approach used for Onyx in this study involves simplifications that limit the physiological realism of the simulations. First of all, Onyx-18 was treated as a single-phase material with averaged properties, although its two constituents, DMSO and EVOH, should ideally be represented as two separate phases (see Table 2.3 from Section 2.2.2 *Simulation Setup*). Additionally, one of the most significant limitations of this study is the omission of the Onyx solidification process, which plays a critical role in the embolization behavior. Incorporating solidification would enhance both the realism and predictive capability of the simulations [7, 8, 107]. This challenge is further discussed in Section 3.3.4 *Modeling the Onyx Solidification Process*. However, the results of this study remain interesting to assess the initial effect of Onyx injection on the hemodynamics.

3.3 Future Perspectives

Several key directions for future research emerge from the findings and limitations of this study (see Sections 3.1 *Results and Interpretation* and 3.2 *Limitations*). This section outlines the most critical areas for advancement: improving patient-specific boundary conditions, analyzing WSS, examining multiple AVM cases, incorporating Onyx solidification, and experimental validation of simulations. In the long term, also the feasibility of monitoring or controlling injection rates in the clinic and research for enhanced workflow efficiency would need to be considered.

3.3.1 Personalized Boundary Conditions

An interesting advancement is the optimization and personalization of boundary conditions, which could greatly enhance model fidelity but also the translational potential of CFD in patient-specific clinical decision-making.

One promising technique is 4D flow MRI, which provides time-resolved, three-dimensional velocity data throughout the cardiac cycle. This modality enables non-invasive measurements of blood flow in the vasculature, offering detailed insights into inflow and outflow profiles that could be directly applied as boundary conditions in CFD models [8, 158–160].

In addition, DSA imaging—which is already routinely used during AVM embolization—can be used for determining personalized velocity values. For the patient studied in this thesis, DSA images were also available; however, the imaging frame rate data was missing, which prevented extraction of velocity information. Although DSA is primarily a qualitative imaging modality, quantitative methods have been developed to extract velocity information from DSA sequences. These techniques rely on contrast bolus tracking and temporal analysis of pixel intensity changes to estimate mean velocities (so imaging frame rate data is needed) [161]. Although flow or velocity profiles over time cannot be obtained this way, the information from patient-specific preinterventional DSA images can be valuable for approximating personalized mean velocities in the feeding arteries or draining veins of the AVMs.

Furthermore, the assumption of rigid walls could be improved upon by implementing FSI to model a more realistic non-rigid wall that is deformed by the forces exerted on it by the fluid flow in the model, although this is computationally expensive [126, 127].

3.3.2 Wall Shear Stress Analysis: Preliminary Observations and Future Work

Although WSS investigation was not a primary focus of this study, preliminary results of WSS for various injection rates are presented in this section, given the clinical relevance of WSS, as elevated values have been associated with risks such as thrombus formation or vessel rupture [125]. The CFD simulations in this thesis allow for WSS examination; however, it is important to interpret these results with appropriate caution. CFD in general tends to overestimate WSS, as it assumes rigid vessel walls, whereas more realistic results would be obtained using FSI models [126, 127]. In this study, however, we applied physiological inlet velocity profiles derived from healthy individuals (see Section 2.2.3.1 *Velocity Inlet Boundary Conditions for Blood*) in an AVM geometry (with enlarged arteries); while in reality, AVMs often exhibit significantly elevated velocities, potentially up to 160 % higher than normal [143], which implies that WSS values reported here are likely underestimated. So, the exact values for WSS presented in this section should not be overinterpreted.

Figure 3.9 illustrates the WSS over the vessel wall around the injection site over time for various injection rates. In all cases, an increase in WSS is seen around the location of the catheter due to Onyx injection. This increase in WSS can be attributed to the locally elevated viscosity near the wall at the injection site caused by the presence of Onyx—which has a significantly higher dynamic viscosity than blood (0.018 vs. 0.004 kg/(m·s), respectively)—as described by the WSS formula (Equation 3.3) [162].

Formula for wall shear stress:

$$\tau_w = \mu \left(\frac{\partial u}{\partial n} \right) \tag{3.3}$$

With τ_w the wall shear stress [Pa], μ the dynamic viscosity [kg/(m·s)], $\frac{\partial u}{\partial n}$ the shear rate or the velocity gradient perpendicular to the wall [s^{-1}] with u the velocity component tangential to the wall, and n the direction normal to the wall.

Differences between various injection rates can be observed: higher Onyx injection rates appear to cause higher local WSS around the injection site. For the zone of the outer vessel wall that is visualized in these figures, the maximal WSS values are around 2, 5, and 8 Pa (determined with an accuracy of 1 Pa) for injection rates of 0.08, 0.16, and 0.32 ml/min, respectively. However, as previously noted, the absolute WSS values are likely not realistic due to limitations in the simulation setup. Moreover, for a given injection rate, the WSS

values remain unchanged over the entire time period, at least considering this accuracy of 1 Pa. Since WSS is expected to increase with rising blood inlet velocities [163, 164], more accurate investigations could potentially capture such temporal variations. A potential explanation for the absence of observable fluctuations in WSS for the current simulations might be that the effect of the Onyx—which is injected with a constant velocity during the simulations—overrides the expected influence of pulsatile blood inlet velocity profiles.

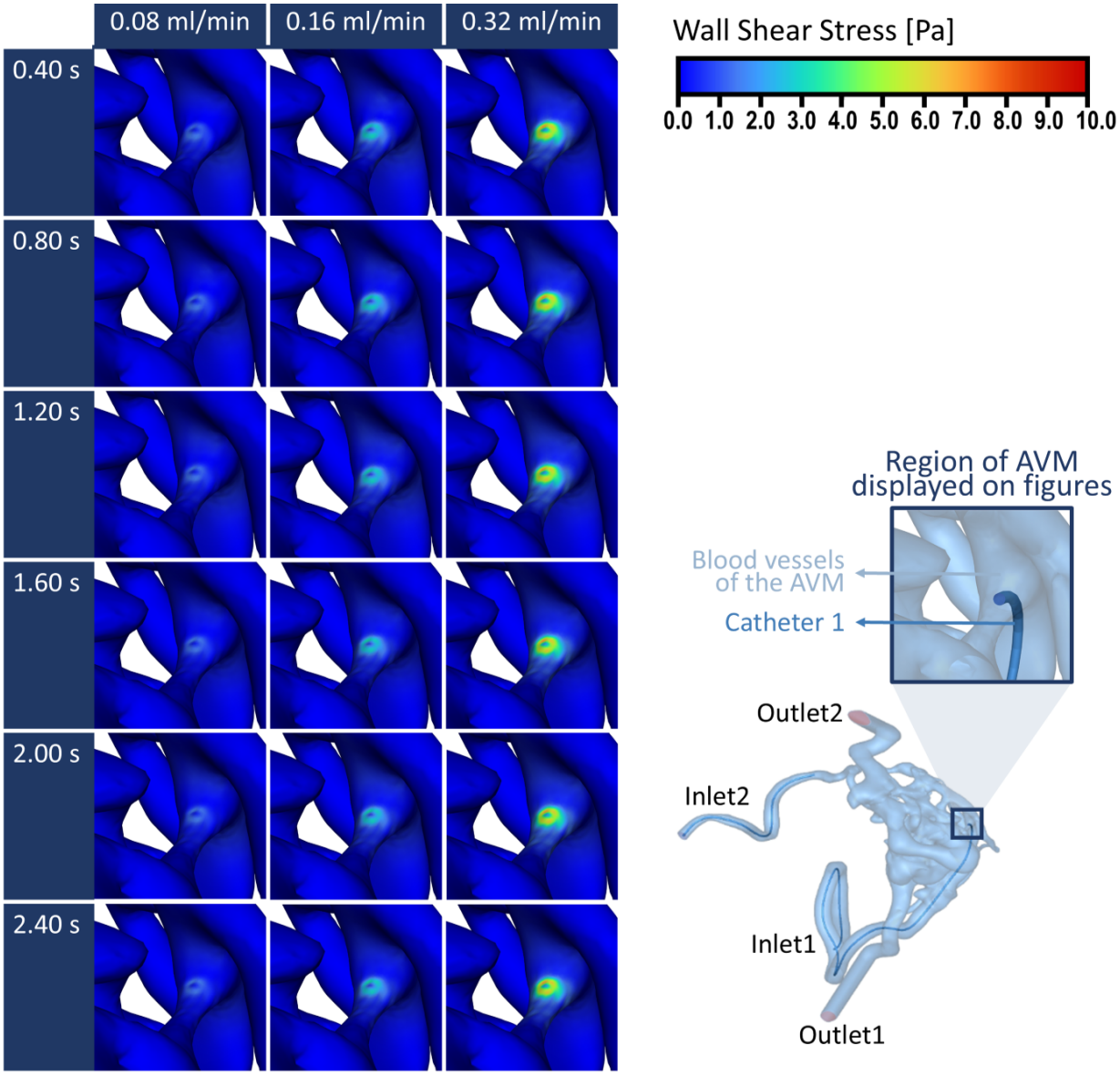

Figure 3.9: The WSS on the outer vessel walls of the AVM around the injection site over time for various injection rates (0.08, 0.16, and 0.32 ml/min). The WSS is indicated by a color scale from deep blue for 0.0 Pa to dark red for 10.0 Pa (legend for all figures is shown on the upper right). On the bottom right, the zone of the AVM depicted in the pictures in the table is shown.

In conclusion, these preliminary findings indicate that further investigation of the Onyx injection rate effect on WSS is clinically interesting, since the injection rate is seen to have an influence on the WSS for these simulations, and excessively high WSS is associated with risks of thrombus formation and vessel rupture [125]. However, boundary conditions would need to be optimized and personalized (i.e. FSI to model deformable walls and patient-specific blood inlet velocity boundary conditions) to obtain more reliable WSS results.

3.3.3 Expansion of patient cohort

To evaluate whether the findings presented in this thesis are generalizable, a larger number of AVM cases should be modeled. Studying a wider range of AVM geometries and flow conditions will help determine the robustness of observed trends and identify potential case-dependent variations. Expanding the patient cohort is a crucial step towards building clinically relevant and reliable CFD tools. Ideally, multiple patient-specific simulations would also be experimentally validated (as discussed in Section 3.3.5 *Validation Through Experimental and Clinical Studies*).

3.3.4 Modeling the Onyx Solidification Process

An important improvement for future research is the incorporation of the Onyx solidification process, which is critical for improving the realism and clinical relevance of embolization simulations [7,8,107,120]. Solidification significantly influences the behavior of the embolic agent and local hemodynamics; however, it was not included in this study due to time constraints, as simulating the typical five-minute solidification period of Onyx [114] would require substantial computational resources and time. Moreover, the primary focus of this study was on the initial effects of different Onyx injection rates on the hemodynamic environment and the spatial distribution of the embolic agent. Ideally, future models should distinguish between the two phases of Onyx (EVOH and DMSO), with the viscosity increasing exponentially with the decrease in DMSO concentration, as suggested in prior studies [7,8]. However, additional experimental validation of the material characteristics of Onyx (i.e. relationship of viscosity increase as a function of DMSO content decrease) may be required.

3.3.5 Validation Through Experimental and Clinical Studies

Extensive validation will be essential for translating CFD modeling into clinical applications. Different modeling and simulation methods should be investigated (e.g. different multi-phase

flow models, boundary conditions, and other settings) in order to determine an optimal workflow for AVM modeling. Validation requires in vitro experiments using 3D-printed phantoms of various patient-specific AVMs, and ultimately, clinical trials will be necessary to assess the reliability and added clinical value of CFD-based tools in guiding treatment planning [58, 123].

3.3.6 Monitoring or Controlling Injection Rate

If further research demonstrates the clinical need for monitoring or perhaps controlling the velocity of Onyx injections, it would be important to explore the development of specialized pumping devices or safety alert systems. Such systems could enable real-time monitoring to detect when the injection rate exceeds the FDA upper limit of 0.30 ml/min [114], with, for instance, an alerting alarm sound. Additionally, if CFD modeling were to be used as a pretreatment tool in the long term, monitoring injection velocity would be necessary to follow a previously defined treatment plan. Possibly, semi-automated injection devices could be interesting to administer the embolic agent at an optimized speed, although the clinician should have the ability to override the system manually at any time to ensure patient safety. Injection systems like these are already explored in other clinical settings: for example, Ren et al. (2022) demonstrated robotic-assisted embolic agent delivery in the renal artery-kidney system of rabbits [128], highlighting the feasibility of controlled injection in complex vascular procedures.

3.3.7 Optimizing Workflow Efficiency

Looking further ahead, substantial advancements in workflow speed and automation are essential, particularly in the segmentation process, to integrate CFD simulations into the clinical routine. Leveraging segmentations generated and used during clinical interventions—such as those routinely created at UZ Ghent (University Hospital, Ghent, Belgium)—could be valuable, particularly for retrospective CFD modeling studies of AVMs. After thorough validation of these CFD models, standardized protocols could be developed. In the long term, for CFD to be used as a pretreatment tool, alternative approaches are needed. AI-based segmentation holds significant potential, as it can significantly reduce manual effort and inter-operator variability. Several studies have already explored using AI frameworks to segment blood vessels from DSA or 3DRA images [165–167]. While these techniques are expected to improve significantly in the near future, it is crucial to ensure adequate validation and understanding of these models, as careful application of AI in healthcare is essential.

Chapter 4

Conclusion

Cerebral arteriovenous malformations (AVMs) are abnormal, direct vascular connections between arteries and veins that bypass the normal capillary beds, creating high-flow, low-resistance shunts that may result in severe clinical complications such as hemorrhage. Endovascular embolization is a common treatment, involving the injection of an embolic agent, such as Onyx, to occlude the AVM and create a safer hemodynamic situation. As the outcomes of this procedure greatly rely on the experience of the clinician, there is growing interest in quantification of key parameters that influence the outcome, for example with computational fluid dynamics. This thesis specifically investigated the impact of Onyx injection rate through multi-phase flow simulations with the Volume-of-Fluid method. The simulations were performed on a patient-specific AVM geometry, segmented from 3D rotational angiography images, with boundary conditions based on both literature and digital subtraction angiography data. Three different injection rates were evaluated: 0.08 ml/min, 0.16 ml/min (the FDA-recommended rate for Onyx injection), and 0.32 ml/min. The results show that the injection rate affects the behavior of the embolic agent. Higher injection rates accelerate Onyx progression and alter its spatial distribution over different downstream branches. Additionally, faster injection rates caused greater pressure differences downstream of the injection site, and greater wall shear stresses around the injection site. These changes might impact procedural outcomes, suggesting that Onyx injection rate is a clinically relevant parameter that deserves closer consideration, and the impact of deviating from the recommended injection rate is interesting to explore further. However, it is important to emphasize that this study represents an initial investigation based on a single patient case and simplified modeling assumptions. To confirm and generalize these findings, further research with a larger patient cohort, an optimized simulation workflow, and experimental validation, is necessary.

Chapter 5

Societal Reflection

This chapter provides a societal reflection on the broader implications of this thesis work, exploring how personalized CFD modeling for endovascular embolization of AVMs could impact society in both the near and long term. Ethical considerations related to the use of patient data are addressed, alongside societal impacts framed within the context of the Sustainable Development Goals (SDGs) [168].

This research makes use of imaging data of patients, which means careful consideration of ethical and privacy aspects—such as anonymization, informed consent, and data protection—is critical. All data were fully pseudo-anonymized, and ethical approval was obtained from the Ethics Committee of UZ Gent (reference: ONZ-2024-0129, approval letter added in Appendix E: *Approval Letter from Ethics Committee*). In addition, the study was registered on ClinicalTrials.gov (reference: NCT06588543), in accordance with international standards for clinical research.

While these measures ensure patient privacy and compliance with ethical regulations, the use of real-world clinical data in computational modeling also raises broader ethical questions. Although CFD simulations hold great promise in the long term to aid in personalized pretreatment planning, they must always be combined with clinical expertise and critical thinking. It is important to acknowledge limitations of the model itself and think about how misuse or misinterpretation can be prevented, especially when (in the long term) clinical decisions could be influenced by these simulations and suboptimal decisions could harm the patient. Thus, transparency about model assumptions and constraints, thorough validation of models and simulation methodologies, and close collaboration between engineers and clinicians are essential to ensure that computational modeling is used in a safe, responsible, and ethical manner.

The potential integration (in the long term) of CFD modeling into clinical practice for pre-treatment planning of endovascular embolizations also raises important societal considerations. This kind of modeling can contribute to SDG 3: 'Good Health and Well-being', particularly through improved planning of procedures. Personalized simulations help to minimize trial-and-error during procedures, reduce complication risks and procedural time, and optimize outcomes. However, clinical expertise should remain central to decision-making, and limitations (as for this study discussed in Section 3.2 *Limitations*) should be considered.

While advanced CFD modeling holds great promise for improving AVM treatment, it is worth thinking about its accessibility across different hospitals and countries in relation to SDG 10: 'Reduced Inequalities'. Innovations like this might increase the gap between high-resource and low-resource settings. Potentially, open-source tools, along with transparent reporting and dissemination of simulation workflows and methodologies, could help promote more equitable access to these technologies.

In the context of SDG 9: 'Industry, Innovation and Infrastructure', the integration of advanced CFD modeling for AVM treatment can lead to more efficient procedures, resulting in fewer complications and shorter hospital stays, resulting in cost savings and alleviation of strain on healthcare systems, promoting long-term sustainability.

In summary, while this thesis illustrates the promising potential of personalized CFD modeling for AVM treatment, its integration into clinical practice requires attention to ethical, societal, and infrastructural aspects. Protecting patient rights, clinical validation of the models, and focusing on interdisciplinary collaboration will be key to ensure that this innovation will lead to sustainable healthcare improvements.

Bibliography

[1] A. H. Care, "Arteriovenous malformation (avm)," n.d. [Online]. Available: https://www.aurorahealthcare.org/services/neuroscience/brain-skull-base-care/cerebrovascular-malformations/arteriovenous-malformation

[2] D. Menken, "Cerebral avm resection surgery - designer biomed - medical illustration," https://www.medillsb.com/illustration_image_details.aspx?AID=11565&IID=226266, 2024, accessed: 2025-02-18.

[3] Mayo Clinic Staff, "Brain stereotactic radiosurgery," 2023, accessed: 2025-02-18. [Online]. Available: https://www.mayoclinic.org/tests-procedures/brain-stereotactic-radiosurgery/about/pac-20384679

[4] M. Pinkiewicz, M. Pinkiewicz, J. Walecki, and M. Zawadzki, "State of the art in the role of endovascular embolization in the management of brain arteriovenous malformations—a systematic review," 12 2022.

[5] D. F. Vollherbst, R. Chapot, M. Bendszus, and M. A. Möhlenbruch, "Glue, onyx, squid or phil? liquid embolic agents for the embolization of cerebral arteriovenous malformations and dural arteriovenous fistulas," pp. 25–38, 3 2022.

[6] P. M. Meyers, J. T. Fifi, K. M. Cockroft, T. R. Miller, C. A. Given, A. R. Zomorodi, B. D. Jagadeesan, M. Mokin, P. Kan, T. L. Yao, O. Diaz, D. Huddle, R. J. Bellon, J. Seinfeld, A. J. Polifka, D. Fiorella, R. V. Chitale, P. Kvamme, J. T. Morrow, J. Singer, A. K. Wakhloo, A. S. Puri, V. R. Deshmukh, R. A. Hanel, L. F. Gonzalez, H. H. Woo, and M. A. Aziz-Sultan, "Safety of the apollo onyx delivery microcatheter for embolization of brain arteriovenous malformations: Results from a prospective post-market study," *Journal of NeuroInterventional Surgery*, vol. 13, pp. 935–941, 2021.

[7] P. Orlowski, P. Summers, J. A. Noble, J. Byrne, and Y. Ventikos, "Computational modelling for the embolization of brain arteriovenous malformations," *Medical Engineering and Physics*, vol. 34, pp. 873–881, 9 2012.

[8] B. Zhang, X. Chen, X. Zhang, G. Ding, L. Ge, and S. Wang, "Computational modeling and simulation for endovascular embolization of cerebral arteriovenous malformations with liquid embolic agents," *Acta Mechanica Sinica/Lixue Xuebao*, vol. 40, 1 2024.

[9] P. Reymond, F. Merenda, F. Perren, D. Rüfenacht, and N. Stergiopulos, "Validation of a one-dimensional model of the systemic arterial tree," *American Journal of Physiology - Heart and Circulatory Physiology*, vol. 297, 7 2009.

[10] A. Can, B. A. Gross, and R. Du, *The natural history of cerebral arteriovenous malformations*. Elsevier, 2017.

[11] M. T. Lawton, W. C. Rutledge, H. Kim, C. Stapf, K. J. Whitehead, D. Y. Li, T. Krings, K. TerBrugge, D. Kondziolka, M. K. Morgan, K. Moon, and R. F. Spetzler, "Brain arteriovenous malformations," *Nature Reviews Disease Primers*, vol. 1, 5 2015.

[12] C. C. McCuaig, "Update on classification and diagnosis of vascular malformations," pp. 448–454, 8 2017.

[13] F. H. Tomlinson, D. A. Rufenacht, T. M. Sundt, D. A. Nichols, and N. C. Fode, "Arteriovenous fistulas of the brain and the spinal cord," *Journal of Neurosurgery*, vol. 79, pp. 16–27, 1993.

[14] N. Goettel, M. Rovira, and S. Bengali, *Arteriovenous malformations*. Elsevier, 1 2024, pp. 333–344.

[15] F. Toulgoat and P. Lasjaunias, *Vascular malformations of the brain*. Elsevier B.V., 2013, vol. 112, pp. 1043–1051.

[16] R. Chapot, P. Stracke, A. Velasco, H. Nordmeyer, M. Heddier, M. Stauder, P. Schooss, and P. J. Mosimann, "The pressure cooker technique for the treatment of brain avms," *Journal of Neuroradiology*, vol. 41, pp. 87–91, 3 2014.

[17] O. Diaz and R. Scranton, *Endovascular treatment of arteriovenous malformations*. Elsevier B.V., 12 2016, vol. 136, pp. 1311–1317.

[18] A. Mansur and I. Radovanovic, "Vascular malformations: An overview of their molecular pathways, detection of mutational profiles and subsequent targets for drug therapy." *Frontiers in neurology*, vol. 14, p. 1099328, 2023.

[19] A. Laakso and J. Hernesniemi, "Arteriovenous malformations: Epidemiology and clinical presentation," pp. 1–6, 1 2012.

[20] M. F. Berman, R. R. Sciacca, J. Pile-Spellman, C. Stapf, E. S. C. Jr., J. P. Mohr, and W. L. Young, "The epidemiology of brain arteriovenous malformations," *Neurosurgery*, vol. 47, no. 2, pp. 389–397, aug 2000.

[21] C. Stapf, H. Mast, R. R. Sciacca, A. Berenstein, P. K. Nelson, Y. P. Gobin, J. Pile-Spellman, and J. P. Mohr, "The new york islands avm study: design, study progress, and initial results." *Stroke; a journal of cerebral circulation*, vol. 34, 2003.

[22] R. Al-Shahi, J. J. Bhattacharya, D. G. Currie, V. Papanastassiou, V. Ritchie, R. C. Roberts, R. J. Sellar, and C. P. Warlow, "Prospective, population-based detection of intracranial vascular malformations in adults: The scottish intracranial vascular malformation study (sivms)," *Stroke*, vol. 34, pp. 1163–1169, 5 2003.

[23] M. R. Bokhari and S. R. A. Bokhari, *Arteriovenous Malformation of the Brain.* Treasure Island (FL): StatPearls Publishing, 2023, statPearls [Internet]. [Online]. Available: https://www.ncbi.nlm.nih.gov/books/NBK430744/

[24] W. Guest and T. Krings, "Brain arteriovenous malformations: The role of imaging in treatment planning and monitoring response," pp. 205–222, 5 2021.

[25] C. Stapf, D. L. Labovitz, R. R. Sciacca, H. Mast, J. P. Mohr, and R. L. Sacco, "Incidence of adult brain arteriovenous malformation hemorrhage in a prospective population-based stroke survey," *Cerebrovascular Diseases*, vol. 13, pp. 43–46, 2002.

[26] J. W. Osbun, M. R. Reynolds, and D. L. Barrow, *Arteriovenous malformations: epidemiology, clinical presentation, and diagnostic evaluation.* Elsevier B.V., 2017, vol. 143, pp. 25–29.

[27] P. M. Crawford, C. R. West, D. W. Chadwick, and M. D. Shaw, "Arteriovenous malformations of the brain: Natural history in unoperated patients," *Journal of Neurology Neurosurgery and Psychiatry*, vol. 49, pp. 1–10, 1986.

[28] R. D. Brown, D. O. Wiebers, G. Forbes, W. M. O'Fallon, D. G. Piepgras, W. R. Marsh, and R. J. Maciunas, "The natural history of unruptured intracranial arteriovenous malformations," *Journal of Neurosurgery*, vol. 68, pp. 352–357, 1988.

[29] S. L. Ondra, H. Troupp, E. D. George, and K. Schwab, "The natural history of symptomatic arteriovenous malformations of the brain: A 24-year follow-up assessment," *Journal of Neurosurgery*, vol. 73, pp. 387–391, 1990.

[30] M. B. Potts, W. L. Young, and M. T. Lawton, "Deep arteriovenous malformations in the basal ganglia, thalamus, and insula: Microsurgical management, techniques, and results," *Neurosurgery*, vol. 73, pp. 417–429, 9 2013.

[31] Y. Weerakkody and F. Gaillard, *Spetzler-Martin arteriovenous malformation grading system.* Radiopaedia.org, 5 2008.

[32] W. L. Young, "Reporting terminology for brain arteriovenous malformation clinical and radiographic features for use in clinical trials," pp. 1430–1442, 2001.

[33] D. Strozyk, R. G. Nogueira, and S. D. Lavine, "Endovascular treatment of intracranial arteriovenous malformation," pp. 399–418, 10 2009.

[34] J. L. Martinez and R. L. Macdonald, "Surgical strategies for acutely ruptured arteriovenous malformations," *Frontiers of Neurology and Neuroscience*, vol. 37, pp. 166–181, 2015.

[35] A. Zafar, B. Fiani, H. Hadi, M. Arshad, A. Cathel, M. Naeem, M. S. Parsons, M. Farooqui, A. A. Bucklin, M. J. Leone, A. Baig, and S. A. Quadri, "Cerebral vascular malformations and their imaging modalities," pp. 2407–2421, 9 2020.

[36] B. A. Gross and R. Du, "Rate of re-bleeding of arteriovenous malformations in the first year after rupture," *Journal of Clinical Neuroscience*, vol. 19, pp. 1087–1088, 2012.

[37] J. C. Horton, W. A. Chambers, S. L. Lyons, R. D. Adams, and R. N. Kjellberg, "Pregnancy and the risk of hemorrhage from cerebral arteriovenous malformations," *Neurosurgery*, vol. 27, pp. 867–872, 1990.

[38] J. L. Porras, W. Yang, E. Philadelphia, J. Law, T. Garzon-Muvdi, J. M. Caplan, G. P. Colby, A. L. Coon, R. J. Tamargo, and J. Huang, "Hemorrhage risk of brain arteriovenous malformations during pregnancy and puerperium in a north american cohort," *Stroke*, vol. 48, pp. 1507–1513, 6 2017.

[39] J. A. Hernesniemi, R. Dashti, S. Juvela, K. Väärt, M. Niemelä, and A. Laakso, "Natural history of brain arteriovenous malformations: A long-term follow-up study of risk of hemorrhage in 238 patients," *Neurosurgery*, vol. 63, pp. 823–829, 11 2008.

[40] L. D. Costa, M. C. Wallace, K. G. T. Brugge, C. O'Kelly, R. A. Willinsky, and M. Tymianski, "The natural history and predictive features of hemorrhage from brain arteriovenous malformations," *Stroke*, vol. 40, pp. 100–105, 1 2009.

[41] S. Liu, H. X. Chen, Q. Mao, C. You, and J. G. Xu, "Factors associated with seizure occurrence and long-term seizure control in pediatric brain arteriovenous malformation: A retrospective analysis of 89 patients," *BMC Neurology*, vol. 15, 8 2015.

[42] J. M. Boone and C. H. McCollough, "Computed tomography turns 50," *Physics Today*, vol. 74, no. 9, pp. 34–40, 2021. [Online]. Available: https://pubs.aip.org/physicstoday/article/74/9/34/928331/Computed-tomography-turns-50Modern-high

[43] SUNY Upstate Medical University, "Image reconstruction," SUNY Upstate Medical University, 2025. [Online]. Available: https://www.upstate.edu/radiology/education/rsna/ct/reconstruction.php

[44] M. Vella, M. D. Alexander, M. C. Mabray, D. L. Cooke, M. R. Amans, C. M. Glastonbury, H. Kim, M. W. Wilson, D. E. Langston, M. B. Conrad, and S. W. Hetts, "Comparison of mri, mra, and dsa for detection of cerebral arteriovenous malformations in hereditary hemorrhagic telangiectasia," *American Journal of Neuroradiology*, vol. 41, pp. 969–975, 5 2020.

[45] G. Lloyd-Jones, "Mri signal production," Radiology Masterclass, 2017, [Online; accessed 21-May-2025]. [Online]. Available: https://www.radiologymasterclass.co.uk/tutorials/mri/mri_signal

[46] C. S. Albin and S. F. Zafar, *VENOUS SINUS THROMBOSIS*. Springer International Publishing, 1 2022, pp. 117–121.

[47] NHS, "Angiography," NHS, 2023. [Online]. Available: https://www.nhs.uk/conditions/angiography/

[48] T. J. Kaufmann and D. F. Kallmes, "Diagnostic cerebral angiography: Archaic and complication-prone or here to stay for another 80 years?" pp. 1435–1437, 6 2008.

[49] R.Bouezzeddine, "Digital subtraction angiography and ct angiography." [Online]. Available: https://www.medical-professionals.com/en/digital-subtraction-angiography-and-ct-angiography/

[50] H. Ota, K. Takase, H. Rikimaru, M. Tsuboi, T. Yamada, A. Sato, S. Higano, T. Ishibashi, and S. Takahashi, "Quantitative vascular measurements in arterial occlusive disease," *Radiographics*, vol. 25, pp. 1141–1158, 9 2005.

[51] C. S. Eddleman, H. J. Jeong, M. C. Hurley, S. Zuehlsdorff, G. Dabus, C. G. Getch, H. H. Batjer, B. R. Bendok, and T. J. Carroll, "4d radial acquisition contrast-enhanced mr angiography and intracranial arteriovenous malformations: Quickly approaching digital subtraction angiography," *Stroke*, vol. 40, pp. 2749–2753, 8 2009.

[52] S. F. Shakur, S. Amin-Hanjani, H. Mostafa, F. T. Charbel, and A. Alaraj, "Hemodynamic characteristics of cerebral arteriovenous malformation feeder vessels with and without aneurysms," *Stroke*, vol. 46, pp. 1997–1999, 7 2015.

[53] S. F. Shakur, T. Valyi-Nagy, S. Amin-Hanjani, L. Ya'Qoub, V. A. Aletich, F. T. Charbel, and A. Alaraj, "Effects of nidus microarchitecture on cerebral arteriovenous malformation hemodynamics," *Journal of Clinical Neuroscience*, vol. 26, pp. 70–74, 4 2016.

[54] S. M. Sargent, S. K. Bonney, Y. Li, S. Stamenkovic, M. M. Takeno, V. Coelho-Santos, and A. Y. Shih, "Endothelial structure contributes to heterogeneity in brain capillary diameter." *Vascular biology (Bristol, England)*, vol. 5, 1 2023.

[55] Klabunde, Richard E., "Basic hemodynamic principles," CV Physiology, 2023. [Online]. Available: https://cvphysiology.com/hemodynamics/h001

[56] Harvard Natural Sciences Lecture Demonstrations, "Poiseuille's law," Harvard Natural Sciences Lecture Demonstrations, 2025. [Online]. Available: https://sciencedemonstrations.fas.harvard.edu/presentations/poiseuilles-law

[57] Klabunde, Richard E., "Determinants of resistance to flow (poiseuille's equation)," CV Physiology, 2023. [Online]. Available: https://cvphysiology.com/hemodynamics/h003

[58] B. Zhang, X. Chen, W. Qin, L. Ge, X. Zhang, G. Ding, and S. Wang, "Enhancing cerebral arteriovenous malformation analysis: Development and application of patient-specific lumped parameter models based on 3d imaging data," *Computers in Biology and Medicine*, vol. 180, 9 2024.

[59] J. A. Abbott, *Syncope and Sudden Cardiac Death.* Elsevier, 2000, pp. 23–27.

[60] A. Silverman and N. H. Petersen, *Physiology, Cerebral Autoregulation.* National Center for Biotechnology Information, 2020.

[61] S. Rossitti, "Pathophysiology of increased cerebrospinal fluid pressure associated to brain arteriovenous malformations: The hydraulic hypothesis." *Surgical neurology international*, vol. 4, p. 42, 2013.

[62] C. P. Derdeyn, G. J. Zipfel, F. C. Albuquerque, D. L. Cooke, E. Feldmann, J. P. Sheehan, and J. C. Torner, "Management of brain arteriovenous malformations: A scientific statement for healthcare professionals from the american heart association/american stroke association," pp. e200–e224, 8 2017.

[63] K. Irikura, S. Morii, Y. Miyasaka, M. Yamada, K. Tokiwa, and K. Yada, "Impaired autoregulation in an experimental model of chronic cerebral hypoperfusion in rats," *Stroke*, vol. 27, pp. 1399–1404, 1996.

[64] N. Collins and A. Abd-Elsayed, *Cerebral perfusion pressure.* CRC Press, 1 2017, pp. 31–38.

[65] N. A. Lassen, "Normal average value of cerebral blood flow in younger adults is 50 ml/100 g/min," *Journal of Cerebral Blood Flow and Metabolism*, vol. 5, pp. 347–349, 1985.

[66] S. Fantini, A. Sassaroli, K. T. Tgavalekos, and J. Kornbluth, "Cerebral blood flow and autoregulation: current measurement techniques and prospects for noninvasive optical methods," *Neurophotonics*, vol. 3, p. 031411, 6 2016.

[67] R. Kim, Y. S. Do, and K. B. Park, "How to treat peripheral arteriovenous malformations," *Korean Journal of Radiology*, vol. 22, pp. 568–576, 4 2021.

[68] T. C. Cuong, L. M. Thang, N. L. Giang, N. A. Trung, L. V. Qui, T. T. T. Tha, N. D. N. Huy, T. V. Lam, D. H. Linh, and N. M. Duc, "Recurrent head and neck arteriovenous malformations: A case report," *Radiology Case Reports*, vol. 18, pp. 766–770, 3 2023.

[69] A. J. Awad, B. P. Walcott, C. J. Stapleton, D. Ding, C. C. Lee, and J. S. Loeffler, "Repeat radiosurgery for cerebral arteriovenous malformations," pp. 945–950, 6 2015.

[70] R. F. Spetzler and N. A. Martin, "A proposed grading system for arteriovenous malformations," *Journal of Neurosurgery*, vol. 65, pp. 476–483, 1986.

[71] A. Hafez, P. Koroknay-Pál, E. Oulasvirta, A. A. Elseoud, M. T. Lawton, M. Niemelä, and A. Laakso, "The application of the novel grading scale (lawton-young grading system) to predict the outcome of brain arteriovenous malformation," *Clinical Neurosurgery*, vol. 84, pp. 529–536, 2 2019.

[72] G. M. Sicuri, N. Galante, and R. Stefini, *Brain Arteriovenous Malformations Classifications: A Surgical Point of View*. Springer Science and Business Media Deutschland GmbH, 2021, vol. 132, pp. 101–106.

[73] T. M. Dumont, P. Kan, K. V. Snyder, L. N. Hopkins, A. H. Siddiqui, and E. I. Levy, "A proposed grading system for endovascular treatment of cerebral arteriovenous malformations: Buffalo score," *Surgical Neurology International*, vol. 6, 1 2015.

[74] Mayo Clinic, "Brain avm (arteriovenous malformation) – diagnosis and treatment," Mayo Clinic, 2025. [Online]. Available: https://www.mayoclinic.org/diseases-conditions/brain-avm/diagnosis-treatment/drc-20350265

[75] A. K. Unnithan, "Overview of the current concepts in the management of arteriovenous malformations of the brain," pp. 212–220, 4 2020.

[76] J. Byun, D. H. Kwon, D. H. Lee, W. Park, J. C. Park, and J. S. Ahn, "Radiosurgery for cerebral arteriovenous malformation (avm) : Current treatment strategy and radiosurgical technique for large cerebral avm." *Journal of Korean Neurosurgical Society*, vol. 63, pp. 415–426, 7 2020.

[77] B. E. Pollock, R. W. Kline, S. L. Stafford, R. L. Foote, and P. J. Schomberg, "The rationale and technique of staged-volume arteriovenous malformation radiosurgery," *International Journal of Radiation Oncology Biology Physics*, vol. 48, pp. 817–824, 10 2000.

[78] G. T. Szeifert, A. A. Kemeny, W. R. Timperley, and D. M. Forster, "The potential role of myofibroblasts in the obliteration of arteriovenous malformations after radiosurgery," *Neurosurgery*, vol. 40, pp. 61–66, 1 1997.

[79] S. Fogh, L. Ma, N. Gupta, A. Sahgal, J. L. Nakamura, I. Barani, P. K. Sneed, M. McDermott, and D. A. Larson, "High-precision volume-staged gamma knife surgery and

equivalent hypofractionation dose schedules for treating large arteriovenous malformations." *Journal of neurosurgery*, vol. 117 Suppl, pp. 115–119, 2012.

[80] C. P. Cifarelli, J. A. Vargo, T. Tenenholz, J. D. Hack, G. Guthrie, and J. S. Carpenter, "Gamma knife radiosurgery for arteriovenous malformations using a four-dimensional dynamic volume computed tomography angiography planning system as an alternative to traditional catheter angiogram." *Cureus*, vol. 10, p. e2788, 6 2018.

[81] S. N. Shah, S. S. Shah, P. Kaki, S. R. Satti, and S. A. Shah, "Efficacy of dose-escalated hypofractionated radiosurgery for arteriovenous malformations," *Cureus*, 1 2024.

[82] C. S. Haw, K. Terbrugge, R. Willinsky, and G. Tomlinson, "Complications of embolization of arteriovenous malformations of the brain," pp. 226–232, 2 2006.

[83] The Kingsley Clinic, "Embolization for arteriovenous malformations: Minimally invasive treatment," The Kingsley Clinic, 2025. [Online]. Available: https://thekingsleyclinic.com/resources/embolization-for-arteriovenous-malformations-minimally-invasive-treatment/

[84] WakeMed Health & Hospitals, "Embolization: What to expect," WakeMed Health & Hospitals, 2025. [Online]. Available: https://www.wakemed.org/care-and-services/surgery/interventional-radiology/vascular-tumors-and-arteriovenous-malformations-avm/embolization-what-to-expect

[85] Barnes-Jewish Hospital, "Avm embolization," Barnes-Jewish Hospital, 2025. [Online]. Available: https://www.barnesjewish.org/Medical-Services/Neurology-Neurosurgery/AVM-Arteriovenous-Malformation/AVM-Treatment/AVM-Embolization

[86] Mount Sinai Health System, "Endovascular embolization," Mount Sinai Health Library, 2025. [Online]. Available: https://www.mountsinai.org/health-library/surgery/endovascular-embolization

[87] W. C. Jean, T. Huynh, A. X. Tai, D. R. Felbaum, H. R. Syed, and H. M. Ngo, "Outcome of microsurgery for arteriovenous malformations in a resource-restricted environment: Single-surgeon series from vietnam," *World Neurosurgery*, vol. 132, pp. e66–e75, 12 2019.

[88] Eminence Neurosurgery, "Avm and davf – microsurgery," Eminence Neurosurgery, 2025. [Online]. Available: https://eminenceneurosurgery.com.au/procedures/avm-and-davf-microsurgery

[89] J. A. Ellis and S. D. Lavine, "Role of embolization for cerebral arteriovenous malformations," pp. 234–239, 10 2014.

[90] R. D. Leacy, S. A. Ansari, C. M. Schirmer, D. L. Cooke, C. J. Prestigiacomo, K. R. Bulsara, and S. W. Hetts, "Endovascular treatment in the multimodality management of brain arteriovenous malformations: report of the society of neurointerventional surgery standards and guidelines committee," *Journal of NeuroInterventional Surgery*, vol. 14, pp. 1118–1124, 4 2022.

[91] S. Luzzi, M. D. Maestro, D. Bongetta, C. Zoia, A. V. Giordano, D. Trovarelli, S. R. Dehcordi, and R. J. Galzio, "Onyx embolization before the surgical treatment of grade iii spetzler-martin brain arteriovenous malformations: Single-center experience and technical nuances," *World Neurosurgery*, vol. 116, pp. e340–e353, 8 2018.

[92] N. V. de Oliveira Souza, T. Lamiraux, F. V. da Silva, V. M. Lima, A. Rouchaud, S. Saleme, and C. Mounayer, "Endovascular treatment of spetzler-martin grade iii arteriovenous malformations: A single-center 12 years' experience stratified by the spetzler-martin modified scale," *Neurosurgery*, 12 2024.

[93] Y. Chen, R. Li, L. Ma, Y. Zhao, T. Yu, H. Wang, X. Ye, R. Wang, X. Chen, and Y. Zhao, "Single-stage combined embolization and resection for spetzler-martin grade iii/iv/v arteriovenous malformations: A single-center experience and literature review," *Frontiers in Neurology*, vol. 11, 10 2020.

[94] W. Huda and K. R. Peters, "Radiation-induced temporary epilation after a neuroradiologically guided embolization procedure," *Radiology*, vol. 193, pp. 642–644, 1994.

[95] R. B. Mooney, C. S. McKinstry, and H. A. Kamel, "Absorbed dose and deterministic effects to patients from interventional neuroradiology," *British Journal of Radiology*, vol. 73, pp. 745–751, 2000.

[96] N. Kuwayama, A. Takaku, S. Endo, M. Nishijima, and T. Kamei, "Radiation exposure in endovascular surgery of the head and neck," *American Journal of Neuroradiology*, vol. 15, pp. 1801–1808, 1994.

[97] M. K. Varma, K. Price, V. Jayakrishnan, B. Manickam, and G. Kessell, "Anaesthetic considerations for interventional neuroradiology," pp. 75–85, 2007.

[98] T. F. Massoud, G. J. Hademenos, W. L. Young, E. Gao, and J. Pile-Spellman, "Can induction of systemic hypotension help prevent nidus rupture complicating arteriovenous malformation embolization?: Analysis of underlying mechanisms achieved using a theoretical model," *American Journal of Neuroradiology*, vol. 21, pp. 1255–1267, 2000.

[99] K. Riedel, M. Thudium, A. Boström, J. Schramm, and M. Soehle, "Controlled arterial hypotension during resection of cerebral arteriovenous malformations," *BMC Neurology*, vol. 21, 12 2021.

[100] Y. He, W. Bai, T. Li, F. K. Hui, Y. He, and B. Xu, "Curative transvenous embolization for ruptured brain arteriovenous malformations: A single-center experience from china," *World Neurosurgery*, vol. 116, pp. e421–e428, 8 2018.

[101] S. N. Veloso, I. Lylyk, P. N. Lylyk, J. Lundquist, and P. Lylyk, *Symptomatic Arteriovenous Malformation (Spetzler-Martin Grade III): Staged Transarterial and Final Transvenous Embolization; Complete Occlusion of the AVM and Excellent Clinical Outcome*. Springer International Publishing, 2021, pp. 1–12.

[102] F. C. Albuquerque, A. F. Ducruet, R. W. Crowley, R. E. Bristol, A. Ahmed, and C. G. McDougall, "Transvenous to arterial onyx embolization," *Journal of NeuroInterventional Surgery*, vol. 6, pp. 281–285, 2014.

[103] B. C. Brahimaj, K. Keigher, and D. K. Lopes, "Transvenous arteriovenous malformation embolization," *Journal of neurointerventional surgery*, vol. 12, p. 332, 3 2020.

[104] C. J. Chen, P. Norat, D. Ding, G. A. Mendes, P. Tvrdik, M. S. Park, and M. Y. Kalani, "Transvenous embolization of brain arteriovenous malformations: A review of techniques, indications, and outcomes," *Neurosurgical Focus*, vol. 45, pp. 1–7, 7 2018.

[105] I. Kuianova, A. Chupakhin, A. Besov, A. Gorbatykh, D. Kislitsin, K. Orlov, and D. Parshin, "Rheological properties of non-adhesive embolizing compounds—the key to fine-tuning embolization process-modeling in endovascular surgery," *Polymers*, vol. 15, 2 2023.

[106] Medtronic, "Onyx™ liquid embolic system for peripheral embolization," 2024. [Online]. Available: https://europe.medtronic.com/xd-en/healthcare-professionals/products/cardiovascular/peripheral-embolization/onyx-liquid-embolic-system.html

[107] A. H. White and F. T. Smith, "Computational modelling of the embolization process for the treatment of arteriovenous malformations (avms)," *Mathematical and Computer Modelling*, vol. 57, pp. 1312–1324, 3 2013.

[108] J. M. Anderson, A. Rodriguez, and D. T. Chang, "Foreign body reaction to biomaterials," pp. 86–100, 4 2008.

[109] kg m3.com, "Evoh - ethylene vinyl alcohol," 2020. [Online]. Available: https://kg-m3.com/material/evoh-ethylene-vinyl-alcohol

[110] J. Rössberger, M. Fall, and R. Peeker, "Critical appraisal of dimethyl sulfoxide treatment for interstitial cystitis: Discomfort, side-effects and treatment outcome," *Scandinavian Journal of Urology and Nephrology*, vol. 39, pp. 73–77, 2005.

[111] C. Mahajan and N. Gupta, *Vasospasm*. Elsevier Inc., 2016, pp. 103–109.

[112] T. Aizawa, Y. Hasegawa, G. Araki, K. Mori, K. Yoshida, N. Sato, S. Nagano, H. Nakamura, M. Kato, and K. Kojima, "Studies on experimental cerebral vascular lesion. reference to ischemic angionecrosis and microcirculation," in *Proceedings of the Annual Meeting of the Japanese Society of Pathology*. Keio University, Dept. of Internal Medicine, School of Medicine, 1983, p. S15, abstract presentation.

[113] R. Siekmann, "Basics and principles in the application of onyx ld liquid embolic system in the endovascular treatment of cerebral arteriovenous malformations." *Interventional neuroradiology : journal of peritherapeutic neuroradiology, surgical procedures and related neurosciences*, vol. 11, pp. 131–40, 10 2005.

[114] Micro Therapeutics, Inc. (MTI), *Onyx® Liquid Embolic System: Instructions for Use*, [Online]. Available: https://www.accessdata.fda.gov/scripts/cdrh/cfdocs/cfpmn/pmn.cfm, Medtronic, 2023, retrieved from product labeling.

[115] X. Deng, M. Dong, C. Peng, X. Ding, K. Wang, K. Qin, and G. Chen, "Embolizing intracranial arteriovenous malformations with onyx: experience at a single center with 250 patients." *Journal of interventional medicine*, vol. 1, pp. 164–169, 8 2018.

[116] V. Panagiotopoulos, E. Gizewski, S. Asgari, J. Regel, M. Forsting, and I. Wanke, "Embolization of intracranial arteriovenous malformations with ethylene-vinyl alcohol copolymer (onyx)," *American Journal of Neuroradiology*, vol. 30, pp. 99–106, 1 2009.

[117] Medtronic, "Apollo™ and marathon™ flow directed microcatheters," 2024. [Online]. Available: https://europe.medtronic.com/xd-en/healthcare-professionals/products/neurological/avm-embolization/apollo-marathon.html

[118] I. Saatci, S. Geyik, K. Yavuz, and H. S. Cekirge, "Endovascular treatment of brain arteriovenous malformations with prolonged intranidal onyx injection technique: Long-term results in 350 consecutive patients with completed endovascular treatment course - clinical article," *Journal of Neurosurgery*, vol. 115, pp. 78–88, 7 2011.

[119] L. Pierot, C. Cognard, D. Herbreteau, H. Fransen, W. J. V. Rooij, E. Boccardi, A. Beltramello, N. Sourour, K. Kupcs, A. Biondi, A. Bonafé, W. Reith, and A. Casasco, "Endovascular treatment of brain arteriovenous malformations using a liquid embolic agent: Results of a prospective, multicentre study (bravo)," *European Radiology*, vol. 23, pp. 2838–2845, 10 2013.

[120] P. Orlowski, F. Al-Senani, P. Summers, J. Byrne, J. A. Noble, and Y. Ventikos, "Towards treatment planning for the embolization of arteriovenous malformations of the brain: Intranidal hemodynamics modeling," *IEEE Transactions on Biomedical Engineering*, vol. 58, pp. 1994–2001, 7 2011.

[121] S. A. Wajihah and D. S. Sankar, "A review on non-newtonian fluid models for multi-layered blood rheology in constricted arteries," pp. 1771–1796, 5 2023.

[122] K. Yamashita, W. Taki, H. Iwata, I. Nakahara, S. Nishi, A. Sadato, K. Matsumoto, and H. Kikuchi, "Characteristics of ethylene vinyl alcohol copolymer (eval) mixtures," *American Journal of Neuroradiology*, vol. 15, pp. 1103–1105, 1994.

[123] G. Franzetti, M. Bonfanti, C. Tanade, C. S. Lim, J. Tsui, G. Hamilton, V. Díaz-Zuccarini, and S. Balabani, "A computational framework for pre-interventional planning of peripheral arteriovenous malformations," *Cardiovascular Engineering and Technology*, vol. 13, pp. 234–246, 4 2022.

[124] OpenStax CNX, "Blood flow, blood pressure, and resistance," Lumen Learning: Anatomy and Physiology II, Module 4, 2025. [Online]. Available: https://courses.lumenlearning.com/suny-ap2/chapter/blood-flow-blood-pressure-and-resistance-no-content/

[125] A. M. Malek, S. L. Alper, and S. Izumo, "Hemodynamic shear stress and its role in atherosclerosis," *Journal of the American Medical Association*, vol. 282, pp. 2035–2042, 12 1999.

[126] M. Hu, B. Chen, and Y. Luo, "Computational fluid dynamics modelling of hemodynamics in aortic aneurysm and dissection: a review." *Frontiers in bioengineering and biotechnology*, vol. 13, p. 1556091, 2025.

[127] F. Ene, P. Delassus, and L. Morris, "The influence of computational assumptions on analysing abdominal aortic aneurysm haemodynamics," *Proceedings of the Institution of Mechanical Engineers, Part H: Journal of Engineering in Medicine*, vol. 228, pp. 768–780, 8 2014.

[128] D. Ren, J. Li, B. Zhou, S. Guo, and B. Guo, "Modeling of the dynamics of vascular embolization by using porous media for the design of injection robots of embolic agents," *Medical Engineering and Physics*, vol. 101, 3 2022.

[129] C. A. Taylor, T. J. Hughes, and C. K. Zarins, "Finite element modeling of blood flow in arteries," *Computer Methods in Applied Mechanics and Engineering*, vol. 158, pp. 155–196, 1998.

[130] A. Niemann and D. Behme, "Deep learning-based semantic vessel graph extraction for intracranial aneurysm rupture risk management," *International Journal of Computer Assisted Radiology and Surgery*, vol. 18, no. 3, pp. 473–481, Mar. 2023.

[131] V. Naik, "New fluent meshing workflow quickly wraps non-watertight, dirty geometries," ANSYS Blog, Jun. 2019, [Online; accessed 21-May-2025]. [Online]. Available: https://www.ansys.com/blog/fluent-meshing-workflow-wraps-non-watertight-geometries

[132] K. H. Yang, *Isoparametric Formulation and Mesh Quality*. Elsevier, 1 2017, pp. 111–149.

[133] Simmetrix Inc., "Boundary layer meshing," Online: Simmetrix, 2025. [Online]. Available: https://www.simmetrix.com/index.php/technologies/boundary-layers

[134] R. V. Garimella and M. S. Shephard, "Boundary layer mesh generation for viscous flow simulations," *International Journal for Numerical Methods in Engineering*, vol. 49, pp. 193–218, 9 2000.

[135] *ANSYS Fluent Theory Guide*, ANSYS Inc., 2013, release 15.0. [Online]. Available: https://www.ansys.com

[136] P. Subrahmanyam and D. Rasky, "Entry, descent, and landing technological barriers and crewed mars vehicle performance analysis," pp. 1–26, 5 2017.

[137] P. O'Gorman, I. Chiavacci, and H. Knipe, "Propagation speed," Radiopaedia.org, Aug. 2021. [Online]. Available: https://radiopaedia.org/articles/propagation-speed

[138] L. Allard and G. Cloutier, "Power doppler ultrasound scan imaging of the level of red blood cell aggregation: An in vitro study," *Journal of Vascular Surgery*, vol. 30, pp. 157–168, 1999.

[139] R. A. Phillips, B. E. Smith, and V. M. Madigan, "Stroke volume monitoring: Novel continuous wave doppler parameters, algorithms and advanced noninvasive haemodynamic concepts," *Current Anesthesiology Reports*, vol. 7, pp. 387–398, 12 2017.

[140] C. Zhang, N. Chau, and H. Ho, "Patient-specific blood flow analysis for cerebral arteriovenous malformation based on digital subtraction angiography images," *Frontiers in Bioengineering and Biotechnology*, vol. 8, 7 2020.

[141] U. Themes, "Cerebral doppler sonography," n.d., accessed: 2025-03-29. [Online]. Available: https://radiologykey.com/cerebral-doppler-sonography/

[142] L. Zarrinkoob, K. Ambarki, A. Wåhlin, R. Birgander, A. Eklund, and J. Malm, "Blood flow distribution in cerebral arteries," *Journal of Cerebral Blood Flow and Metabolism*, vol. 35, pp. 648–654, 3 2015.

[143] R. R. Diehl, H. Henkes, H. C. Nahser, D. Kuhne, and P. Berlit, "Blood flow velocity and vasomotor reactivity in patients with arteriovenous malformations: A transcranial doppler study," *Stroke*, vol. 25, pp. 1574–1580, 1994.

[144] J. Tu, G.-H. Yeoh, and C. Liu, *CFD Solution Analysis: Essentials*. Elsevier, 2018, pp. 211–253.

[145] B. Liu, J. Zheng, R. Bach, and D. Tang, "Influence of model boundary conditions on blood flow patterns in a patient specific stenotic right coronary artery," *Biomedical engineering online*, vol. 14, p. S6, 2015.

[146] I. C. Campbell, J. Ries, S. S. Dhawan, A. A. Quyyumi, W. R. Taylor, and J. N. Oshinski, "Effect of inlet velocity profiles on patient-specific computational fluid dynamics simulations of the carotid bifurcation," *Journal of Biomechanical Engineering*, vol. 134, 2012.

[147] T. Bomberna, "Computational fluid dynamics models for patient-specific planning of liver transarterial radioembolization," Doctoral Dissertation, Ghent University, Ghent, Belgium, Sep. 2024, supervisors: Prof. Charlotte Debbaut, PhD and Prof. Geert Maleux, PhD. Joint research with KU Leuven.

[148] J. Zeebroek, "Using cfd for the evaluation of side-hole catheters and injection velocity on particle spread for transarterial liver cancer treatments: A patient-specific case study," Master's Dissertation, Ghent University, Ghent, Belgium, 2024, supervisor: Prof. Dr. Ir. Charlotte Debbaut. Counsellor: Tim Bomberna. Academic year 2023–2024.

[149] J. Aramburu, R. Antón, A. Rivas, J. C. Ramos, B. Sangro, and J. I. Bilbao, "Computational assessment of the effects of the catheter type on particle–hemodynamics during liver radioembolization," *Journal of Biomechanics*, vol. 49, pp. 3705–3713, 11 2016.

[150] A. Taebi, N. Janibek, R. Goldman, R. Pillai, C. T. Vu, and E. Roncali, "The impact of injection distance to bifurcations on yttrium-90 distribution in liver cancer radioembolization," *Journal of Vascular and Interventional Radiology*, vol. 33, pp. 668–677.e1, 6 2022.

[151] X. Lv, Z. Wu, and Y. Li, "Arteriovenous malformation in the brain: A theoretical study explaining the behavior of liquid embolic agents during endovascular treatment," *Neuroradiology Journal*, vol. 26, pp. 661–668, 2013.

[152] Y. Li, X. xia Tian, T. Liu, and R. tao Wang, "Association between whole blood viscosity and arterial stiffness in patients with type 2 diabetes mellitus," *Endocrine*, vol. 49, pp. 148–154, 5 2015.

[153] B. Stojadinović and T. Tenne, "Effect of viscosity on the wave propagation: Experimental determination of compression and expansion pulse wave velocity in fluid-fill elastic tube," *Journal of Biomechanics*, vol. 48, pp. 3969–3974, 11 2015.

[154] S. V. Golovin, A. K. Khe, and K. A. Gadylshina, "Hydraulic model of cerebral arteriovenous malformations," *Journal of Fluid Mechanics*, vol. 797, pp. 110–129, 6 2016.

[155] T. Y. Abay, J. P. Phillips, C. Uff, M. Roldan, and P. A. Kyriacou, "In vitro evaluation of a non-invasive photoplethysmography based intracranial pressure sensor," *Applied Sciences (Switzerland)*, vol. 13, 1 2023.

[156] L. Zacchetti, S. Magnoni, F. D. Corte, E. R. Zanier, and N. Stocchetti, "Accuracy of intracranial pressure monitoring: Systematic review and meta-analysis," *Critical Care*, vol. 19, 12 2015.

[157] X. Chen, Y. Wang, and J. Yu, "Intra- and post-operative acute hemorrhagic complications of onyx embolization of brain arteriovenous malformations: A single-center experience," *Frontiers in Neurology*, vol. 13, 9 2022.

[158] S. Schnell, C. Wu, and S. A. Ansari, "Four-dimensional mri flow examinations in cerebral and extracerebral vessels - ready for clinical routine?" pp. 419–428, 8 2016.

[159] A. G. Morgan, M. J. Thrippleton, J. M. Wardlaw, and I. Marshall, "4d flow mri for non-invasive measurement of blood flow in the brain: A systematic review," pp. 206–218, 2 2021.

[160] D. T. Wymer, K. P. Patel, W. F. Burke, and V. K. Bhatia, "Phase-contrast mri: Physics, techniques, and clinical applications," *Radiographics*, vol. 40, pp. 122–140, 1 2020.

[161] C. Hoffman, S. Periyasamy, C. Longhurst, R. Medero, A. Roldan-Alzate, M. A. Speidel, and P. F. Laeseke, "A technique for intra-procedural blood velocity quantitation using time-resolved 2d digital subtraction angiography," *CVIR Endovascular*, vol. 4, no. 1, p. 11, 2021. [Online]. Available: https://doi.org/10.1186/s42155-020-00058-7

[162] D. Katritsis, L. Kaiktsis, A. Chaniotis, J. Pantos, E. P. Efstathopoulos, and V. Marmarelis, "Wall shear stress: Theoretical considerations and methods of measurement," *Progress in Cardiovascular Diseases*, vol. 49, no. 5, pp. 307–329, 2007.

[163] X. Chen, J. Zhuang, H. Huang, and Y. Wu, "Fluid–structure interactions (fsi) based study of low-density lipoproteins (ldl) uptake in the left coronary artery," *Scientific Reports*, vol. 11, 12 2021.

[164] A. M. Shaaban and A. J. Duerinckx, "Wall shear stress and early atherosclerosis: A review," pp. 1657–1665, 2000.

[165] H. Deng, X. Liu, T. Fang, Y. Li, and X. Min, "Dfa-net: Dual multi-scale feature aggregation network for vessel segmentation in x-ray digital subtraction angiography," *Journal of Big Data*, vol. 11, 12 2024.

[166] R. Su, P. M. van der Sluijs, Y. Chen, S. Cornelissen, R. van den Broek, W. H. van Zwam, A. van der Lugt, W. J. Niessen, D. Ruijters, and T. van Walsum, "Cave: Cerebral artery–vein segmentation in digital subtraction angiography," *Computerized Medical Imaging and Graphics*, vol. 94, p. 101986, 2022. [Online]. Available: https://doi.org/10.1016/j.compmedimag.2022.101986

[167] N. Ballas, L. Yao, C. Pal, and A. Courville, "Delving deeper into convolutional networks for learning video representations," in *4th International Conference on Learning Representations, ICLR 2016 - Conference Track Proceedings*. International Conference on Learning Representations, ICLR, 2016.

[168] United Nations, "Sustainable development goals," 2015. [Online]. Available: https://sdgs.un.org/goals

Appendix A

Additional Information on Tools and Settings in Mimics, 3-Matic, ANSYS Discovery, and Fluent Meshing

This appendix contains a chronological summary of the employed tools with some additional explanation and parameters listed for each of the software used for segmentation and meshing of the AVM model.

Operation/Tool	**Explanation**	**Additional Settings**
'Threshold'	Initial threshold-based segmentation	1250 to 14084 GV
'Smooth'	Smoothing of 3D Part	Step 1: Smoothing factor: 0.7, 20 iterations, shrinkage compensated. Step 2: Smoothing factor: 0.9, 20 iterations, shrinkage compensated.
'Analyze' > 'Plane'	Define planes	/
'3D Tools' > 'Subtract'	Cut off in- or outlets using planes	/
'Export' > 'IGES' > 'Analysis'	Save the centerlines of the inlets as .iges files	/

Table A.1: Overview of operations in Mimics with explanations and relevant settings.

Operation/Tool	**Explanation**	**Additional Settings**
'Design' > 'Move Surface'	Extrude the outlets	/
'Remove Spikes'	Remove remaining spikes in the mesh	Spike size: 0.1 mm, Smallest detail: 0.1 mm, Preserve surface detail: Checked
'Adaptive Remesh'	Perform adaptive remeshing	Target triangle length: 0.4 mm, Preserve surface contours: Checked, Minimum skewness: 0.4
'Uniform Remesh'	Perform uniform remeshing	Target triangle length: 0.4 mm, Preserve surface contours: Checked
Diagnostic options, including 'Normals', 'Stitching', 'Noise', 'Shells', 'Holes', 'Triangles', and 'Overlaps'	Operations to ensure good mesh quality	Were all reviewed and, if necessary, automatically updated

Table A.2: Overview of operations in 3-Matic with explanations and relevant settings.

Operation/Tool	**Explanation**	**Additional Settings**
Type of flow	Define where the flow will be w.r.t. the geometry	Internal flow through an object
Local Refinement	Locally impose a smaller mesh size	See in Section 2.1.5 'Mesh Sensitivity Analysis'
Surface Mesh Generation	Generation of surface mesh	Surface mesh target skewness: 0.8
Boundary Layers	Add boundary layers	Offset method type: 'Aspect-ratio'
Volume Mesh Generation	Generation of volume mesh	Quality Improve Limit: 0.04

Table A.3: Overview of meshing operations in Fluent Meshing with explanations and relevant settings.

Operation/Tool	**Explanation**	**Additional Settings**
'Plane,' 'Sketch,' 'Cylinder,' 'Sweep,' and 'Convert' tools	Modeling of the catheters	/
'Holes' tool	Creates closed surfaces at the inlets and outlets	/
'Subtract' tool	Remove the catheter volumes from the AVM model	/
'Select' and 'Delete facets' tools	Used to define inlets and outlets for blood and Onyx	/

Table A.4: Overview of operations in Ansys Discovery with explanations.

Appendix B

Workflow for Implementation of Catheters in ANSYS Discovery

This appendix describes a detailed workflow followed in ANSYS Discovery to create a model for the AVM with two catheters implemented (one in each feeding artery). This appendix outlines the detailed workflow used in ANSYS Discovery to develop the model of the AVM, incorporating two catheters—one placed in each feeding artery. The steps presented here give insight into the modeling process and serve as a reference for reproducing or extending this modeling workflow.

First of all, the model of the AVM geometry was loaded.

- A surface mesh of the model was saved from 3-Matic as an .stl file and loaded into Discovery via /// > 'Open'.

The next step is to create the catheters.

- These catheters were aligned along the centerlines of the arterial feeder flows and the microcatheter tip locations were estimated based on angiography images. The centerlines of the relevant parts were exported from Mimics as .iges files via 'Export' > 'IGES' > 'Analysis' and loaded into Discovery via /// > 'Insert Geometry'.
- Via the 'Select point' tool in the 'Design' menu, a point at the start of this centerline was selected; and via the 'Plane' tool in the 'Design' menu, a plane was defined that goes through this point and is normal to the centerline.
- This plane was selected as a sketch plane via the 'Sketch' mode in the 'Design' menu.

- In sketch mode, the 'Circle' option in the 'Design' menu was used to draw a circle in this sketch plane with a diameter of 0.3302 mm. (So the catheter diameter was here set to 0.3302 mm, matching the inner diameter of the Apollo microcatheter. However, ideally a thickness would be assigned to the catheter, as is the case in reality.)
- Then the sketch mode was left, and the '3D mode' was again selected.
- To obtain a 3D catheter, this created circle was pulled along the whole centerline by selecting the 'Pull' option in the 'Design' menu, and then selecting the option to 'sweep' around a curve, and for this curve selecting the imported centerline.
- For the resulting catheters, the 'Auto Fix' tool from the 'Facets' menu was used; and afterwards, the 'Convert' tool from the 'Facets' menu was used to convert these catheter walls to faceted bodies.

Now, the outer surface of the AVM (but no in- and outlet planes yet) and the outer surface of the catheters are created, and the next step was to obtain a model with the in- and outlets for the blood phase.

- On the AVM geometry, the 'Holes' tool from the 'Facets' menu (with options 'Cap' and 'Separately') was used to obtain these planes at the in- and outlets of the AVM geometry.

Then, the catheters were subtracted from the AVM geometry to create a model in which the spaces occupied by the catheters were represented as voids.

- The 'Subtract' tool from the 'Facets' menu was used to remove the catheter volumes from the AVM model.

Furthermore, the wall of the AVM vessels, the catheter walls, the catheter end planes, and the blood in- and outlets all needed to be defined as separate structures.

- All of these were defined by making a copy of the whole geometry and then using 'Select' to select all the facets that did not belong to the structure, and 'Delete facets' to delete these unwanted facets until the desired structure remained. In the end, each of the structures was defined as a separate object in the object tree.

Lastly, to ensure all parts are nicely defined and no issues occur later in Fluent Meshing, some additional steps were needed.

- For all surfaces: select all facets of that surface with the 'Select tool' from the 'Design' menu, then right click and choose 'Add facetted region' (this way they are recognized by the program as one region that belongs together).
- On each part in the object tree: use the 'Convert' tool from the 'Facets' menu to convert them to solid bodies, choose the 'fully tesselated' option.

This final file can be saved as .fmd or .tgf to use it for further meshing in FLUENT meshing.

Appendix C

Convergence Evaluation of CFD Simulations

In numerical simulations such as CFD, convergence means that results no longer change significantly with more calculations, so changes between successive iterations become very small [144]. So, a converged solution becomes stable as the simulation progresses, which is necessary for reliable interpretation of results [144]. For this study, a time step was considered converged when the continuity, x-velocity, y-velocity, and z-velocity residuals each relatively decreased by at least three orders of magnitude (a popular convention [144]). In non-converged time steps, particular care is required, as the results might still contain numerical errors or instabilities [144]. Table C.1 provides the amount and portion of converged time steps for each of the simulations. While Figures C.1 and C.2, indicated the (not) converged time steps on the blood inlet velocity profile at inlet 1 (the branch from the ACA) for all the conducted simulations. This visualization helps identify periods of the simulation where results should be interpreted with caution. It is important to note, however, that the lack of convergence in some time steps was primarily due to time and computational resource limitations. Given extended simulation time and resources, convergence would likely be achieved for all time steps, and no fundamental numerical issues are expected.

Table C.1: Amount of converged time steps per conducted simulation. The convergence criterion was defined as a drop of at least three orders of magnitude for all residuals.

	Number of converged time steps	**Percentage of converged time steps**
Simulation without Onyx (only blood)	220/240	91.67 %
Simulation with Onyx injection at 0.08 ml/min	204/240	85.00 %
Simulation with Onyx injection at 0.16 ml/min	199/240	82.92 %
Simulation with Onyx injection at 0.32 ml/min	202/240	84.17 %

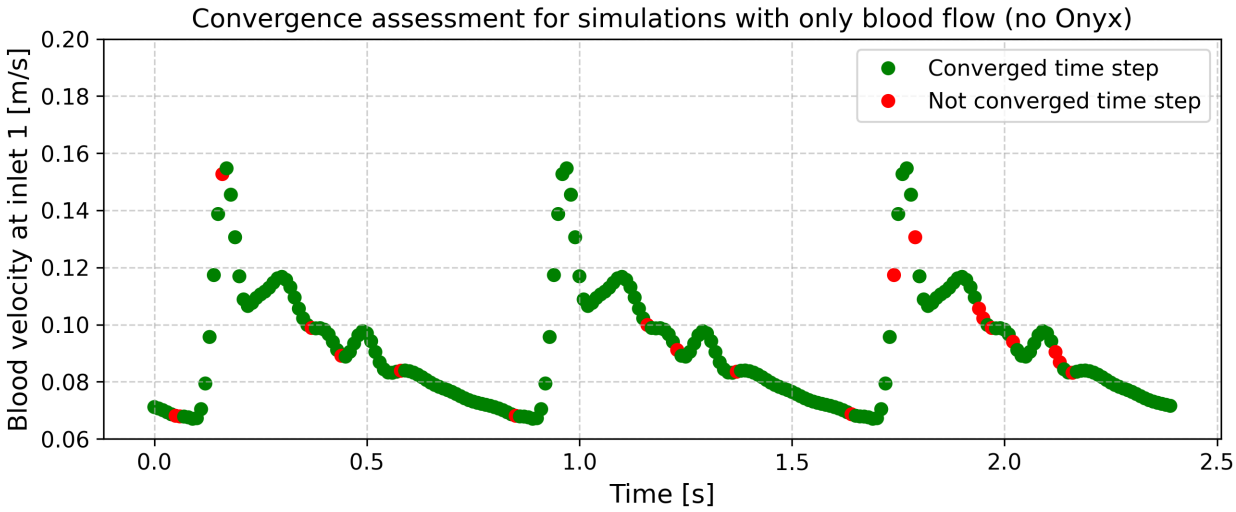

Figure C.1: Blood velocity at inlet 1 (branch from ACA) over time for three blood flow cycles with each point representing a simulation time step (of 0.10 s) for the simulation with only blood (before any Onyx injection). Green indicates time steps where full convergence was achieved (residuals relatively dropped by three orders of magnitude for continuity and velocity components), while red indicates time steps that did not meet the convergence criterion.

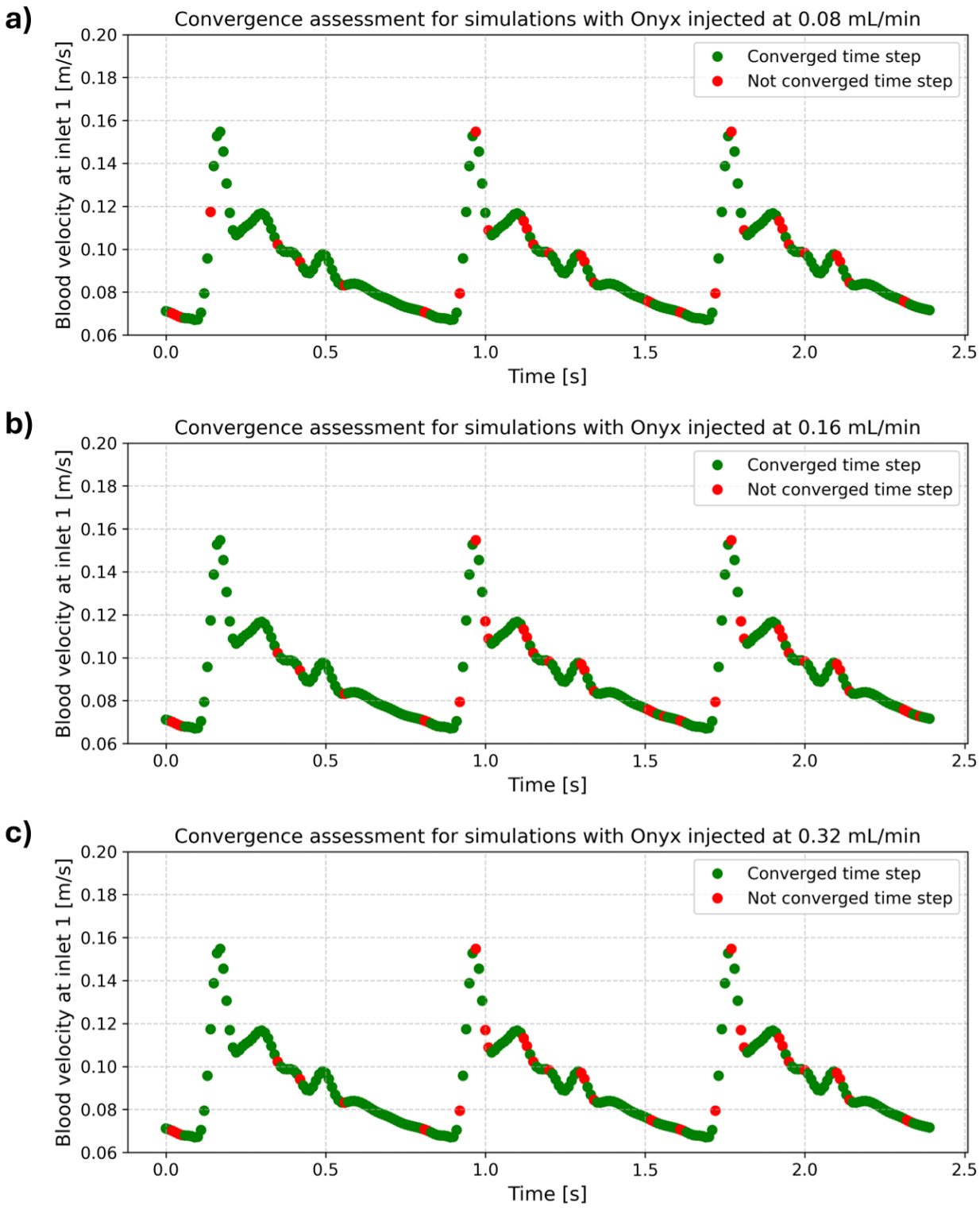

Figure C.2: Blood velocity at inlet 1 (branch from ACA) over time for three blood flow cycles with each point representing a simulation time step (of 0.10 s) for the simulations with Onyx injected at **a)** 0.08 ml/min, **b)** 0.16 ml/min, and **c)** 0.32 ml/min. Green indicates time steps where full convergence was achieved (residuals dropped by three orders of magnitude for continuity and velocity components), while red indicates time steps that did not meet the convergence criterion.

Appendix D

Workflow in Fluent for Mass Flow Rate Calculations

In this appendix, the precise workflow in ANSYS Fluent for the calculations of the mass flow rates through different branches after the injection site is described.

For all .dat files, which were saved every 0.10 s (so every 10 time steps of 0.01 s), the following steps were done in ANSYS Fluent:

- Via 'User-defined' > 'Custom Field Function', I defined a custom field function to determine the local mass flux (Equation D.1).

$$\dot{m}''_{\text{Onyx}} = \rho_o \cdot v \cdot \alpha_o \tag{D.1}$$

  With $\dot{m}''_{\text{Onyx}}$ the mass flux of Onyx [kg/s/m^2], ρ_o density of Onyx [kg/m^3], v velocity [m/s], and α_o volume fraction of Onyx phase [-].

- The surface integral was determined for this custom field function over the planes indicated in Figure 3.7.a via 'Results' > 'Report' > 'Surface Integrals' with 'Integral' as 'Report Type' and the custom field function as 'Field variable' (Equation D.2).

$$\dot{m}_{\text{o, through plane}} = \sum_{\text{all faces i of plane}} \rho_o \cdot v_i \cdot \alpha_{o,i} \cdot A_i \tag{D.2}$$

  With $\dot{m}_{\text{o, through plane}}$ mass flow rate of Onyx through a plane [kg/s], ρ_o density of

Onyx [kg/m^3], v_i velocity in face i [m/s], $\alpha_{o,i}$ volume fraction of Onyx in face i [-], and A_i area of face i [m^2].

To calculate the mass through each branch over a number of cycles as listed in Table 3.1, the mass flow rate at a certain time point was multiplied by the duration of a time step (here 0.10 s) over the different time steps over the duration T (T is either one, two, or three cycles, so 0.80 s, 1.60 s, or 2.40 s) (Equation D.3).

$$m_{\text{o, through plane, T}} = \sum_{\substack{t_i \in [0,T] \\ \Delta t \text{ intervals}}} \dot{m}_{\text{o, through plane}}(t_i) \cdot \Delta t \tag{D.3}$$

With $m_{\text{o, through plane, T}}$ mass of Onyx through plane over time T [kg], $\dot{m}_{\text{o, through plane}}(t_i)$ mass flow rate of Onyx through a plane at time t_i [kg/s], and Δt the length of the time interval [s] (in this case always 0.10 s).

Appendix E

Approval Letter from Ethics Committee

Afzender : Commissie voor medische ethiek

Prof. dr. Peter Vanlangenhove

UZ Gent

contact	telefoon	e-mail
Commissie voor medische ethiek	+32 (0)9 332 33 36	Ethisch.comite@uzgent.be
Aanvrager	**datum**	**pagina**
Kaat Wille	06/08/2024	1/6

Onze referentie:	EudraCT-nr:	Belg. Regnr:
ONZ-2024-0129 E02		B6702024000368

Betreft:
Blood flow modelling in brain vasculature during neuro-interventional procedures
Scriptie : Kaat Wille

Positief advies conform de wet van 7 mei 2004 betreffende experimenten op de menselijke persoon

Beste collega

De Commissie Medische Ethiek (CME) verbonden aan de Universiteit Gent (Ugent) en het Universitair Ziekenhuis Gent (UZ Gent) geeft op 06/08/2024 een gunstig advies over deze studie.

De Commissie voor Medische Ethiek beklemtoont dat een gunstig advies niet betekent dat de Commissie voor Medische Ethiek de verantwoordelijkheid voor het onderzoek op zich neemt.
De promotor en de hoofdonderzoeker dragen de verantwoordelijkheid voor het correcte ethische en wettelijke verloop van het onderzoek.

Ingediende documenten: zie bijlage 1
Ledenlijst: zie Bijlage 2
Aandachtspunten: zie Bijlage 3a

Met vriendelijke groeten,

Prof. dr. Renaat Peleman
Voorzitter
Commissie voor Medische Ethiek U(Z) Gent

ALGEMENE DIRECTIE
Commissie voor Medische Ethiek

VOORZITTER:
Prof. dr. R. Peleman

SECRETARIS:
Dr. L. Goossens

INGANG 75
ROUTE 7522

Unofficial translation in English:

Positive advice in accordance with the law of 7 May 2004 on experiments on the human person

The Ethics committee (EC) of University Ghent (Ugent) and Ghent University Hospital (UZ Gent) gives on 06/08/2024 a favourable opinion on this study

EC emphasizes that a favorable opinion does not mean that the Medical Ethics Committee assumes responsibility for the investigation.
The promoter and the principal investigator are responsible for the correct ethical and legal conduct of the research

Submitted documents: see Annex 1
List of members: see appendix 2
Points of concern: see appendix 3b

Bijlage 1: Documenten

Categorie: CV
- Curriculum vitae Kaat Wille,ontvangen dd. 05/07/2024

Alle goedgekeurde documenten van de hoofdstudie (ONZ-2024-0129)

Bijlage 2: Overzicht leden CME U(Z) Gent

voorzitter: Prof. dr. R. Peleman
Secretaris: Dr. L. Goossens

Effectief lid	**Plaatsvervangend lid**
Prof. dr. G. Van Lancker UZ Gent - klinisch farmacoloog, ♀	Prof. dr. S. Rottey UZ Gent - klinisch farmacoloog, ♀
Prof. dr. D. De Bacquer Ugent - statisticus, ♂	Prof. dr. P. Coorevits Ugent - statisticus, ♂
Dr. M. Cosyns Extern - huisarts, ♂	Dr. J. Matthys Extern - huisarts, ♂
Dr. J. Van Elsen Extern – huisarts ♂	Dr. J. Matthys Extern – huisarts, , ♂
Prof. dr. K. De Groote UZ Gent - kindercardioloog, ♀	Dr. P. De Bruyne UZ Gent - kinder gastro-enteroloog, ♀
Prof. dr. W. Notebaert UGent - psycholoog, ♂	Dhr. W. Schrauwen UGent - psycholoog, ♂
Mevr. R. Vrielynck UZ Gent - verpleegkundige, ♀	Mevr. A. Charles UZ Gent - verpleegkundige, ♀
Dhr. C. Demeestere UZ Gent - verpleegkundige, ♂	Dhr. G. De Smet UZ Gent - verpleegkundige, ♂
Apr. K. Kint UZ Gent - apotheker, ♀	Apr. L. Huys UZ Gent - apotheker, ♀
Dhr. B. Vanderhaegen UZ Gent - Ethicus, ♂	Dhr. K. Raus UZ Gent - Ethicus, ♂
Prof. dr. T. Goffin UGent - jurist, ♂	Mevr. V. Vanscheewijck UGent - jurist, ♀
Mevr. C. Van Caeneghem extern - patiëntvertegenwoordiger, ♀	Mevr. S. Degroote extern - patiëntvertegenwoordiger, ♀
Prof. dr. W. Van Biesen UZ Gent - nefroloog, ♂	Dr. A. Beyens UZ Gent - geneticus, ♀
Prof. dr. R. Peleman UZ Gent - internist en pneumoloog, ♂	Dr. L. Goossens UZ Gent - neonatoloog, ♀
Dr. T. Martens UZ Gent - hartchirurg, ♂	Dr. H. Eker UZ Gent - algemene en hepatobiliaire chirurg, ♂
Dr. L. Dhaenens UZ Gent - fertiliteitsarts, ♀	Dr. I. Dehaene UZ Gent - verloskunde, ♀
Dr. R. Van Der Looven UZ Gent - kinderrevalidatie, ♀	Dr. M. Neckebroek UZ Gent - anesthesist, ♀
Dr. E. Schoentjes UZ Gent - [kinder - jeugd]psychiater, ♂	Prof. dr. K. Dhondt UZ Gent - [kinder - jeugd]psychiater, ♀

Appendix 3a: Aandachtspunten (indien van toepassing)

De CME benadrukt de verantwoordelijkheid van de PI/promotor van dit onderzoek ten aanzien van de privacy van de persoons-/patiëntgegevens in contacten met patiënten, of bij het inzien van patiëntgegevens, inclusief de juiste uitvoering daarvan door collega's en studenten. De PI/promotor is verantwoordelijk voor de uitvoering van het projectvoorstel in overeenstemming met de toepasselijke wet- en regelgeving waaronder, maar niet beperkt tot, de EU-verordening 2016/679 (Algemene Verordening Gegevensbescherming), de Belgische Wet op de patiëntenrechten van 22/ 8/2002, en het beleid van de instelling waar het onderzoek wordt uitgevoerd.

De CME verwijst op haar website naar de ICH/GCP-richtlijnen en bevestigt dat van elke onderzoeker een GCP-training vereist is. Het is de verantwoordelijkheid van de hoofdonderzoeker dat elk lid van het onderzoeksteam een geldig GCP-certificaat heeft. De conformiteit van vertaalde documenten ten opzichte van de Nederlandse documenten is de verantwoordelijkheid van de opdrachtgever.

Wij vestigen uw aandacht op het feit dat de CME verwacht dat haar eerste opmerkingen ab initio in aanmerking worden genomen bij de volgende indiening door dezelfde sponsor.

Mits er een Clinical Trial Agreement is, kan de studie pas starten wanneer de Clinical Trial Agreement werd goedgekeurd en ondertekend door de CEO van het UZ Gent (en/of door een gemachtigde vertegenwoordiger van de UGent).

Studies met geneesmiddelen voor onderzoek en bepaalde studies met "medical devices" dienen door de klant (PI of sponsor) te worden ingediend bij het FAGG (Federaal Agentschap voor Geneesmiddelen en Gezondheidsproducten).

Studies met geneesmiddelen voor onderzoek mogen enkel uitgevoerd worden op voorwaarde dat de minister (FAGG) geen bezwaar maakt binnen de wettelijke termijnen zoals beschreven in art. 13 van de Belgische wet van 7/5/2004 betreffende experimenten op de menselijke persoon en in art. 21 van de Belgische wet van 7/05/2017 betreffende klinische proeven met geneesmiddelen voor menselijk gebruik.

Bepaalde onderzoeken met medische hulpmiddelen vallen ook onder wettelijke termijnen (KB van 17/3/2009). Raadpleeg de website van het FAGG voor meer informatie: www.fagg-afmps.be .

Onderzoek op embryo's in vitro valt onder de wet van 11 mei 2003. Alvorens het onderzoeksproject kan starten, vereist dergelijk onderzoek ook een positief advies van het Federaal Comité voor medisch en wetenschappelijk onderzoek op embryo's in vitro.

Gelieve rekening te houden met de reglementen van het ziekenhuis inzake weefselbeheer en de reglementen van de wet van 19 december 2008.

Dit gunstige advies van de CME houdt niet in dat zij de geplande studie op zich neemt. U blijft verantwoordelijk voor het onderzoek. Daarnaast dient u ervoor te zorgen dat uw mening als betrokken onderzoeker wordt weergegeven in publicaties, rapporten voor de overheid etc. die het resultaat zijn van dit onderzoek. U wordt eraan herinnerd dat met betrekking tot klinische onderzoeken elke waargenomen ernstige gebeurtenis onmiddellijk moet worden gemeld aan de sponsor en de ethische commissie, zelfs als het oorzakelijk verband met de studie onduidelijk is.

De CME-goedkeuring die voor een specifiek project wordt gegeven, is één jaar geldig. Wij verzoeken u ons te informeren als het onderzoek niet wordt gestart of als het onderzoek niet binnen 1 jaar na goedkeuring start.

De CME bevestigt dat - in geval van belangenverstrengeling - betrokken leden niet deelnemen aan de stemming over het onderzoek.

Indien het onderzoek niet binnen een jaar wordt beëindigd, eist de ICH-GCP dat jaarlijks een voortgangsrapportage aan de CME wordt verstrekt.

Tot slot verzoeken wij u de (voortijdige of geplande) beëindiging van het onderzoek binnen de wettelijke termijnen te melden en het Clinical Study Report (CSR) aan de CME te bezorgen.

Houd er in het geval van een klinische proef (EudraCT) rekening mee dat de resultaten moeten worden gepubliceerd in het European Clinical Trial Register. Het rapport van deze resultaten kan als CSR naar de EC worden gestuurd.

Appendix 3b: Points of concern (if applicable)

The EC emphasizes the responsibility of the PI/promotor of this study concerning the privacy of the person/patient data in contacts with patients, or when viewing patient data, including the correct implementation thereof by coworkers and students. The PI/promotor is responsible for the implementation of the project proposal in accordance with applicable laws and regulations including, but not limited to, the EU regulation 2016/679 (General Data Protection Regulation), the Belgian Law on patients' rights of 22/8/2002, and the policy of the institution where the research will be carried out.

The EC refers to the ICH/GCP guidelines on its website, and confirms that a GCP-training is required from each investigator. It is the responsibility of the principal investigator that each member of the study team has a valid GCP-certificate.

The conformity of translated documents compared to the Dutch documents, is the responsibility of the sponsor.
We would like to draw your attention to the fact that the EC expects her initial comments to be taken into account ab initio at the next submission by the same sponsor.

*Provided that there is a **Clinical Trial Agreement**, the study can only start when the Clinical Trial Agreement has been approved and signed by the CEO of UZ Gent (and/or by an authorized representative of UGent).*

Studies with investigational medicinal products and certain studies with "medical devices" should be submitted by the client (PI or sponsor) to the FAMHP (Federal Agency for Medicines and Health Products).
Studies with investigational medicinal products are only allowed to be conducted, provided that the minister (FAMHP) does not state objections within legal deadlines as described in art. 13 of the Belgian law of 7/5/2004 concerning experiments on the human person and art. 21 of the Belgian law of 7/5/2017 concerning clinical trials with medicines for human use.

Certain studies using medical devices are also covered by legal deadlines (KB of 17/3/2009). Please consult the FAMHP website for more information: www.fagg-afmps.be.

Research on embryos in vitro is covered by the law of May 11, 2003. Before the research project can start, such research also requires a positive advice of the Federal Committee for medical and scientific research on embryos in vitro.

Please take into account the regulations of the hospital concerning tissue management and the regulations of the law of December 19, 2008.

This favorable advice of the EC does not imply that it will assume responsibility for the planned study. You will remain responsible for the study. In addition, you should ensure that your opinion as an involved researcher is reproduced in publications, reports for the government, etc. which are the result of this study. You are reminded that concerning clinical studies, any observed serious event needs to be reported immediately to the sponsor and the ethics committee, even if the causal relationship with the study is unclear.

The EC approval given for a specific project, is valid for one year. We request you to inform us if the study will not be initiated or if the study does not start within 1 year after approval.

The EC confirms that - in case of conflict of interest - involved members do not take part in the vote concerning the study.

*If the study will not be terminated within a year, the ICH-GCP demands that an **annual progress report** will be provided to the EC.*

*Finally, we request you to report the termination (early or planned) of the study within the legal deadlines and provide the **Clinical Study Report** (CSR) to the EC.*

In case of a clinical trial (EudraCT), please be informed that the results must be published in the European Clinical Trial Register. The report of these results can be sent to the EC as the CSR.

FACULTY OF ENGINEERING AND ARCHITECTURE

Impact of Onyx Injection Velocity in Endovascular Embolization: a Computational Multi-Phase Flow Study of a Patient-Specific Arteriovenous Malformation

Kaat Wille
Student number: 02010479

Supervisors: Prof. dr. ir. Charlotte Debbaut, Prof. dr. Peter Vanlangenhove
Counsellors: Jessie Duquesne, Dr. ir. Danilo Babin, Mohammadjavad Sedghizadeh, Prof. ir. Vincent Keereman

Master's dissertation submitted in order to obtain the academic degree of
Master of Science in Biomedical Engineering

Academic year 2024-2025

GHENT UNIVERSITY

VUB VRIJE UNIVERSITEIT BRUSSEL